ABSTRACT

Title of Thesis:	HEAT TRANSFER MEASUREMENTS IN A SUPERSONIC FILM FLOW
	Colin Sawyer Adamson, Master of Science, 2016
Thesis Directed By:	Associate Professor, Dr. Christopher P. Cadou, Department of Aerospace Engineering

This thesis presents measurements of wall heat flux and flow structure in a canonical film cooling configuration with Mach 2.3 core flow in which the coolant is injected parallel to the wall through a two-dimensional louver. Four operating conditions are investigated: no film (i.e. flow over a rearward-facing step), subsonic film, pressure-matched film, and supersonic film. The overall objective is to provide a set of experimental data with well characterized boundary conditions that can be used for code validation. The results are compared to RANS and LES simulations which overpredict heat transfer in the subsonic film cases and underpredict heat transfer in supersonic cases after film breakdown. The thesis also describes a number of improvements that were made to the experimental facility including new Schlieren optics, a better film heater, more data at more locations, and a verification of the heat flux measurement hardware and data reduction methods.

HEAT TRANSFER MEASUREMENTS IN A SUPERSONIC FILM FLOW

by

Colin Sawyer Adamson

Thesis submitted to the Faculty of the Graduate School of the
University of Maryland, College Park, in partial fulfillment
of the requirements for the degree of
Master of Science
2016

Advisory Committee:
Assoc. Professor Christopher Cadou, Chair
Professor Arnaud Trouvé
Assoc. Professor Kenneth Yu

Dedication

To my family and friends, without whom I would most certainly not be where, or who, I am today.

Acknowledgements

I would like to thank my advisor, Dr. Christopher Cadou, for his guidance and help over the course of this project. I would also like to thank Dr. Robert Sanner, Dr. James Baeder, Dr. Inderjit Chopra, and my committee members Dr. Arnaud Trouvé and Dr. Kenneth Yu for their assistance over the past six years. Lab partners are the key to getting through graduate school, so thanks to Daanish Maqbool, Chandan Kittur, Salman Verma, Daniel Waters, Stephen Vannoy, Wiam Attar, Lucas Pratt, Branden Chiclana and Andrew Ceruzzi. I would like to express my heartfelt gratitude to the National Aeronautics and Space Administration and Melinda Nettles of the Marshall Space Flight Center for their support under NRA NNM13AA13G. Additionally, I would like to recognize and thank Joseph Ruf of Marshall Space Flight Center and James Beck of Aerojet Rocketdyne for their assistance and feedback throughout the course of this project. In addition, thanks to all of my family, my friends, and my girlfriend, for their unflagging support during my graduate career.

Table of Contents

List of Tables

List of Figures

Chapter 1: Introduction

1.1 Film Cooling Overview

Film cooling is an active cooling technique often used in gas turbines to cool the combustor liner and turbine blades [1], and in rocket engines to protect the thrust chamber and nozzle from hot exhaust gases [2]. Coolant is injected into the flow through holes or slots around the perimeter of the nozzle wall to create separation from the hot core flow.

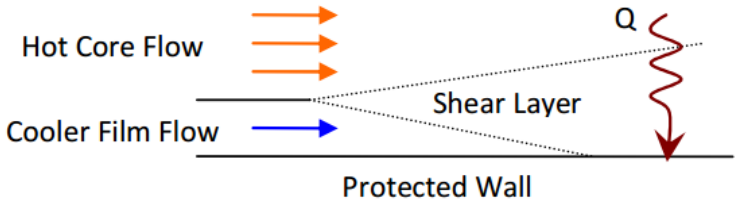

Figure 1: Simple film cooling theory (Adapted from Maqbool [3]*)*

A shear layer forms between the hot core and cooler film flows that grows with distance downstream until it contacts the wall. Thermal protection from the film is greatly reduced beyond this impingement point. Thus, it is important to be able to predict the growth of the shear layer and the location of its impingement point on the protected wall in order to predict the degree of thermal protection offered by the film. Adiabatic film cooling effectiveness can be thought of as a dimensionless adiabatic wall temperature where the difference between the adiabatic wall temperature (T_{aw}) and the core flow temperature (T_{∞}) is normalized by the difference between the film flow recovery temperature (T_f) and the core temperature [4]:

$$\eta = \frac{T_{aw} - T_{\infty}}{T_f - T_{\infty}} \quad (1)$$

As the film breaks down, the value of η ranges from 1 (complete film protection, $T_{aw} = T_f$) to 0 (film has fully mixed with the flow, $T_{aw} = T_{\infty}$). In the more realistic case of a non-adiabatic wall, heat flux into the walls varies with distance downstream as the film mixes with the core flow. Hansmann [4] proposes the following definition of film cooling effectiveness for non-adiabatic walls:

$$\eta = 1 - \frac{Q(x)}{Q_0(x)} \quad (2)$$

where $Q(x)$ is the heat flux into the film cooled wall, and $Q_0(x)$ is the heat flux into an analogous unfilm-cooled wall. However, using this definition is problematic because it is not clear what geometry $Q_0(x)$ corresponds to. Is it a bare wall without a film cooling louver or the film cooled wall with no film coolant flow? This work will make comparisons using both methods. A more detailed explanation of how this will be accomplished will be presented after the experimental apparatus is described in Chapter 3. Similar to the methodology used by Goldstein [5] which will be discussed in more detail later, the laboratory inability to produce a sufficiently heated core flow provided the motivation to reverse the heat flux vector. The problem is then, actually, a "film heating" problem, where the heat flux vector is reversed, moving from the walls into the flow. However, the results are still acceptable for code validation with Loci-CHEM.

1.2 Previous Work in Film Cooling

One of the earliest studies of supersonic film cooling was conducted by Goldstein, Eckert, Tsou and Haji-Sheikh in 1966 [6]. The study focused on a helium film flow injected through a rearward-facing slot into a Mach 3 core flow, with an air film flow for comparison. The tunnel operated with atmospheric temperature and pressure inlet conditions, and the walls and film were heated in order to form an inverse "film heating" problem. Though the heat flux vector was reversed, the film cooling effectiveness was still able to be calculated by adiabatic wall temperature measurements. Goldstein et. al. found that film cooling in supersonic flows was effective for a significant distance further downstream than in subsonic core flows. However, when the film started to degrade, it did so faster than in subsonic flows. Additionally, Goldstein et. al. used Schlieren imaging to identify the flow features, including an expansion fan when the flows met and a recompression shock that takes place in the film flow at lower film flows. Goldstein and various colleagues also conducted several studies with film flow injection normal to the core flow [5], [7], with similar but lower efficiencies, especially in the region 10-20 slot heights downstream from film injection.

Another early study in film cooling was conducted by Lucas and Golladay at NASA's Lewis Research Center. The study centered on film cooling in a small JP-4 gaseous oxygen rocket motor, with a nitrogen coolant flow injected tangentially to the wall in an annular ring upstream of the throat. The motor was fired for up to 70 seconds, long enough to achieve steady-state conditions. The wall of the nozzle was insulated and instrumented in order to produce an adiabatic wall temperature

distribution. The study found that the thermal protection was unexpectedly high in the region close to the slot for a certain selected slot height, and the authors were unable to explain this overprotection anomaly. In general, the study found that larger mass flows in the film provided more protection, as expected.

A similar study to the current research was conducted by Hunt, Juhany and Sivo in 1991 [8]. This study was aimed at hypersonic engines, and used air and helium as film coolants over a variety of temperatures and Mach numbers. The core Mach number was 2.4, and the film Mach number was varied from 1.2 to 1.9, with film pressure remaining matched to the core flow. This study had the advantage of using a continuous wind tunnel and establishing a steady state flow. As a general trend, Hunt, et. al. found that effectiveness increased with Mach number and the heat capacity of the film.

A very comprehensive study of the mixing of supersonic main flow with under expanded, over expanded, and perfectly expanded supersonic films was conducted by Aupoix, et. al. in 1998 [9]. They measured flow velocity, flow temperature profiles, wall temperature, and pressure in a M=2.78, 320 K core flow with M=2 coolant flows at 125 and 260 K. and compared them to several RANS turbulence models with a boundary layer code. Aupoix found that the RANS code was unable to capture the initial film-core interaction well, but accuracy improved with distance downstream. The experimental data indicated that the thermal protection of the film increased with film pressure, as is expected.

The effect of shock-film interactions in a supersonic film environment was studied numerically by Konopka, Meinke, and Schröder in 2012 [10]. They simulated

an incident shock wave from a M = 2.44 fully turbulent core film into a M = 1.8 laminar film flow and found that position of the impinging shock has a strong influence on the cooling effectiveness. The shock produced from a 5° flow deflection produced a 33% decrease in cooling effectiveness when close to the slot, but only a 17% decrease when it impinged further downstream. The effectiveness was reduced further at each position by a stronger shock produced by an 8° flow deflection.

1.3 Motivation

Performance in heat engines and rockets tends to improve with increasing working fluid temperatures [11]. This trend drives desired operating temperatures higher and higher, often past the melting point of the system components. In order to protect the integrity of the components, cooling techniques are required to produce safe and reliable engines.

Multiple cooling techniques have been developed over the past century for use in rocket engines. The most common methods are radiative, regenerative, and film cooling. Radiative cooling involves the transfer or heat from the rocket walls to the environment through the emission of photons. It is a passive mitigation method that is insufficient to manage the amount of heat dissipated from large liquid-fueled rockets, and in fact can be overshadowed by radiative heating from the interior flow in larger rockets such as the Saturn V [12]. Regenerative cooling involves piping cold fuel from the main fuel tank through passages in the combustor and nozzle wall before injecting it into the combustor. This has the twofold advantage of both cooling the engine structure and preheating the fuel. Film cooling, the subject of this study, uses a

stream of coolant gas – often turbopump exhaust - injected along the wall to physically separate it from the core flow [13].

The purpose of this study is to acquire fundamental film cooling performance data in supersonic environments that can be used to design the nozzle extension of NASA's J-2X. The development of the Space Launch System lead NASA to examine the performance of the J-2 rocket engines used on the Saturn platform. They found that the J-2 engines, while they performed adequately, were overdesigned in order to prevent failure due to excessive heating. One area of improvement was identified to be the nozzle extension, which was cooled regeneratively. While effective, regenerative cooling requires significant support structure and heavy alloys. Film cooling can eliminate these penalties or mitigate them, if both methods are used. However, simulation techniques struggled to produce accurate estimates of the film cooling performance because of a lack of validation data acquired in relevant environments: supersonic flows with favorable pressure gradients like those found in nozzles. Simulating the conditions encountered in the J-2X nozzle extension on the ground and making wall heat flux measurements was cost-prohibitive because they are so extreme: (p = 9.514 MPa, T = 3767 K, $\dot{m}$ = 297 kg/sec). Therefore it was decided to make heat flux measurements in a smaller scale 'canonical' experiment in order to provide data that are relevant for validation of film cooling simulations made using NASA Marshall Space Flight Center's preferred tool [14] (Loci-CHEM, a RANS (Reynolds-averaged Navier-Stokes solver) based simulation CFD package) at a much more modest cost.

Figure 2: Concept image of the J-2X engine (Adapted from NASA/MSFC [15]*)*

1.4 Previous work at UMD

To meet the needs of the J-2X development program, the University of Maryland has been undertaking a combined program of numerical simulations and experiments in a 'canonical' film cooling configuration for the past 9 years. The overall objective is not to simulate film cooling at J-2X conditions, as the current facilities cannot support the conditions, but to provide an experimental database with well-characterized boundary conditions that can be used to develop quantitatively predictive numerical simulations of film cooling performance.

Work at the University of Maryland on film cooling started with Cruz in 2008 [16]. Cruz performed experiments with adiabatic and non-adiabatic walls for various subsonic blowing ratios, and measured flow temperature and velocity using particle image velocimetry (PIV) and a micro thermocouple. He compared these results to his

new RANS and LES models. Cruz found that the film mixing was strongly influenced by the shear between the film and core flows, and that standard correlations over predict the mixing of the film. Cruz's LES models also over predicted the film cooling effectiveness but less so than the film correlations. Additionally, the LES models were three-dimensional, but were limited by an incompressibility assumption [17].

During this time, Raffan investigated subsonic film cooling. His work was focused on developed experimental minimally intrusive techniques for resolving velocity and temperature profiles near the wall. Raffan found that the film cooling performance in subsonic flows is strongly affected by the shear layer between the core and film flows [18]. These techniques and results are very useful for code validation and use in subsonic regimes, but the conditions are not applicable to the J-2X.

Dellimore began the supersonic film cooling research at University of Maryland, producing models to explain the effects of pressure gradients, density gradients, and compressibility on film cooling effectiveness. His exhaustive review of over 40 different studies resolved disagreements in the literature regarding the effect of pressure gradients on film cooling effectiveness. Dellimore showed that the effect of the pressure gradient depends on the velocity ratio: a favorable pressure gradient degrades film protection in 'core-driven' flows where the core flow is higher velocity than the film flow. Conversely, a favorable pressure gradient improves film cooling performance in 'wall jets' where the film flow has a higher velocity than the main flow. These effects are reversed in an adverse pressure gradient. Dellimore also

identified several fundamental non-dimensional parameters that influence film cooling performance [19]:

$$M_c = \frac{U_\infty - u_f}{a_\infty + a_f} \tag{3}$$

$$\lambda = \frac{\rho_f u_f}{\rho_\infty u_\infty} \tag{4}$$

$$s = \frac{\rho_f}{\rho_\infty} \tag{5}$$

$$r = \frac{u_f}{u_\infty} \tag{6}$$

They are the convective Mach number M_c, the blowing ratio λ, the density ratio s, and the velocity ratio r. Film cooling flows can be categorized using these four parameters[1]. He used his RANS simulations to develop an experiment that used a film heating approach to circumvent the difficulties of heating a supersonic core flow. The results of Dellimore's simulations and analysis, after consultation with NASA and Pratt & Whitney Rocketdyne, led to the development of a set of experiments to be conducted in the University of Maryland's supersonic wind tunnel. Because it is not possible to match all flow properties in the laboratory, the objective is to perform experiments under conditions in which the values of these non-dimensional parameters match those in the J-2X engine as closely as possible. With this in mind, Dellimore proposed the following test matrix:

[1] See [19] for a comprehensive analysis of the current film cooling literature.

Table 1: Test matrix proposed by Dellimore

	J-2X Engine	**Baseline**	**Off-Baseline #1**	**Off-Baseline #2**	**Off-Baseline #3**
Pressure Gradient	Favorable	Zero	Zero	Zero	Favorable
h (m)	$6.35x10^{-3}$	$6.35x10^{-3}$	$6.35x10^{-3}$	$6.35x10^{-3}$	$6.35x10^{-3}$
Core **Film**	H_2/O_2 H_2/H_2O	Air Air	Air Air	Air Air	Air Air
M_∞ M_f	3.74 1.40	2.40 0.73	2.40 0.50	2.40 1.40	2.40 0.73
$T_{0,\infty}(K)$ $T_{0,f}(K)$	2093 300	300 340	300 340	300 340	300 340
U_∞**(m/s)** U_f**(m/s)**	1254.92 558.789	568.0 225.6	568.0 180.4	568.0 438.6	568.0 255.6
$T_w(K)$ $T_\infty(K)$ $T_f(K)$	- 1667.6 323.9	340.0 139.4 307.5	340.0 139.4 323.8	340.0 139.4 244.3	340.0 139.4 307.5
$T_{f\to\infty} = T_f - T_\infty(K)$ $T_{w\to f} = T_w - T_f(K)$	1343.8 -	168.1 32.5	184.4 16.2	104.8 95.8	168.1 32.5
$s = \frac{\rho_f}{\rho_\infty}$	1.39	0.45	0.43	0.57	0.45
$\lambda = \frac{\rho_f U_f}{\rho_\infty U_\infty}$	0.62	0.20	0.14	0.44	0.20
$R = \frac{U_\infty}{U_f}$	2.22	2.22	3.13	1.30	2.22
$M_c = \frac{U_\infty - U_f}{a_\infty + a_f}$	1.08	0.53	0.65	0.24	0.53

In Table 1, various quantities are shown for the J-2X engine and baseline laboratory comparison experiments. The leftmost column shows the values present in the J-2X, and the baseline case was designed to match the velocity ratio, R. Off-Baseline #1 was designed to match the convective Mach number, and Off-Baseline #2 implements a supersonic film. Off-Baseline #3 again matches the velocity ratio and implements a favorable pressure gradient similar to the one present in the J-2X.

Maqbool designed, constructed and began preliminary testing on the experiment first mentioned by Dellimore [20]. His apparatus is shown in Figure 3.

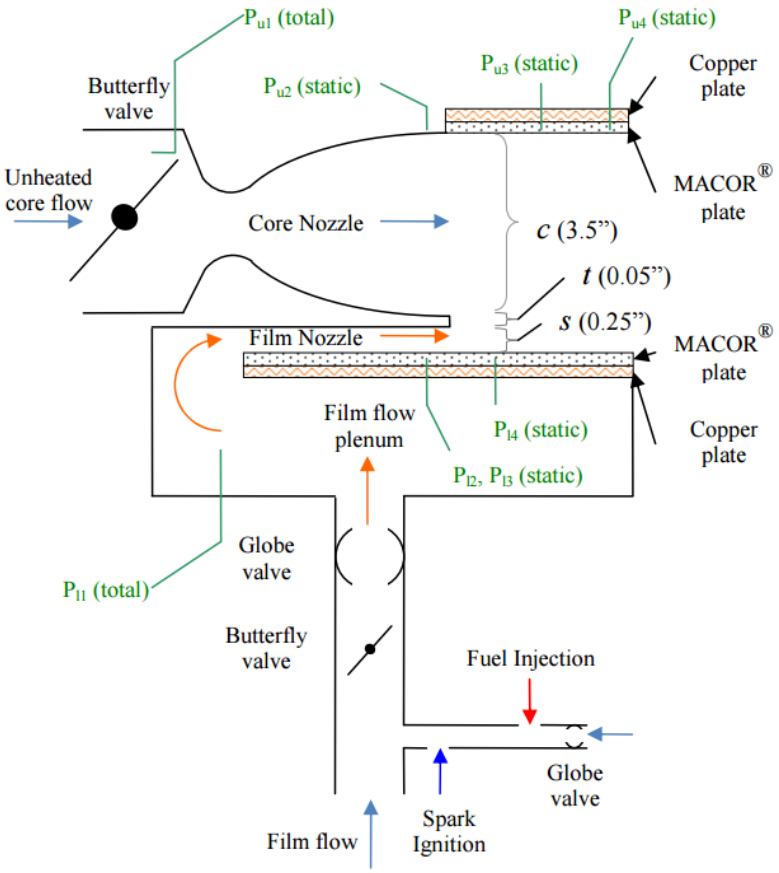

Figure 3: Test section schematic as designed by Maqbool

He also developed a much simpler and faster analytical method for determining heat flux than was used by others in the literature based off of the method used by Chen and Chiou [21], [22]. The method can infer heat flux measurements in walls with initial temperature gradients to within 5% uncertainty from subsurface temperature-time histories. He also recorded Schlieren images of the flow field and shear layer with relatively limited fields of view (18 x 11 slot heights).

Additional measurements and simulations were conducted by Voegele in 2013. His experiments used Particle Image Velocimetry to measure two-dimensional mean and fluctuating velocity for turbulent flow. He then developed an LES code for

simulation of the experiments. However, only the simulated experiments were supersonic, and were conducted in the non-adiabatic case [23].

The most recent experimental work at the University of Maryland was conducted by Collett in 2014. He improved the structural integrity of the test apparatus, implemented an automated image processing algorithm to analyze structures present in Schlieren images, and extended the heat flux measurement base that Maqbool started. The test matrix developed by Maqbool and used by Collett and this work can be found in Table 2.

Table 2: Final Test Matrix

	J-2X	**Test Case 0**	**Test Case 1**	**Test Case 2**	**Test Case 3**
Pressure Gradient	FPG	ZPG	ZPG	ZPG	ZPG
Core fluid **Film fluid**	H_2O H_2O, H_2	Air Air	Air Air	Air Air	Air Air
$\boldsymbol{M_\infty}$ $\boldsymbol{M_f}$	3.74 1.40	2.40 0.00	2.40 0.50	2.40 0.72	2.40 1.40
$\boldsymbol{T_{0,\infty}}$**(K)** $\boldsymbol{T_{0,f}}$**(K)**	2093 300	298 N/A	300 340	300 340	300 340
$\boldsymbol{u_\infty}$**(m/s)** $\boldsymbol{u_f}$**(m/s)**	1254.92 558.789	568.0 N/A	568.0 180.4	568.0 255.6	568.0 438.6
$\boldsymbol{M_c}$	1.08	1.64	0.65	0.53	0.24
$\boldsymbol{\lambda}$	0.62	N/A	0.14	0.2	0.44
s	1.39	0.0	0.43	0.45	0.57
r	2.22	N/A	3.13	2.22	1.30

Collett found that the current Loci-CHEM models over predicted the thermal protection provided by the film in subsonic cases but under predicted protection in supersonic cases with the greatest discrepancy in prediction located near the film injection point.

Verma has been conducting RANS and LES simulations of film cooling performance during the course of this work. His simulations will be shown as a comparison to the heat flux measurements. Additionally, he created a simple 1-D conduction solver for additional comparison to the inverse heat flux method.

1.5 Shortcomings of previous UMD work

The experimental results over the past several years have provided a solid base for analysis, but they have suffered from some shortcomings.

1. The nozzle initially designed by Maqbool and used in the experiments conducted by Maqbool and Collett suffered from an incorrect smoothing algorithm.
2. Some of the test cases exhibited very poor agreement between experiments and CFD.
3. The quantity of data from past experiments were insufficient to sufficiently reduce the random error of the measurements.
4. Schlieren images recorded by Maqbool and Collett were of limited size and quality.
5. The inverse heat transfer measurement technique was difficult to use, raising questions about its efficacy.

1.6 Objectives

The objectives of this thesis are as follows:

1. Improve the experimental apparatus.

a. Design, fabricate and install a new nozzle that eliminates the spurious shocks present in previous experiments caused by an improperly designed nozzle. Construct the nozzle using steel to reduce vibration.
b. Redesign the tunnel walls and heat flux gauges to increase instrumentation density around regions of interest (shock-wall and expansion-wall interaction areas) and mitigate regions of high stress to reduce breakage.
c. Design and install an electric film heater to replace the propane film heater.
d. Broaden the field of view of the Schlieren images to span the full height (and in some cases length) of the test section.

2. Improve the supersonic film cooling database. Collect at least 15 sets of temperature, pressure, and Schlieren measurements data in each of four test cases and compute flow Mach number and upper and lower wall heat flux distributions (from the measured temperature-time histories). Compare the measured heat flux distributions to those predicted by RANS (Reynolds Averaged Navier Stokes) calculations implemented in Loci-CHEM [14] and LES (Large Eddy Simulation) calculations implemented in OpenFOAM [24].
3. Expand, improve and validate the heat flux measurement technique and data via independent tests with known boundary conditions. Better quantify the uncertainties associated with the heat flux measurement technique.
4. Design an experiment suitable for collecting heat flux and pressure measurements in a Favorable Pressure Gradient (FPG) environment.

Chapter 2: Experimental Apparatus: Film Cooling

2.1 Wind Tunnel Basics

The University of Maryland's supersonic wind tunnel is an indraft tunnel operating at atmospheric total temperature and pressure that is capable of producing flows up to Mach 3 for approximately 4 seconds. Lower Mach numbers provide longer test times. The tunnel's test section is 6" x 12" in cross section and is 36 inches long. The test section, butterfly valve and intake bell are shown in Figure 4. A close up view of the test section is presented in Figure 5.

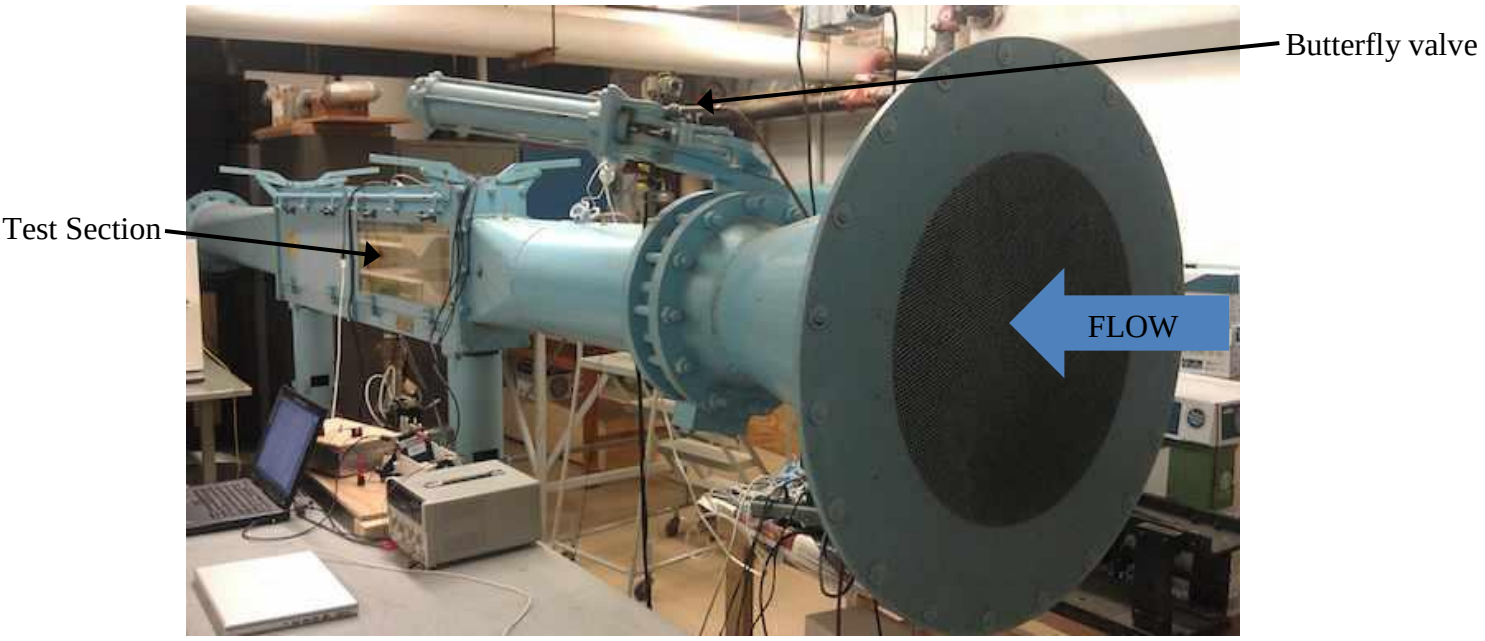

Figure 4: University of Maryland supersonic wind tunnel

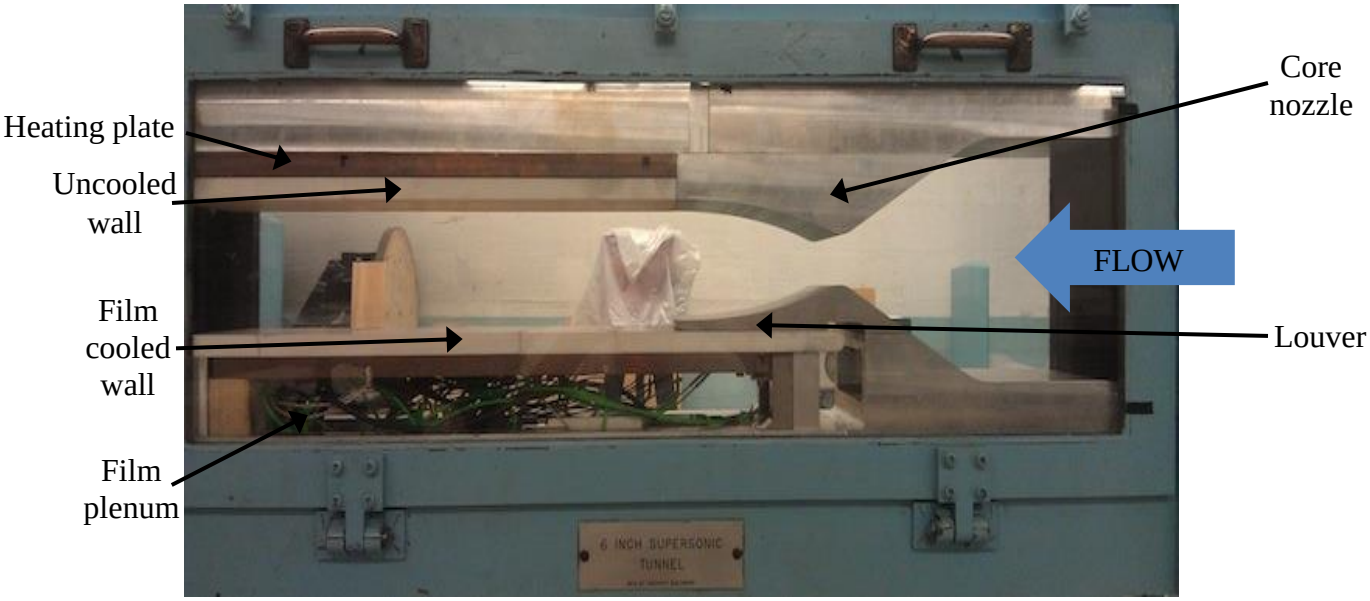

Figure 5: Supersonic test section installed in wind tunnel

2.2 Test section material selection

The wall must act like a semi-infinite thermal body over the course of an experiment in order for the method used to infer lower wall heat flux from subsurface temperature-time histories to be valid. This means that the primary direction of heat transfer must be perpendicular to the surface of the plate (i.e. little streamwise or spanwise flow of heat in the plate) and that the temperature of the backside of the plate (i.e. the surface not exposed to the flow) must remain constant over the course of an experiment. This requires a wall material with a very low thermal diffusivity and MACOR, a machinable ceramic with a thermal diffusivity of $7.3 * 10^{-7} \frac{m^2}{s}$, was chosen. The plate thickness was chosen to be greater than thermal penetration distance associated with the longest experiment (projected to be about 6 seconds).

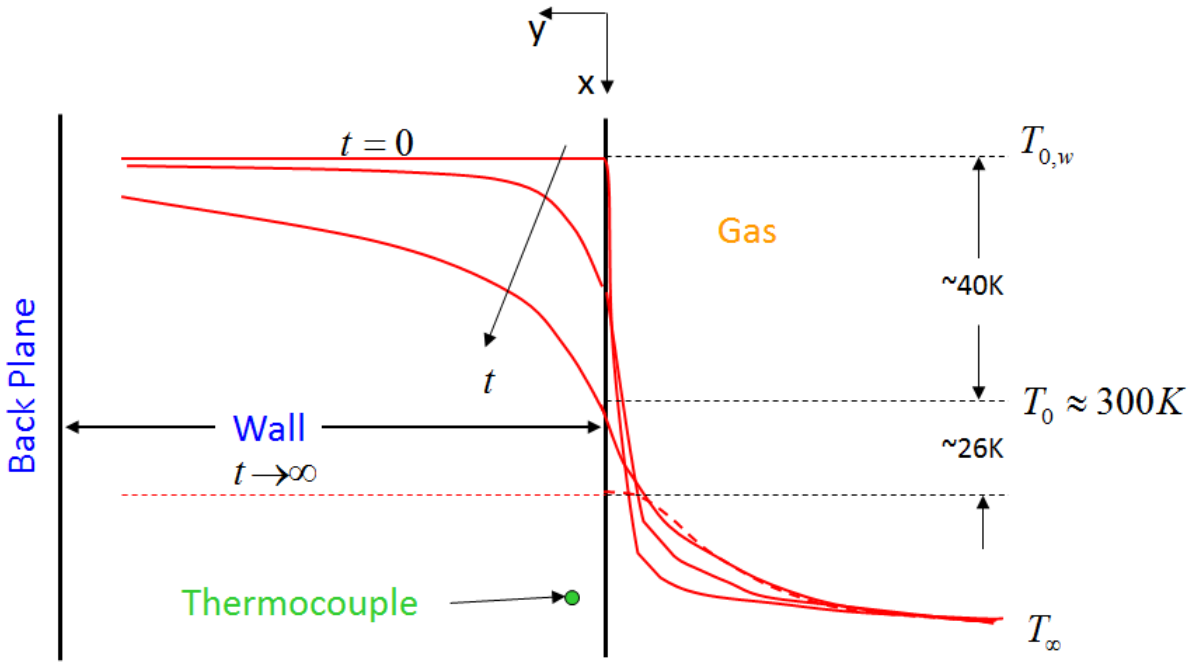

Figure 6: Progression of the thermal wave into the tunnel wall

Figure 6 shows a sketch of the physics of the thermal wave. At t = 0, the wall and gas are at initial temperatures $T_{0,w}$ and T_∞. As time increases, shown by the t arrow, heat begins to transfer from the surface into the gas, causing the red temperature curve to shift. Once the decrease in temperature has contacted the backplane, the semi-infinite thermal assumption is no longer true. The thermal penetration depth is defined as the distance below the surface of the plate at which the temperature has changed significantly. Solutions to the unsteady 1-D energy equation in a semi-infinite solid [25] lead to the following expression for thermal penetration distance in terms of the thermal diffusivity of the material, α, and the test time, t:

$$\delta = 4\sqrt{\alpha t} \tag{8}$$

The thermal penetration distance for a 6 second experiment with MACOR walls is 0.326 inches so heat flux gauges are spaced farther apart than this in order to

ensure that they are not influenced by streamwise or spanwise conduction. The thickness of the plate is chosen to be approximately twice this distance in order to ensure that the outer wall temperature remains constant and to make the wall stronger/more robust.

2.3 Summary of basic measurements

Two main types of measurements were identified for analysis: static pressure and temperature. The pressure measurements are used to determine the core and film Mach numbers, the pressure of the film, and strengths of shocks and expansions incident upon the walls. Static pressure taps are mostly located along the centerline of the test section, although several taps are placed off center to evaluate flow symmetry and avoid interference with heat flux measurements. Each pressure tap consists of a 0.02 inch diameter hole in the MACOR wall, which is connected to 0.05 inch diameter pipe and tubing, as recommended by Figliola [26]. Because the static pressure is assumed to be constant over the course of the run, the dynamic response of the pressure tap, tubing, and transducer do not need to be taken into account. Static pressure is also measured upstream of the nozzle, at the nozzle exit, outside of the tunnel, and in the plenum in order to determine core and film Mach numbers and atmospheric conditions. Wall temperature measurements are made using T-type thermocouples embedded in the MACOR walls. Two T-type thermocouples measure gas temperature in the plenum. The first thermocouple was placed at the inlet of the plenum, directly above the film heater, in order to measure the initial temperature entering the plenum and to ensure it was not high enough to damage any of the electronics located in the plenum. The locations of the temperature and pressure

gauges are tabulated in Table 3 and shown graphically in Figure 7. Distance downstream is reported non-dimensionally in terms of x/s: distance downstream (x) divided by the louver (or slot) height (s). Several thermocouples were damaged during installation and are marked “Inactive” in Table 3.

Table 3: Location of thermocouples and pressure taps

Lower Plate			Upper Plate		
Location (x/s)	Type of gauge	Status	Location (x/s)	Type of gauge	Status
-0.6	P	Active	6	T	Active
-0.6	P	Active	10	T	Active
0	T	Active	17.5	P	Active
2.5	T	Active	17.5	T	Active
2.5	T	Active	17.5	T	Active
5	T	Active	25	P	Active
7.5	P	Active	25	P	Active
10	T	Active	25	T	Active
15	T	Active	28.5	T	Inactive
17.5	P	Active	28.5	T	Inactive
17.5	T	Active	31.5	P	Active
17.5	T	Active	31.5	P	Active
20	T	Active	31.5	T	Inactive
25	P	Active	34.5	T	Active
25	P	Active	34.5	T	Active
25	T	Active	37	P	Active
28.5	T	Active	37	P	Active
28.5	T	Active	37	T	Active
30.25	T	Active	39.5	T	Active
32	T	Active	39.5	T	Active
32	T	Active	42	P	Active
35	P	Active	42	P	Active
35	P	Active	42	T	Active
35	T	Active	46	P	Active
37.5	P	Active	46	T	Active
40	T	Active	46	T	Active
45	P	Active	50	T	Active
45	T	Active	53	P	Active
45	T	Active	56	T	Active
50	T	Active	59	T	Active
53.25	P	Active	59	T	Active

56.5	T	Active	62	T	Active
59	T	Active	65	P	Active
59	T	Inactive	67.5	T	Inactive
61.5	T	Active			
63.25	P	Active			
65	T	Inactive			

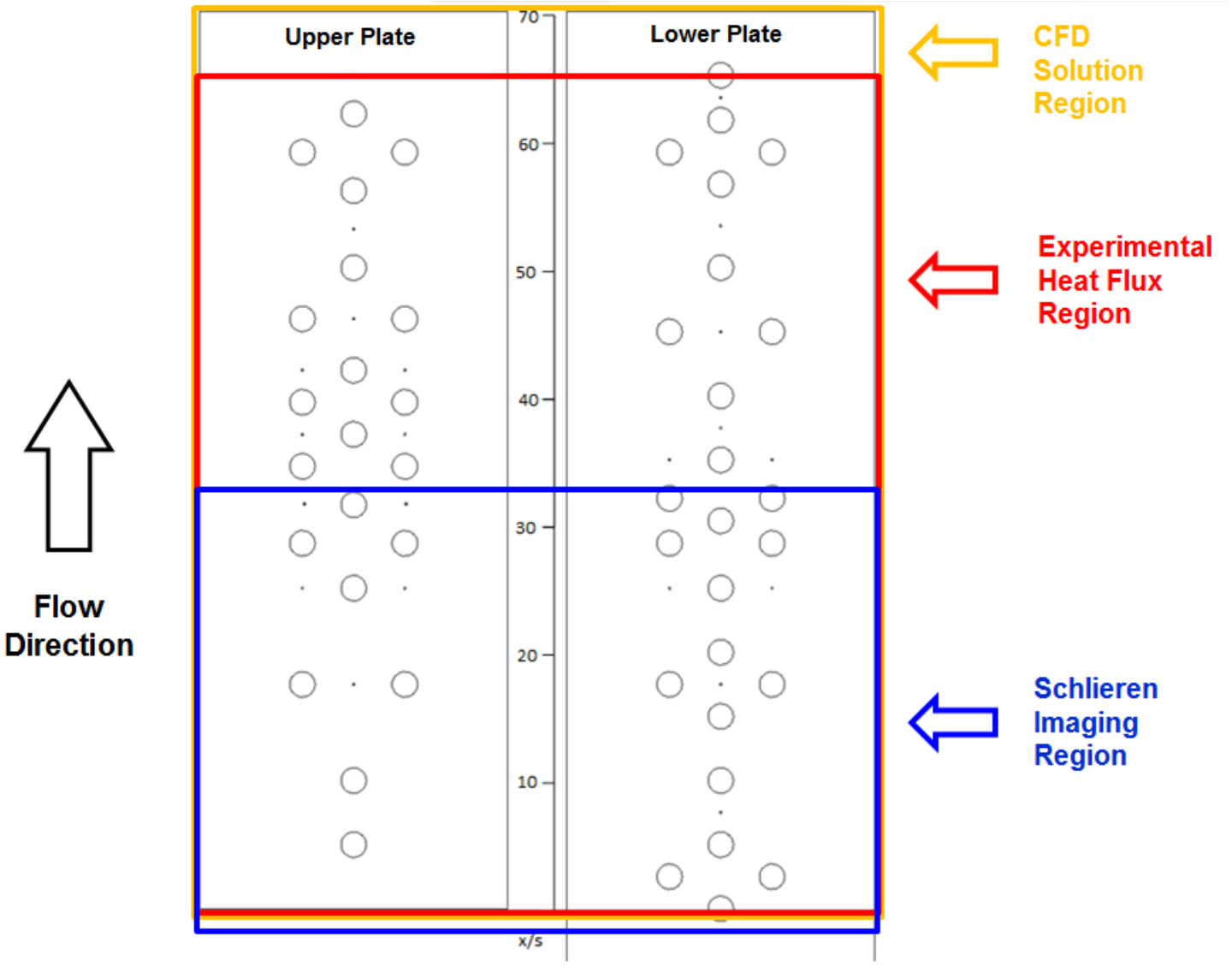

Figure 7: Schematic of heat flux gauge and pressure tap locations

2.4 Instrumentation

2.4.1 Heat flux gage selection

Wall heat flux is usually measured using one of three approaches: thin film gauges [27], slug calorimeters [28], or wall-embedded sensors [29].

Thin film gauges consist of thermocouples or thermistors deposited onto a thin, flexible, electrically insulating substrate like Kapton tape. They are attached to the surface of interest to measure its temperature-time history.

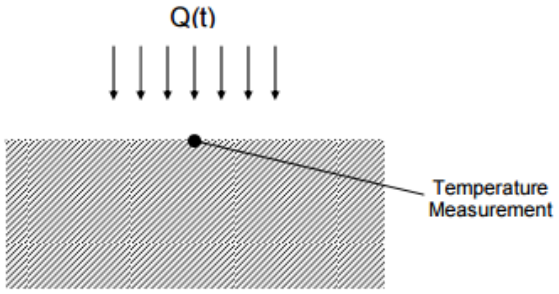

Figure 8: Thin film gauge for heat flux measurement (Adapted from Maqbool [20]*)*

While they provide excellent temporal response and direct measurements of surface temperature, the gauges and their wires protrude into the flow. Since film cooling performance is known to be heavily influenced by free stream turbulence [30], it is important to avoid introducing new disturbances and so thin film gauges are not ideal.

Slug calorimeters consist of a temperature sensor surrounded by a uniform, conductive material embedded in the test surface as illustrated in Figure 9. An unsteady energy balance on the slug permits one to infer total surface heat flux over a time interval from the change in the slug's temperature over the time interval. The slug temperature can be measured at a single point because the slug is usually mad

from very conductive material so that temperature gradients within the slug itself can be assumed to be small. (i.e. the Biot number is << 1). While slug calorimeters minimize flow disturbances, they respond relatively slowly (~seconds because of their relatively high thermal mass) making them unsuitable for use in the high speed flows of interest here which only persist for a few seconds.

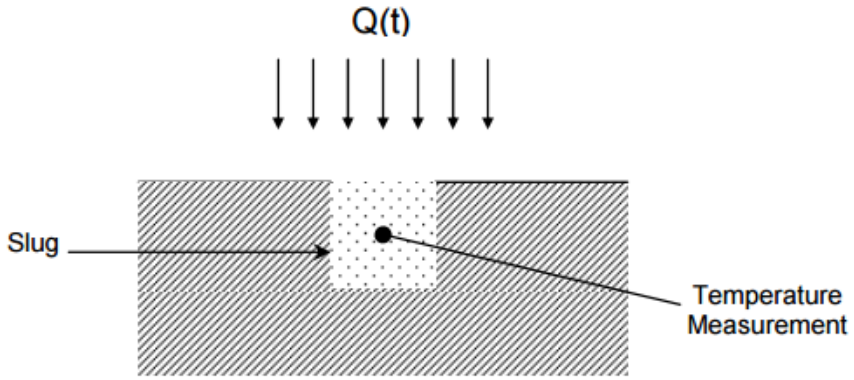

Figure 9: Slug calorimeter for measuring heat flux (Adapted from Maqbool [20]*)*

The method used here involves embedding a thermocouple in the wall a small (and precisely known) below the surface and measuring the temperature-time history there. An inverse solution to the 1-D heat equation with boundary condition given by the subsurface temperature-time history can be used to infer the temperature and heat flux at the surface [22]. The advantages of the technique are that it is non-intrusive, can predict temperature and heat flux at the surface as a function of time, and is simple to construct using prewelded thermocouples and plugs embedded in the wall. The main drawback is that the inverse solution method is complex, time consuming, and sensitive to small variations or errors in the temperature signal. Maqbool addressed this problem in 2010 by devising a simpler inverse technique for inferring

surface heat flux from the subsurface temperature time history. This technique will be discussed more in Section 3.1 Solving the inverse heat transfer problem.

The distance of the thermocouple bead below the test section surface was initially selected by Maqbool to be 0.05 inches. This distance reflected a tradeoff between measurement response and mechanical robustness. The closer the thermocouple is to the surface, the faster it is able to respond to the flow conditions, the larger the total temperature change will be, and thus the more accurate the final determination of heat flux will be. Reducing the gauge depth increases stresses present in the MACOR membrane during testing leading to multiple gauge failures. Collett improved reliability by adding a fillet to reduce stress concentrations in the MACOR membrane and increasing the gauge depth to 0.055 inches. While this degraded the amplitude and speed of the temperature response, it was necessary to maintain the integrity of the plates over the course of many experiments. These improvements were also implemented in this round of testing.

2.4.2 Temperature Measurements

The thermocouples were embedded in the wall by wrapping a 0.01 inch diameter Omega COCO-010-BW thermocouple over the end of a cylindrical MACOR plug. A chase machined in the plug ensures the thermocouple bead ensures that the thermocouple bead remains centered over the end of the plug. The plug is coated with thermal grease and inserted into a matching hole bored in the back side of the MACOR measurement plate. The thermal grease is selected to match the thermal conductivity of the MACOR plate, k = 1.46 W/mK. It is critical to ensure that the grease fills the entire gap as any form of incomplete contact between the plug and

wall will result in retardation of the thermal wave. However, using too much grease will prevent the plug from being fully seated, creating an air gap between the back side of the MACOR wall and the heating plate which could hamper plate and wall heating. The thermocouple leads are insulated with heat-shrink tubing to prevent contact with the copper heating plate or tunnel walls.

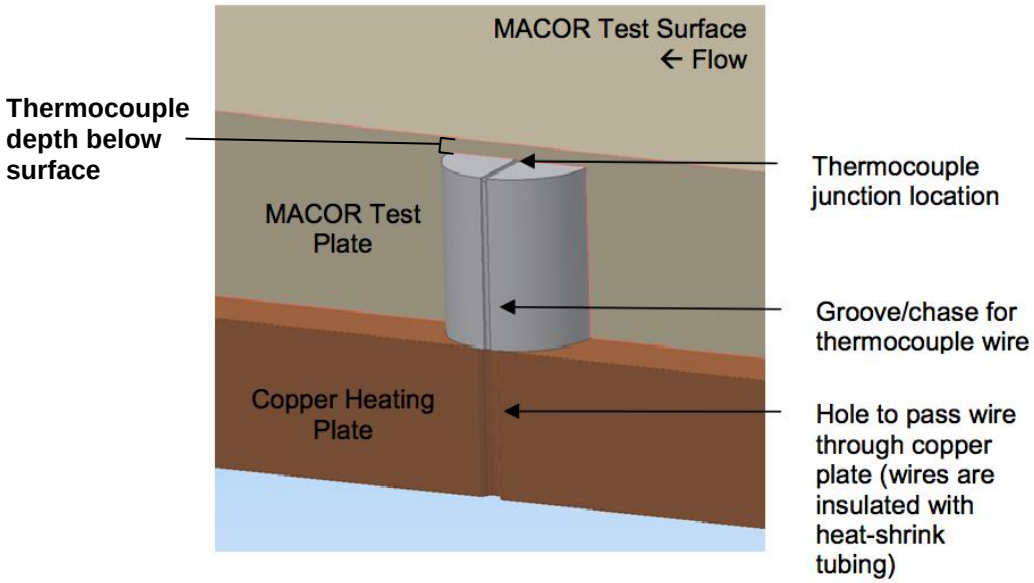

Figure 10: Cutaway of heat flux gauge (Adapted from Maqbool [20]*)*

The thermocouples are sampled at 25 Hz. Temperature signals from the heat flux gauges are measured using four NI-9213 thermocouple modules mounted in NI USB-9162 USB chassis. The digitized data are transmitted from the module to the logging computer through a USB cable mounted in a pressure-tight pass-through as illustrated in Figure 11. The pressure data are recorded with a NI-9205 module mounted in a NI cDAQ-9178 chassis. All of the data were logged on a Lenovo R500 running LabVIEW 8.6 and later analyzed with MATLAB.

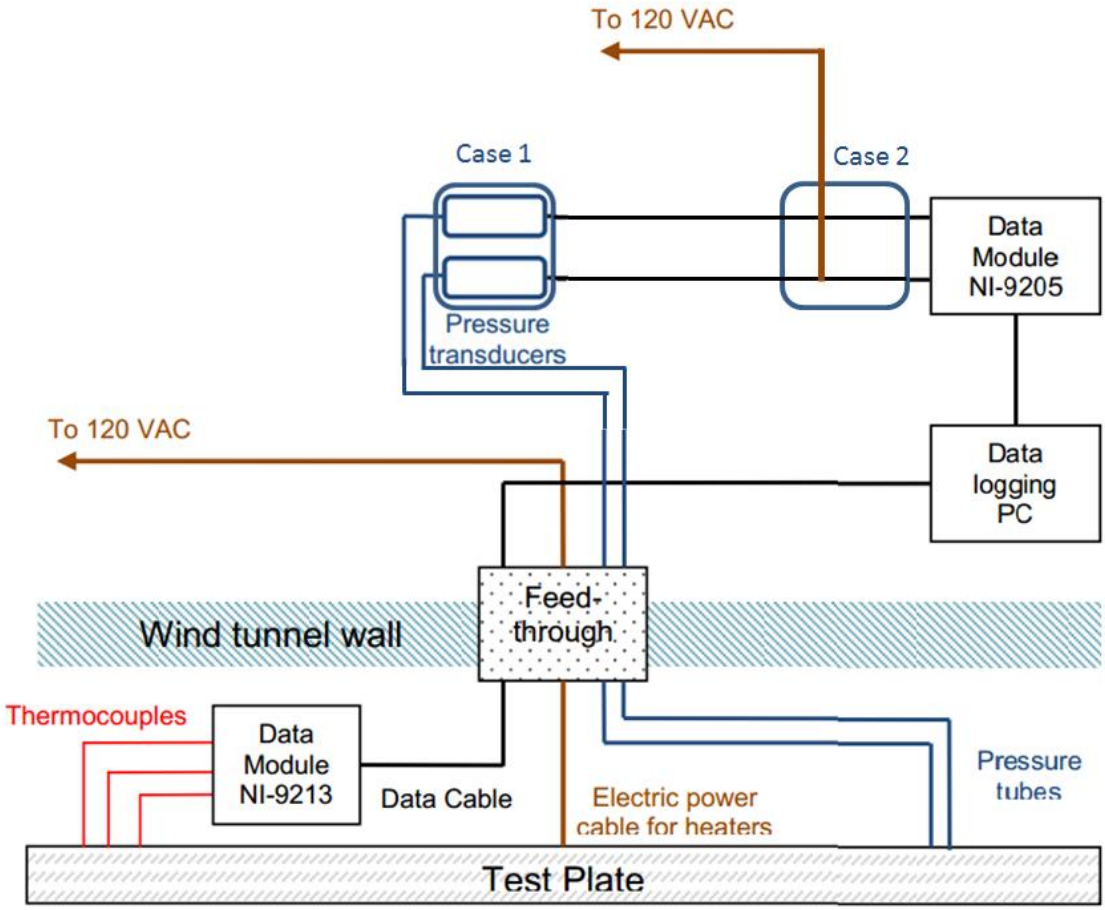

Figure 11: Data recording schematic

2.4.3 Pressure Measurements

The pressure taps were connected via flexible tubing through a pass-through in the tunnel wall to Omega PX309-015V5V pressure transducers. The transducers measure from 0-15 psi (atmospheric) and output a value from 0-5 volts at a maximum frequency of 1000 Hz. Signals from the pressure transducers were sampled at 250 Hz.

2.5 Schlieren Imaging

Schlieren photography is an extremely useful technique for studying supersonic flows. Schlieren photography was developed by August Toepler in 1864

[31] and remains a standard method for visualizing structures in supersonic flows to this day. It works by passing a collimated light beam through the test section. Density gradients in the test section deflect the beam, causing some of the light to become blocked by a 'stop' placed at the focal point of the formerly collimated beam. Figure 12 shows the principle of the Schlieren cutoff – undeflected beams of light are allowed to pass, while a deflected beam (shown by a dashed line) is obstructed by the stop, creating a dark region.

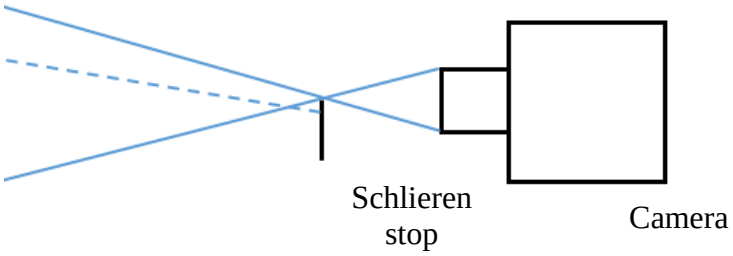

Figure 12: Schlieren cutoff principle

The resulting image has lighter and darker regions whose intensity is proportional to the magnitude of the density gradient, allowing shocks and boundary layers to be clearly identified. It is important to note that this is an integrated technique, so it provides an average of the features across the test section and it is most useful for studying two dimensional flows. There are many possible optical setups; the version used in this work is illustrated in Figure 13.

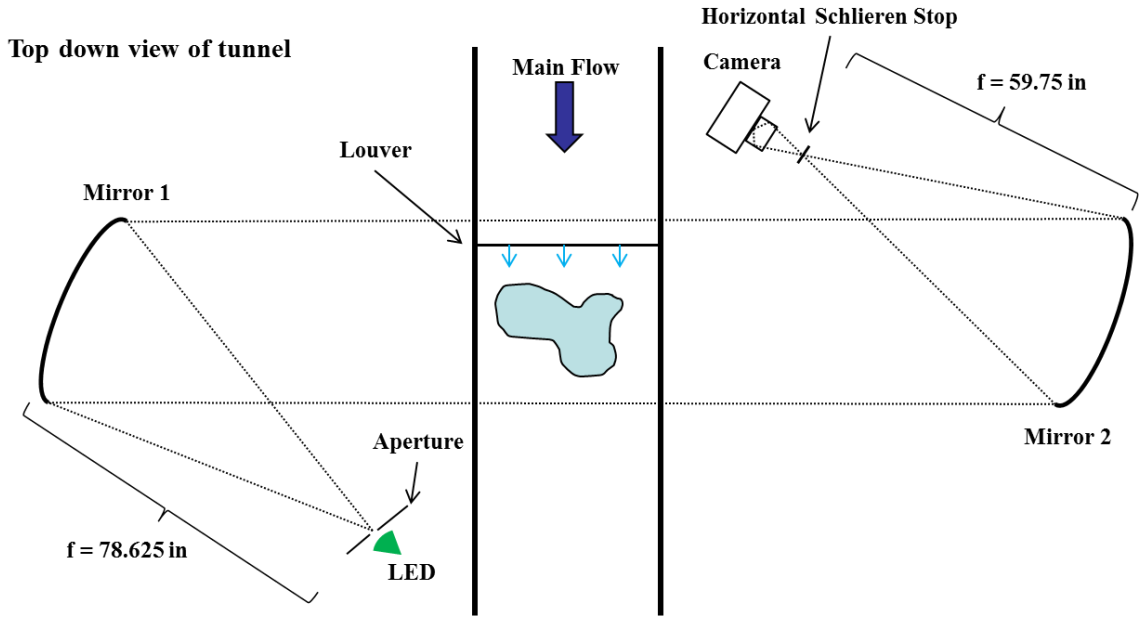

Figure 13: Schlieren System as implemented in supersonic wind tunnel

Maqbool and Collett used the Schlieren setup illustrated in Figure 13 to image flow structures in supersonic film cooling flows, but each set of images had its limitations. Maqbool was able to produce images with good contrast but the overall image was dim due to an underpowered light source. The field of view was also small, so the entire height of the test section was not captured and spurious shocks created by the incorrect nozzle profile disrupted the flow. Collett's contribution was to acquire more images so that averaging could be performed but the images themselves still suffered from the same problems.

2.6 Experimental Procedure

The tunnel operation procedure is as follows:

1. The upper and lower test plates are heated by cartridge heaters in a copper backplate to a temperature of 50°C above ambient, then

allowed to fall to 40°C above ambient to ensure thermal uniformity. Data recording is used to monitor plate temperature.

2. The test section and vacuum tanks located outside of the building are evacuated to a pressure of roughly 6 kPa. The main tunnel is sealed from the atmosphere upstream by a large butterfly valve and the film inlet is sealed by a smaller butterfly valve.
3. The butterfly valves are operated by a pair of solenoids, which are opened upon depressing a foot pedal. This starts the core and film flows. After pressure measurements in the core flow have confirmed that the flow has become subsonic, the valves are closed and the run is complete.

Chapter 3: Experimental Apparatus: Full Plate Ice Tests

3.1 Solving the inverse heat transfer problem

Generally speaking, 'inverse' problems involve the determination of "unknown quantities appearing in the mathematical formulation of a physical problem by using measurements of the system response" [32]. In the heat transfer problem of interest here, the objective is to determine the temperature and heat flux at the surface of the wall from measurements of the temperature-time history below the surface. There are several methods accomplishing this. Some use finite differencing schemes [33][34], while others use curve fitting to a functional form of a solution to the 1-D unsteady conduction problem [22][35][29]. However, most of these are very complex and thus not suitable for general use. An additional complication of the film cooling problem of interest here is that the MACOR walls are not isothermal at the beginning of the experiment, because they lose heat to the environment at different rates on each side. Maqbool addressed this problem by adapting the curve-fitting method of Chen, Chiou and Thomsen [22] for an initially nonisothermal wall in contact with a convective flow. An explanation of the governing equations and solution procedure is beyond the scope of this thesis. These details and MATLAB code that implements the inverse solution can be found in Maqbool's thesis [20]. An updated version of the MATLAB code that enables automated processing of multiple temperature-time data sets is presented in Appendix A. While Maqbool was able to verify that his code solved the inverse problem correctly, it was never tested using data acquired from a real physical system whose response was well known. Since the

heat flux measurements depend on the accuracy of the inverse solution method, it is very important to verify its performance in a physical system.

The numerical method developed by Verma is a simple solver of the 1-D conduction equation similar to methods put forward by Figliola [26] and Ozisik [36]. The solver reads in the thermocouple temperature-time history, predicts a heat flux at the surface, and then attempts to reconstruct the temperature time history at some depth below the surface.

3.2 Full plate overview

The physical system that will be used to verify the inverse solution method is a solid that is impulsively exposed to a temperature difference. This is a good model problem because it is relatively simple to perform experimentally – all it requires is immersing a surface of a block of material with an embedded thermocouple in an ice bath. Analytical solutions to this problem are available and can be compared to the measured temperature-time history. In this case, the "block" of material was a section of the tunnel wall with heat flux gauges installed, as seen in Figure 14.

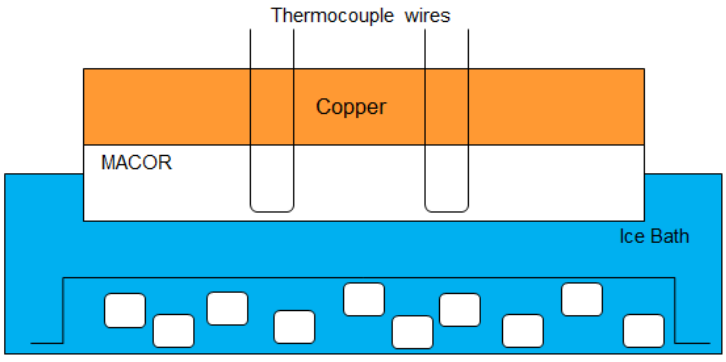

Figure 14: Tunnel wall impulsively exposed to ice bath

The objective is to predict the temperature of the wall at the surface (a known in the experiment) from measurements of subsurface temperature-time histories. The performance of Maqbool's analytical method is also checked via comparison to an iterative 1-D conduction solver developed by Verma.

3.3 Experimental Procedure

In order to confirm the validity of the inverse method, a method for comparison was devised. By introducing the initially non-isothermal instrument to a known boundary condition, a comparison can be made between the inverse curve-fitting method of Maqbool and a simple iterative 1-D conduction equation solution created by Verma. The impulsive thermal boundary condition was applied by lowering the full upper test section into a tray containing ice water. The subsequent temperature-time histories were processed by both codes. The comparison of the two methods provides physical validation for the curve-fitting method, and a greater confidence in the final results from the collected data.

The calibration was performed on with the upper wall instrument and a new lower wall instrument (because the old one had failed during a tunnel run). The walls were tested in both unheated (ΔT between wall and ice bath = 20°C) and heated (ΔT between wall and ice bath = 40°C) states.

Chapter 4: Uncertainty Analysis

The overall uncertainty in measured heat flux is the root mean square sum of the systematic and random components of the uncertainty:

$$U_{tot} = \sqrt{V^2 + S^2} \tag{9}$$

Sources of systematic uncertainty considered are presented in Table 4.

Table 4: Sources of Systematic Uncertainty

Source of Uncertainty	Magnitude of Uncertainty
Thermocouple variance	+/- 0.5 K
Uncertainty in thermocouple position	+/- 0.005 inches
Uncertainty in MACOR thermal properties	+/- 3%
Heat flux numerical curve fit error	+/- 3%

The Omega thermocouples advertise a +/- 0.5 K measurement uncertainty. The DAQ module is equipped with an autozero channel that is used to calibrate the thermocouple output and mitigate any offset. It is assumed that the MACOR plugs place the thermocouple junction in direct contact with the bottom of the bore in the MACOR plates. Thus the position of the thermocouple is set by the thickness of the MACOR membrane above the thermocouple. Technical Products Incorporated, the makers of the MACOR plates, quotes a machining tolerance of 0.005 inches, so this is the assumed uncertainty in the membrane thickness and thus the thermocouple position. The thermal properties of the MACOR itself can also vary by up to 3% causing spatial variations in thermal propagation. Finally, there is some error inherent in the inverse solution as the predicted heat flux can fluctuate around the actual heat flux by as much as +/- 3%.

The systematic error (V) of a quantity q that depends on parameters P_1 to P_I is given by [20]:

$$V^2(P_1, P_2, \ldots P_I) = \sum_{i=1}^{I} (\theta_i \delta_i)^2 \tag{10}$$

$$\theta_i = \frac{\Delta V}{\Delta P_i} \tag{11}$$

Where δ_i is the expected variation or uncertainty in the i^{th} parameter and I is the total number of parameters. Combining all four sources of uncertainty (voltage measurement, membrane thickness, k_{MACOR} and heat flux error) yielded a maximum systematic uncertainty of 9.5%.

The random component of uncertainty arises from natural experiment-to-experiment variations. The impact of these variations on the overall uncertainty can be reduced by increasing the number of measurements. In this work, N = 15 was considered to be a large enough sample size to adequately reduce the random component of the error. The mean heat flux (q) at one x/s location is calculated as follows:

$$\bar{x} = \frac{1}{N} \sum_{i=1}^{N} q_i \tag{12}$$

The variance, standard deviation, and standard deviation of the mean are given by:

$$S_x^2 = \frac{1}{N-1} \sum_{i=1}^{N} (q_i - \bar{x})^2 \tag{13}$$

$$S_x = \sqrt{S_{\bar{x}}^2} \tag{14}$$

$$S_{\bar{x}} = \frac{S_x}{\sqrt{N}} \tag{15}$$

From the standard deviation of means, it is possible to calculate random error for each case and x/s position with Student's t-test values. Random error is calculated as follows:

$$Err_{rand} = S_{\bar{x}} * t_N \tag{16}$$

Where t_N corresponds to the t-test value for the number of samples available at a confidence interval of 97.5%.

Chapter 5: Improvements to the Film Cooling Experiment

5.1 Nozzle re-design

The original nozzle for this experiment was designed using a Method of Characteristics MATLAB code written by Maqbool. The iterative code started the nozzle by creating a sharp corner near the throat, which would result in serious disturbances. Therefore, NASA recommended a final radius was assigned to that sharp corner and throat in order to smooth the corner. However, when the code was initially run and the first nozzle designed, it suffered from an improper smoothing near the throat, which failed to remove the corner entirely. Upon review, the proper radius was implemented, resulting in an improved nozzle profile that was installed for this set of experiments.

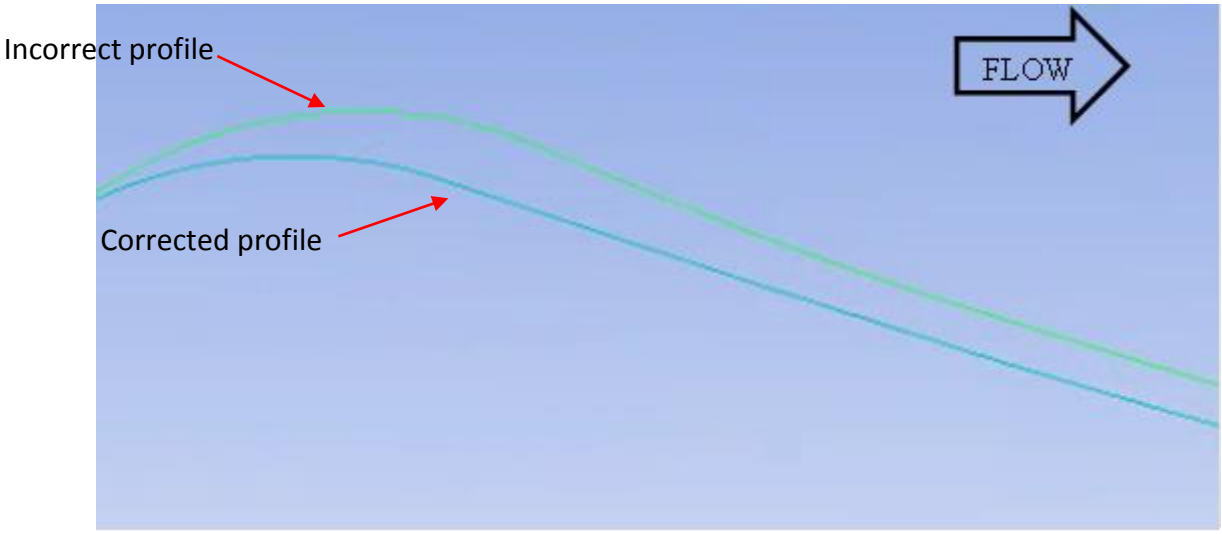

Figure 15: Nozzle comparison: close up of profile near throat.

However, this change to the nozzle meant that the upper nozzle block should have been shifted 0.203 inches downward in order to maintain an $\frac{A_{exit}}{A^*}$ ratio consistent for a M = 2.4 nozzle. Unfortunately, this was not done and the result is that all of the

data reported here were taken in a slightly underexpanded nozzle where a pair of weak oblique shocks are stabilized at the transition from the nozzle exit to the test section wall (as illustrated in Figure 29). The oblique shocks lower the free stream Mach number in the test section to 2.3. This is lower than the desired design Mach number of 2.4 but is consistent with static pressure measurements in the test section.

5.2 Wall re-design

After correcting the nozzle profile, the positions of the flow structures changed. This meant that the locations of the heat flux and pressure gauges needed to change as well. Additional heat flux gauges were also added near the anticipated impingement points of the shocks with the walls in order to measure changes in wall heat flux that may be associated with these impingements. Other gauges were added off-centerline in order to capture any three dimensional effects that might be present in. Similar to the plate thickness analysis, minimum sensor spacing was driven by the thermal penetration metric. Pressure taps were placed between the shocks impingement points in order to measure their strength.

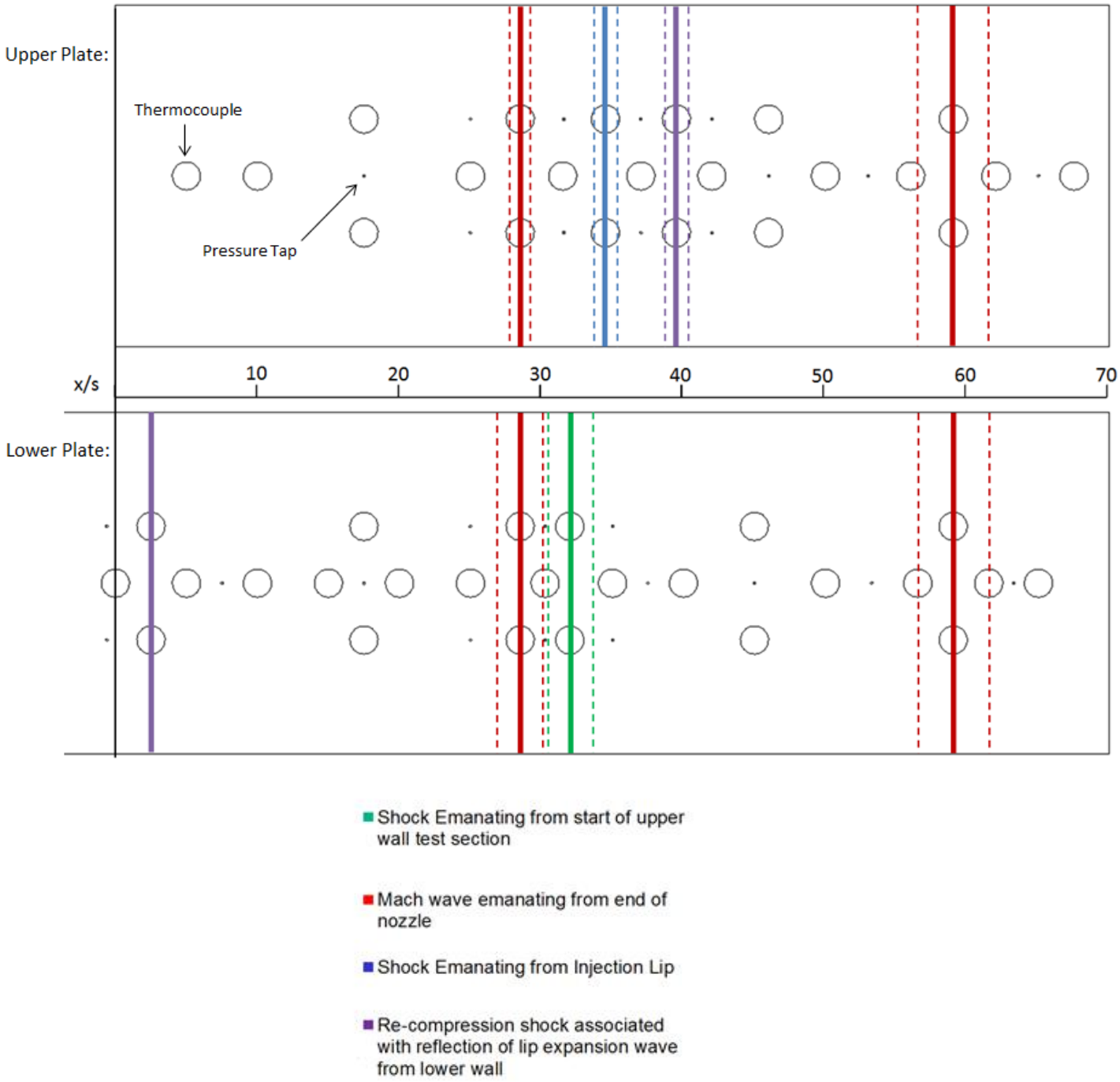

Figure 16: Heat flux gauge placement and shock location

Figure 16 shows the locations of the heat flux gauges, pressure taps, and predicted shock impingements. The dashed lines show the estimated uncertainty in

the shock impingement points. The recompression shock is only seen in the supersonic test case, but all other features are seen in all test cases. The red lines at x/s = 28 and x/s = 59 show the impingement points of the weak shocks emanating from the nozzle exit caused by the upper wall being installed slightly too high. The green line shows the impingement point of a weak disturbance associated with the gap between the upper nozzle block and the test plate, and the blue line shows the impingement point of the lip shock resulting from the flow encountering the end of the louver.

5.3 Schlieren light source upgrade

One problem encountered by previous operators of this test assembly was the light source for the Schlieren system. Maqbool and Collett used a large Spectra-Physics mercury vapor lamp, which emitted a diffuse white light. A pinhole aperture was used to restrict the lamp to a point source, but this resulted in a large drop in light intensity, as only a small fraction of the light emitted by the 72mm² lamp was able to reach the test section. So, the mercury lamp was replaced with a Luminus CBT-90 TE green LED with a more point-source-like 9 mm² light emitting area. This enabled a larger fraction of the light to reach the test section. Another advantage is the fact that the bulk of the light emitted by the green LED is in the 510-540 nm range which is where the human eye [37], and more importantly the camera's Bayer image sensor, are the most sensitive.

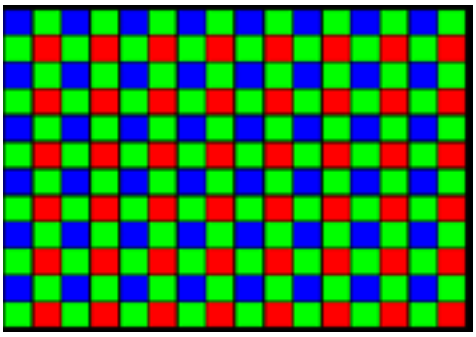

Figure 17: Bayer filter pattern (Adapted from Collett [38]*)*

5.4 Schlieren optics upgrade

Another limitation in the Schlieren measurements was the Nikkor 180-105 lens on the Nikon D-90 camera used to record the Schlieren images. As seen in Figure 18, the alignment of the Schlieren system requires at least 60 inches between the second mirror and the Schlieren stop to achieve a point focus. At this distance, the image of the test section did not fill the camera's CCD resulting in lower quality (i.e. degraded spatial resolution) images of the test section. Replacing this lens with a Nikkor 70-300 mm lens resulted in a higher quality image due to the more complete usage of the CCD.

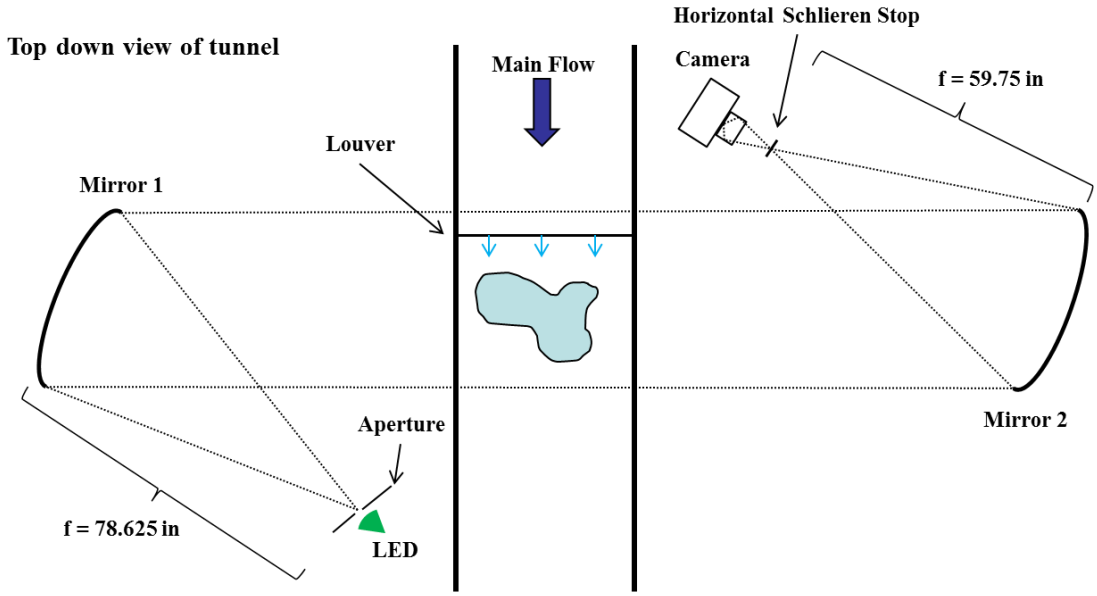

Figure 18: Schlieren alignment requirements

5.5 Film heater upgrade

Though the previous propane film heater was capable of heating the film flow to the desired temperature of 45°C, it suffered from several limitations. In the lower film flow cases, the amount of air flow and therefore fuel needed for combustion was very small, so it was difficult to ensure stable combustion. Even in the supersonic film condition where the heater operated more stably, the film temperature climbed by more than 10 degrees over the course of the 6 second experiment. This is undesirable as the film temperature is assumed to be a constant 323 K in the numerical simulations.

The heating element from an electric heat gun turned out to be a suitable substitute for the propane heater. Figure 19 compares temperatures measured at the film plenum inlet and the center of the film plenum when the film is heated using the propane burner, and Figure 20 shows the two temperatures when the film is heated

with the electric heater. The electric heater was able to hold the target temperature of 318 K to within 2 K over the course of an experiment. This is much better than the propane heater where the film temperature varied 7 K over the course of the experiment.

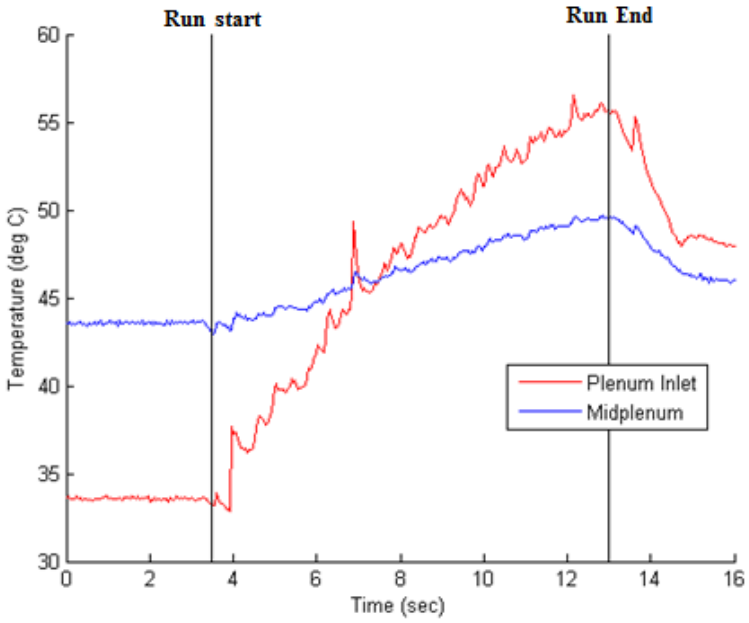

Figure 19: Propane heater measurements (Test Case 2)

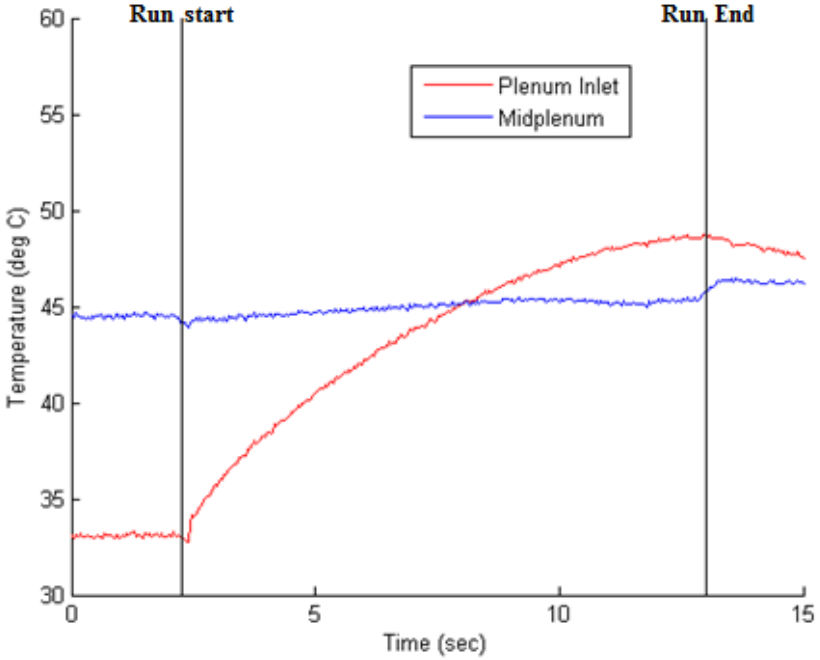

Figure 20: Electric heater measurements (Test Case 2)

5.6 MACOR plate failure and repair

A crack developed in the MACOR under the film louver after 45 to 50 runs and could be due to aerodynamic stresses on the MACOR plate under the lip. The extent of the crack was revealed with dye as seen in Figure 21.

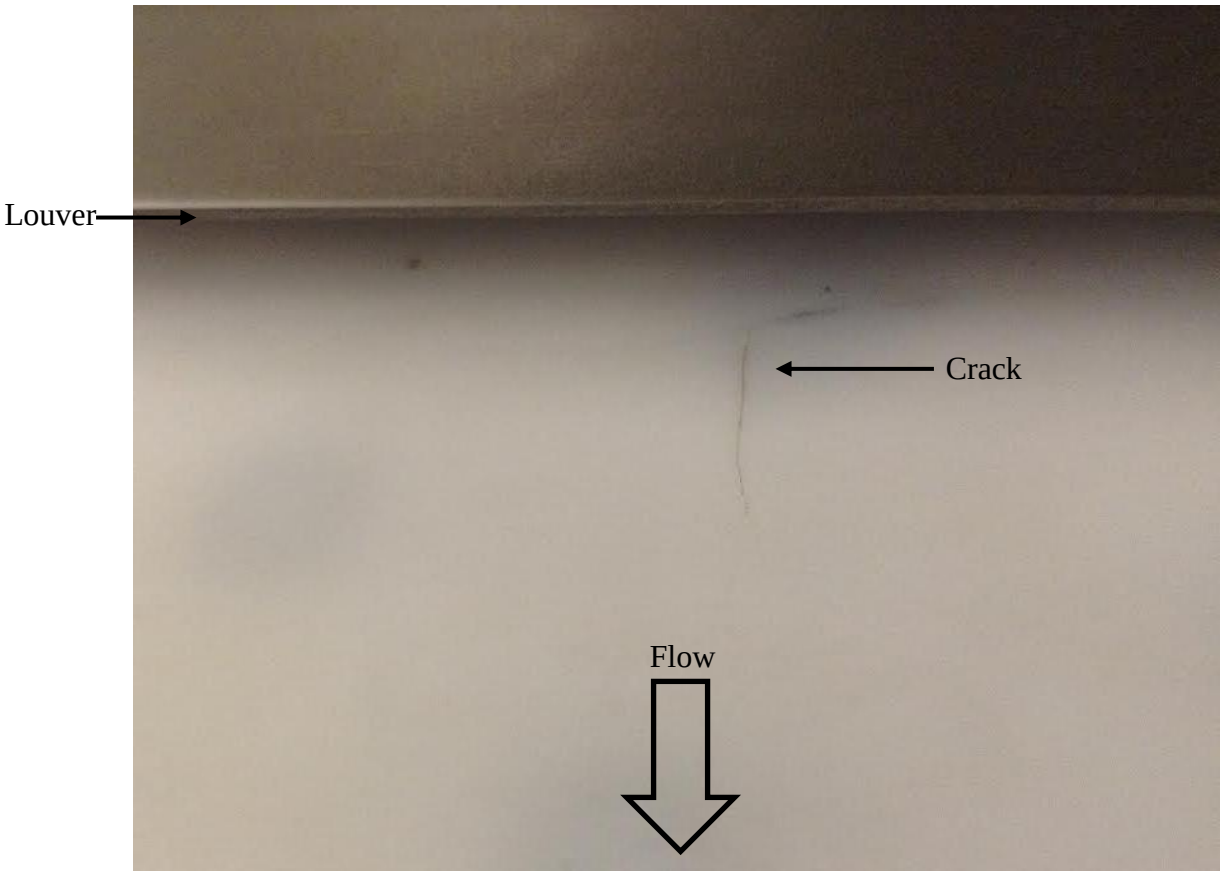

Figure 21: Initial lip crack in MACOR plate

Upon consultation with Howard Grossenbacher of the University of Maryland Aerospace machine shop and the MicaTron Corporation, several 1/8” holes were drilled at the terminal points of the cracks in order to distribute the stress concentrations in the area and reduce the chances of the cracks continuing to propagate. The holes were then filled with epoxy to maintain a smooth plate surface. The process was successful, with no further crack propagation in this area until the ultimate downstream failure occurred.

Figure 22: MACOR crack repair

After approximately 125-150 run cycles and several uninstallations and reinstallations, the downstream attachment points between the MACOR and aluminum assembly structure failed in the first several seconds of a Case 3 run (maximum film pressure, see Figure 23). The test stopped before total failure occurred. This plus the 1/16 inch gap between the walls in the re-designed test section prevented the tunnel from being damaged, but the lower MACOR plate was damaged beyond repair.

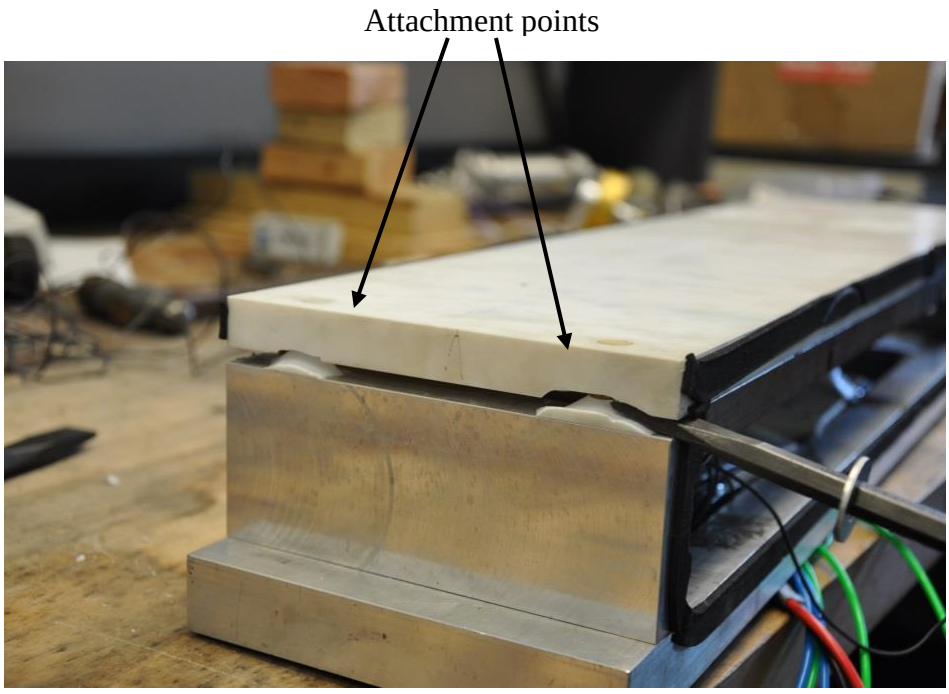

Figure 23: Downstream plate failure

Upon review, it appears that the entire force associated with the pressure difference between the free stream and film plenum was borne by two thin countersunk holes in the MACOR. This was not a good design and could also have possibly been the source of the bending moment that created the upstream crack underneath the louver. The lower plates were replaced and an additional structure was added (Figure 24) to attach the aluminum structure to the copper backing plate and ensure that the full plenum pressure was not borne by the thin countersunk holes in the MACOR.

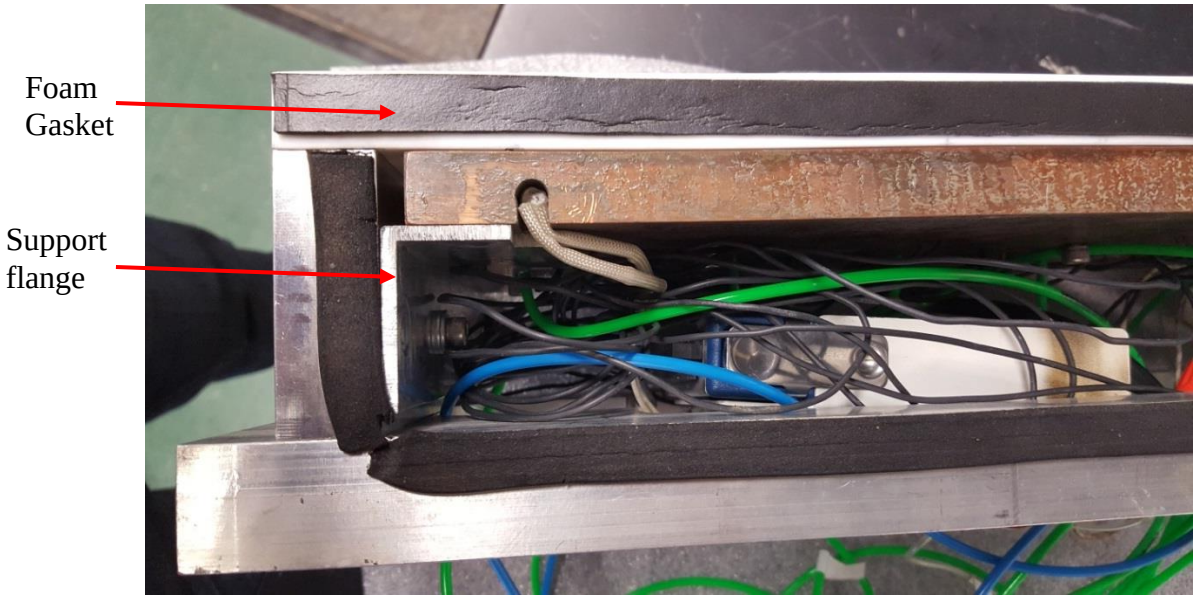

Figure 24: Downstream support structure

5.7 Experimental timeline

Table 5: Experimental Timeline

	Tasks completed
Summer 2014	Redesigned and machined new nozzle profile. Started taking basic Schlieren measurements.
Fall 2014	Redesigned and ordered new MACOR plates. Installed new Schlieren lens and improved Schlieren instrument.
Winter 2014	Recorded high quality Schlieren measurements of Test Case 0. Rebuilt upper and lower tunnel walls, started recording heat flux data.
Spring 2015	Recorded a large quantity of heat flux data and Schlieren images in all four test cases. Identified and repaired leak in Test Case 0 film flow. Implemented new film heater. Experienced lower wall failure.
Summer 2015	Investigated heat flux measurement discrepancies. Began Favorable Pressure Gradient design. Began construction of lower wall full plate test assembly.
Fall 2015	Examined temporal and temperature sensitivity of heat flux measurements. Continued Favorable Pressure Gradient design.
Winter 2015	Constructed and installed downstream structural support. Built new lower wall instrument.
Spring 2016	Conducted additional tests in Test Case 0 and Test Case 3 with new lower wall instrument.

Chapter 6: Experimental Results: Film cooling

6.1 Overview of testing

Between winter of 2014 and spring of 2016, data from over 100 runs were recorded and analyzed. Due to some leaks present in Test Case 0 and the film heater rebuild, some of the data had to be recollected, so an average of 15 runs per test case was achieved across all test cases.

Table 6: Summary of improvements to experiment

	Previous Work	**This Work**
Nozzle Profile	Incorrect	Corrected
Runs per Test Case	10 (5 for supersonic)	15
Schlieren Image Size	18s x 11s	34s x 24s
Heat Flux Measurement locations/run	24	45
Film Heater	Propane	Electric

6.2 Effect of initial wall temperature on wall heat flux

Figure 25 and Figure 26 show the average temperatures after the tunnel walls were heated and the tunnel was pumped to vacuum, but before the run was started. Due to finite heating points, plate features, and the time it took to heat the plates, it was not always possible to achieve a perfectly even temperature profile. The goal was 340 K before the run began, but the upper wall was difficult to heat above ~335 K due to heat loss to the upper tunnel structure and temperatures much above 335K causing the thermocouple modules in the upper wall to overheat and shut down.

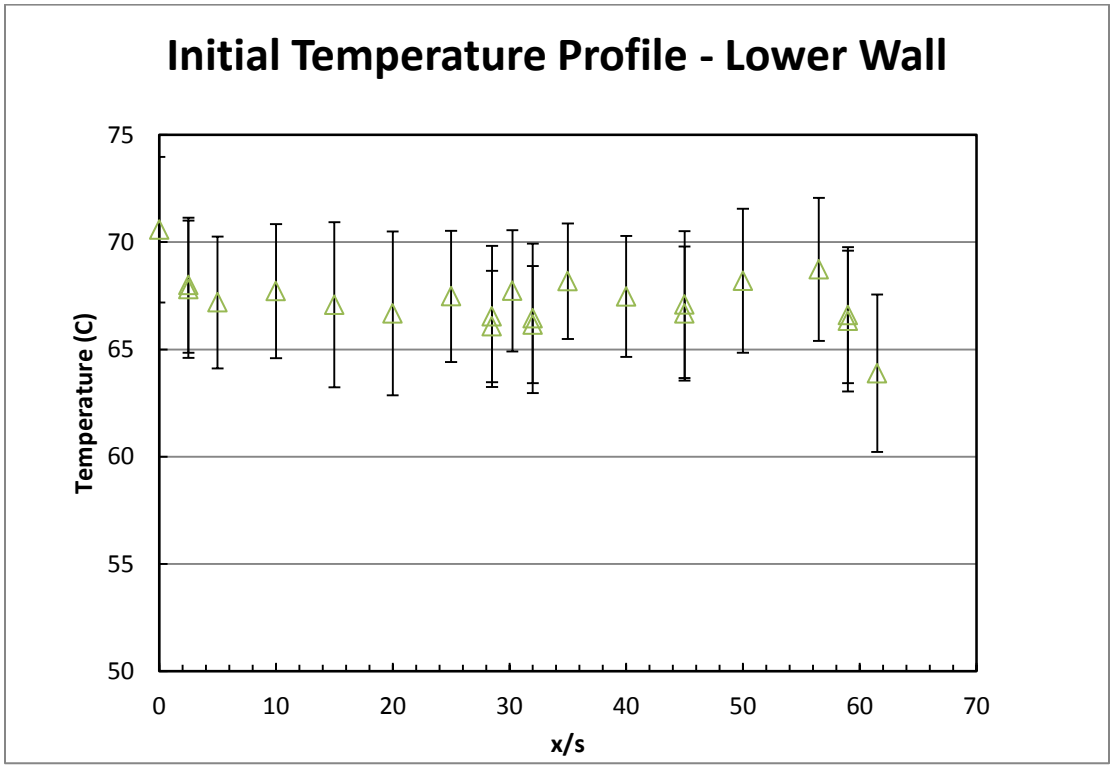

Figure 25: Initial temperature profile for the upper wall before start of run (N = 50)

Figure 25 shows the average lower wall temperature before the start of the run. The temperature was typically about 67 degrees +/- 1 degree, with a standard deviation of about 3 degrees. The gauge under the louver was slightly hot, as the louver radiated heat back down towards it. The gauge at the end of the test section was slightly cold, as there was no heating element at the end of the test plate.

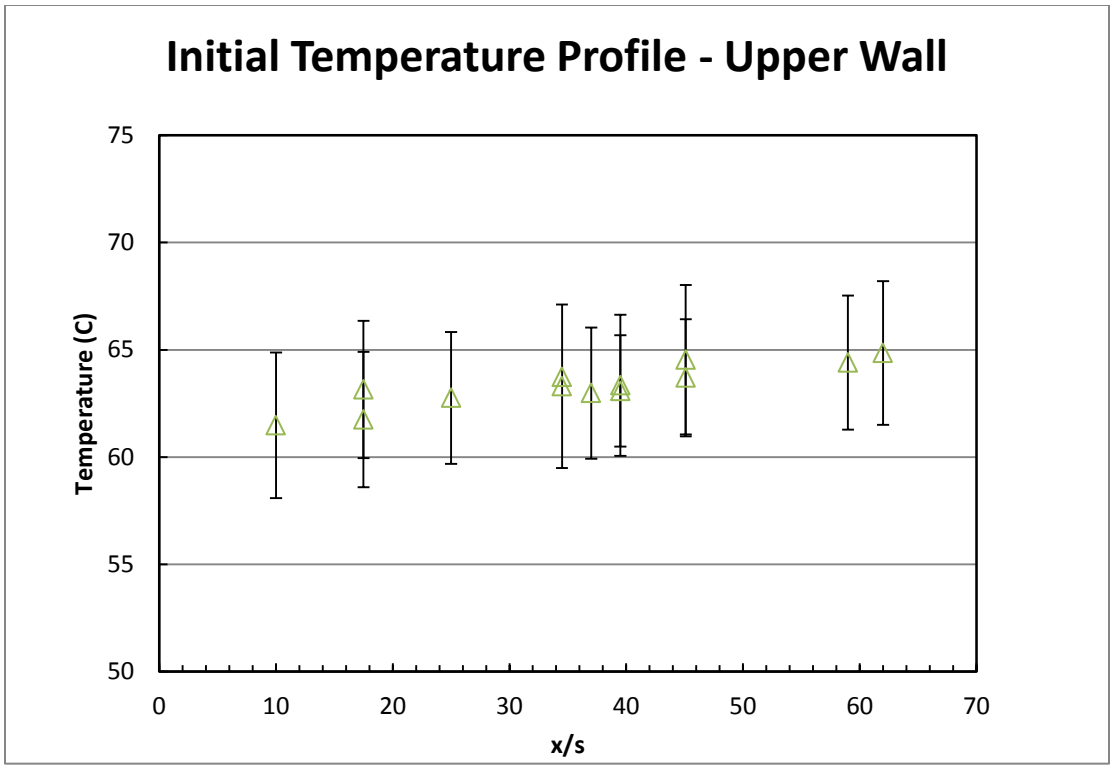

Figure 26: Initial upper wall temperature before start of run (N = 50)

Figure 26 shows the average upper wall temperature before the start of the run. The temperature was typically about 63 degrees +/- 2 degrees, with a standard deviation of about 2 degrees. The gauges near the upper nozzle block were slightly cold, as the plate conducted heat away to the nozzle structure in that direction. The gauges at the end of the test section were slightly hot, as there was a heater under the end of the test plate.

In order to determine if the initial temperature had an effect on the heat flux, a set of measurements with varying initial temperatures were processed. Several gauges were sampled with similar trends, the results of one gauge at x/s = 5 are shown below.

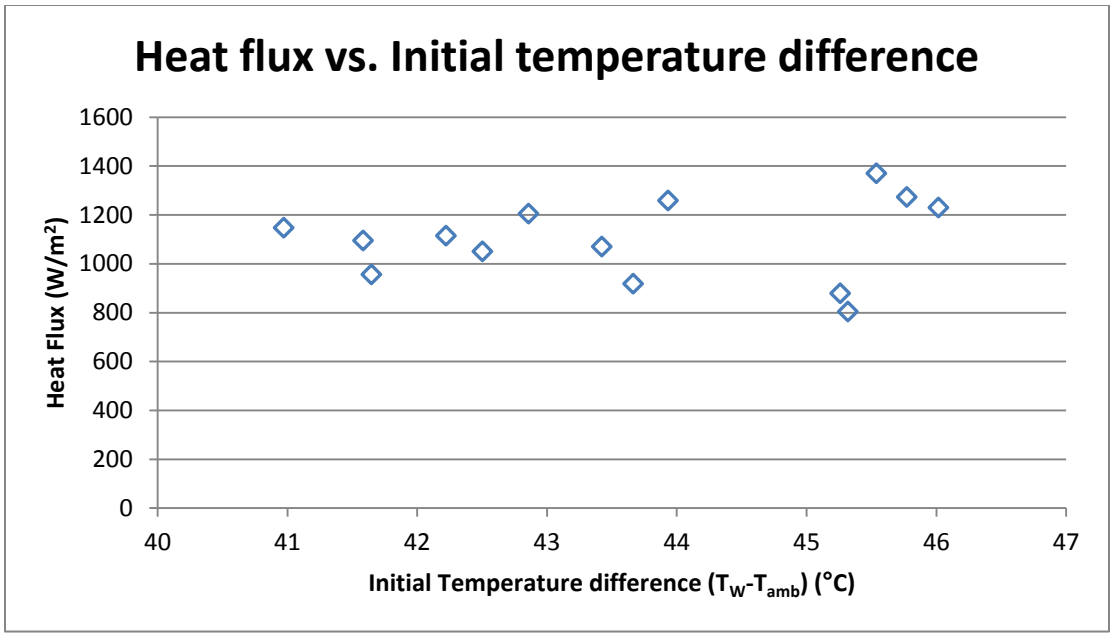

Figure 27: Heat flux vs. Initial temperature difference

Figure 27 shows that there is little to no correlation between initial wall temperature (presented here as difference from the ambient temperature, or $T_w - T_{amb}$) and wall heat flux.

6.3 Test Case 0

6.3.1 Summary of experimental conditions

Table 7: Test Case 0 Summary Table

$\boldsymbol{T_{0,ambient}}$	295 K
$\boldsymbol{P_{0,ambient}}$	1 atm
$\boldsymbol{T_{0,film}}$	N/A
$\boldsymbol{P_{0,film}}$	N/A
$\boldsymbol{M_{film}}$	N/A
$\boldsymbol{u_{film}}$	N/A
Film throttle valve setting	0% (Fully closed)

Film heater setting	0 (Off)
$\boldsymbol{T_{wall}}$	~335 K
$\boldsymbol{M_c = \frac{U_\infty - U_f}{a_\infty - a_f}}$	1.64
$\boldsymbol{\lambda = \frac{\rho_f U_f}{\rho_\infty U_\infty}}$	N/A
$\boldsymbol{s = \frac{\rho_f}{\rho_\infty}}$	N/A
$\boldsymbol{r = \frac{U_f}{U_\infty}}$	N/A

Test Case 0 is the 'baseline' situation corresponding to flow over an unprotected wall. It can thereby be considered one choice for the reference heat fluxes for the experiment which can be used to quantify the protection offered by the other cases. The other reference case will be the unprotected upper wall.

6.3.2 Flow structures

In Test Case 0, the absence of a film flow makes the case analogous to that of supersonic flow over a rearward facing step. This is a well-studied canonical problem whose physics are fairly well established. As such, it provides a control case of sorts that may be compared to other flows. Figure 28 from Smith [39] shows the structures that are expected to be present in the flow downstream of the louver.

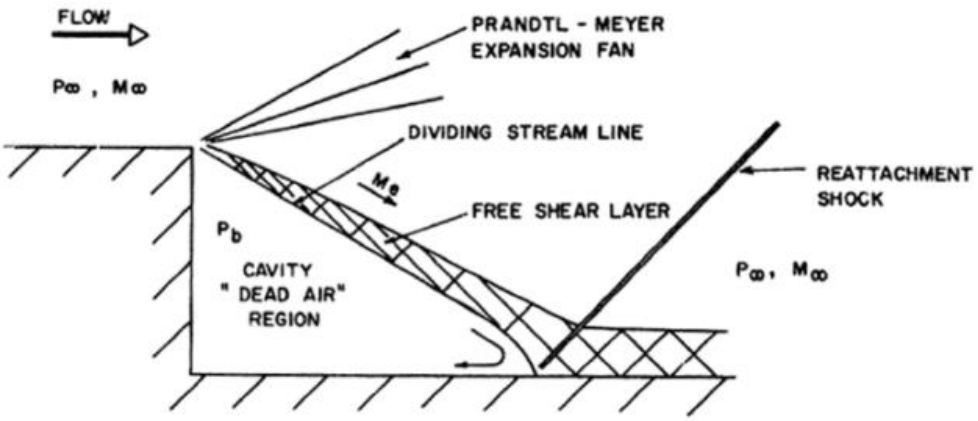

Figure 28: Supersonic flow over a rearward facing step (From Smith [39]*)*

A Prandtl-Meyer expansion fan attached to the upper edge of the rearward facing step turns the flow downward creating a small recirculating region in the lee of the step. A shear layer forms between the free stream and the recirculation region. A normal shock forms where the shear layer meets the bottom wall and turns the shear layer so that it continues along the bottom wall.

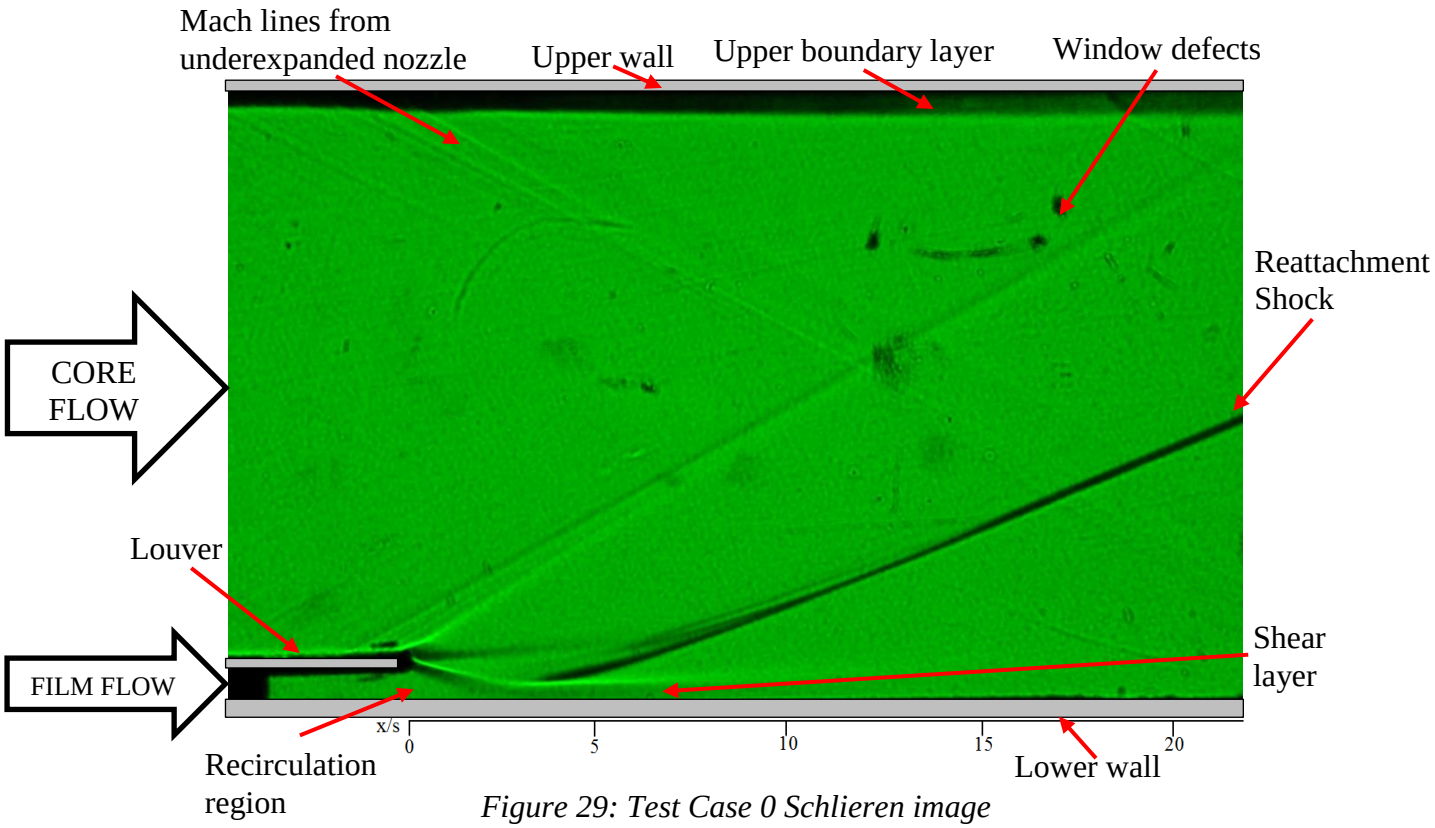

Figure 29: Test Case 0 Schlieren image

Figure 29 is a Schlieren image of the Case 0 flow. Most of the flow features identified in Figure 28 like the recirculation region, expansion fan, reattachment shock, and shear layer, are clearly visible. A boundary layer can also be seen growing on the upper wall, and is most clearly seen in the transparent area on the upper right side of the leftmost image. Contrast makes the boundary layer appear fainter in the other two images, but it can be seen weakly along the upper wall along the rest of the test section. The extra expansion due to the incorrect test section height can be seen as faint Mach waves emanating from the top and bottom of the nozzle on the left side of the image. The dark smudges present in the upper right region are due to scratches on the wind tunnel windows, and are not flow features.

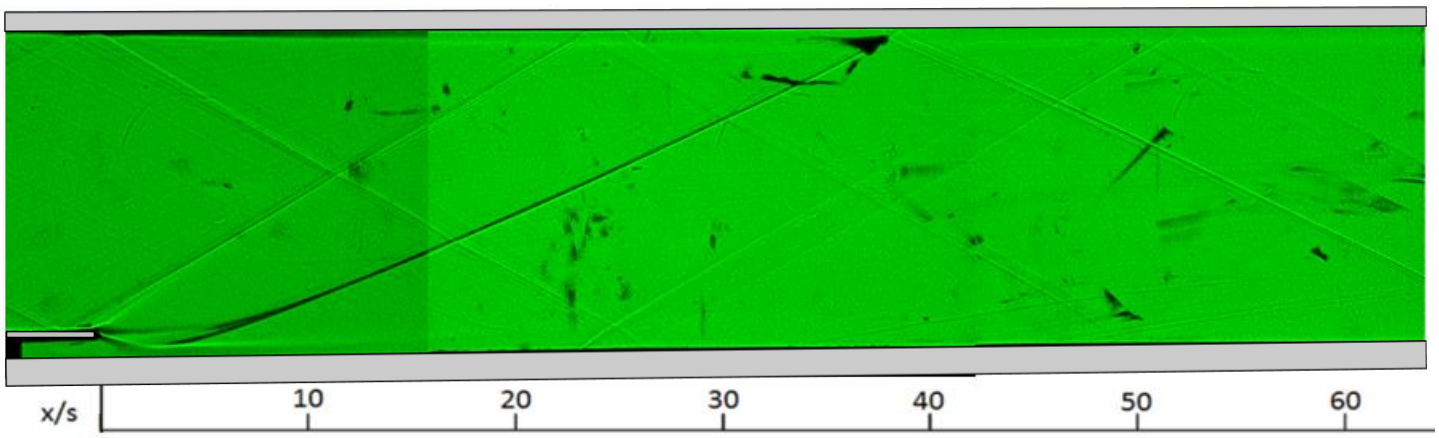

Figure 30: Test Case 0 Schlieren image, full tunnel

Figure 30 is a composite image of the flow created by acquiring Schlieren images at two other downstream locations (at the same flow conditions) and stitching the resulting set of three images together in post-processing. Though the image quality is compromised by scratches on the test section windows, the interaction of the lip shock with the upper wall can be seen clearly. The image also shows that the lower wall shear layer is almost fully mixed out after x/s = 10 and the upper wall boundary layer is visible along the whole length of the test section. Due to the difficulty of moving and calibrating the Schlieren assembly, the stitched set of images was only constructed for Test Case 0. Slight misalignment of the camera mount with the flow direction causes the set of images to look ‘tilted’ to the left.

6.3.3 Upper Wall heat flux

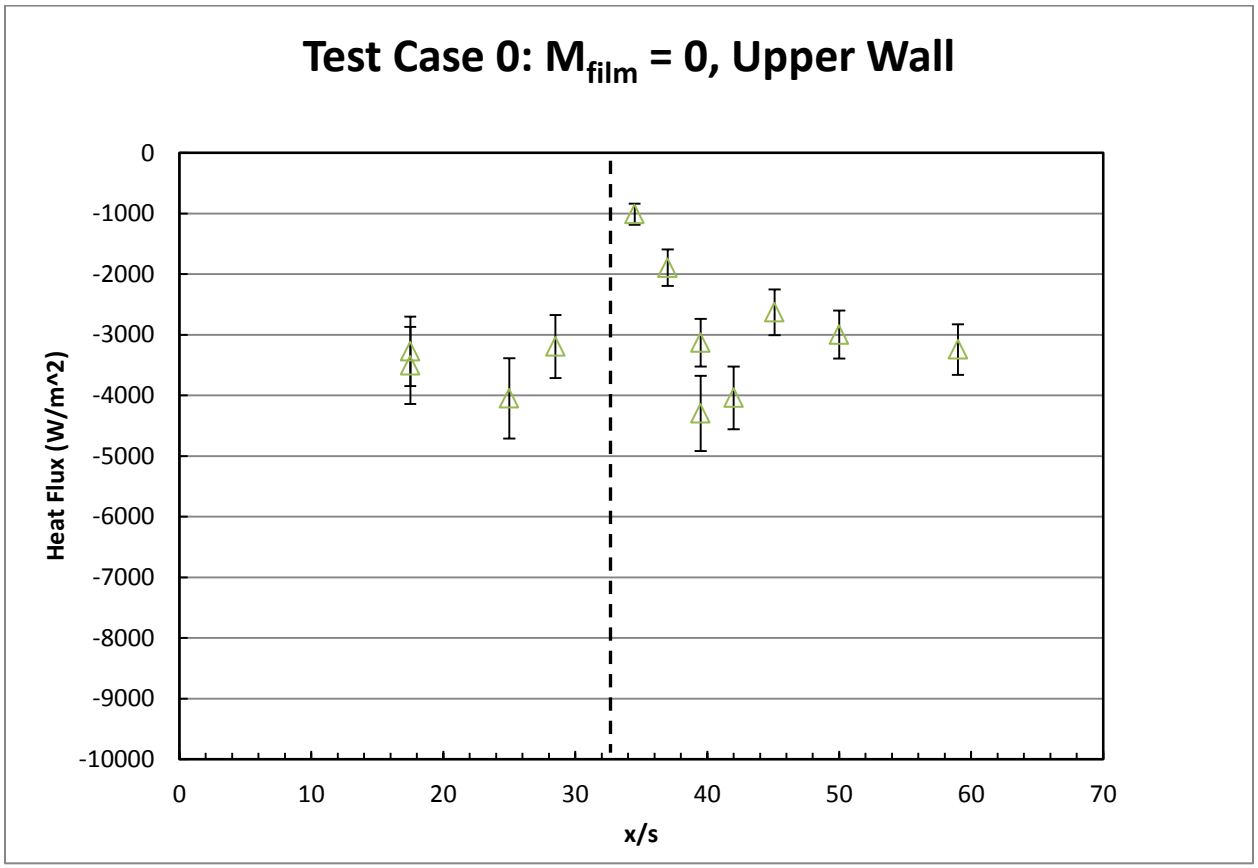

Figure 31: Test Case 0 upper wall heat flux. Dashed lines denote the location of the lip shock impingement as determined by Schlieren (N = 15).

Figure 31 is a plot of heat flux distribution along the upper wall. While the data are scattered, they show that the heat fluxes on the upper wall are of the same order of magnitude as those along the lower wall. The sudden drop in heat flux followed by a slower increase in heat flux from ~30 < x/s <~42 occurs where the expansion fan from the louver lip intersects the upper wall.

6.3.4 Lower Wall heat flux

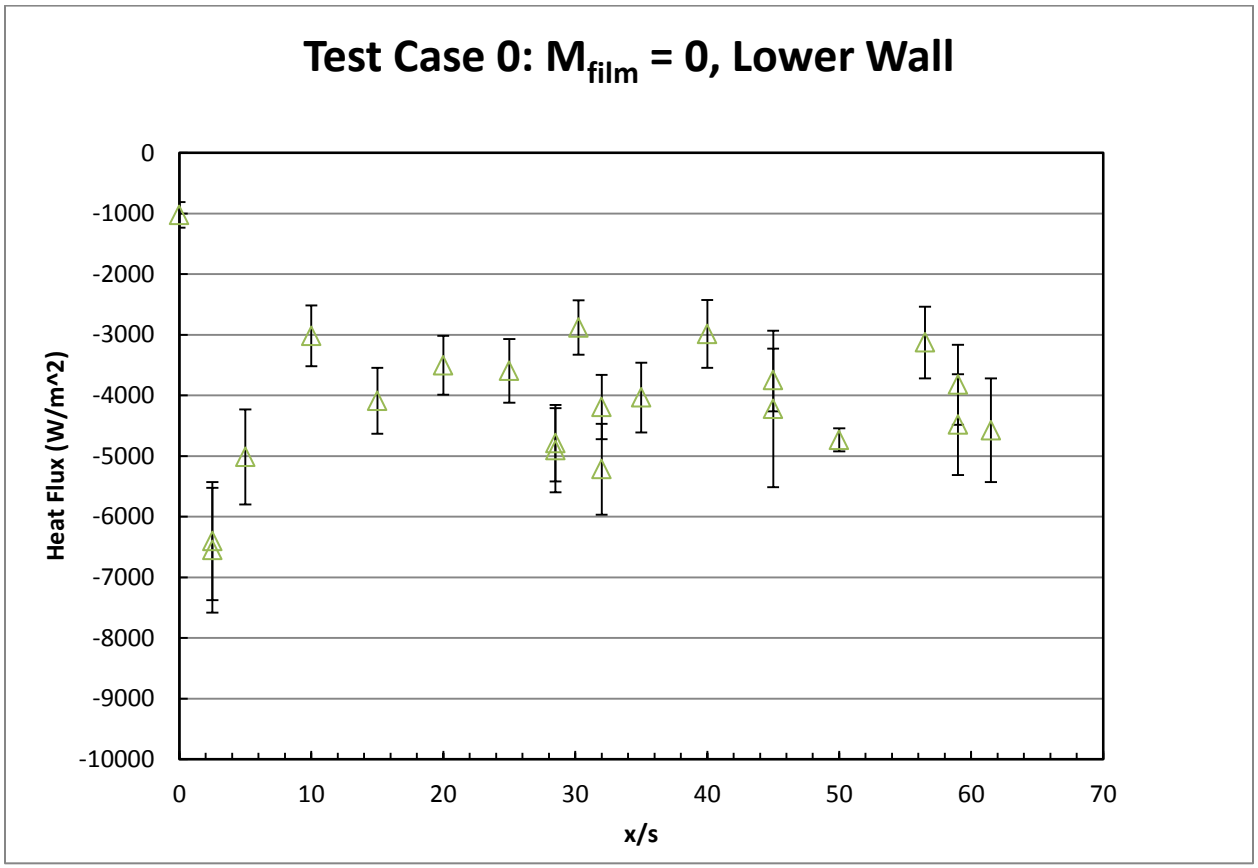

Figure 32: Test Case 0 lower wall heat flux (N = 4)

Figure 32 is a plot of heat flux along the lower wall as a function of non-dimensional distance downstream of the louver in Case 0. The data show that the heat flux peaks at ~6500 W/m^2 at x/s~2.5 (where the reattachment shock leaves the wall as illustrated in Figure 29) and then drops to 5000-3000 W/m$^{2.}$ Only 4 runs were taken in this configuration due to a flow leak that will be covered in 6.3.5 Effect of flow leak.

6.3.5 Effect of flow leak

Earlier Schlieren images indicated that a small film flow was present even when the film valve was fully closed. This problem, which went undiscovered for a

while, turned out to be the result of modifications made to the MACOR walls and support structure after a failure scratched the wind tunnel windows. After the failure, the width of all test section components (i.e. the new MACOR walls and nozzle contraction) was reduced to prevent them from contacting the windows. The resulting 1/16 inch gap between the walls and windows was sealed using a soft foam gasket. The gasket allowed a small amount of the main flow to leak from the upstream end of the nozzle contraction, through the foam between the nozzle structure and window, into the film plenum and out through the film nozzle. This leakage was stopped by inserting a wooden block in the film flow path behind the louver discharge plane and sealing it with clay.

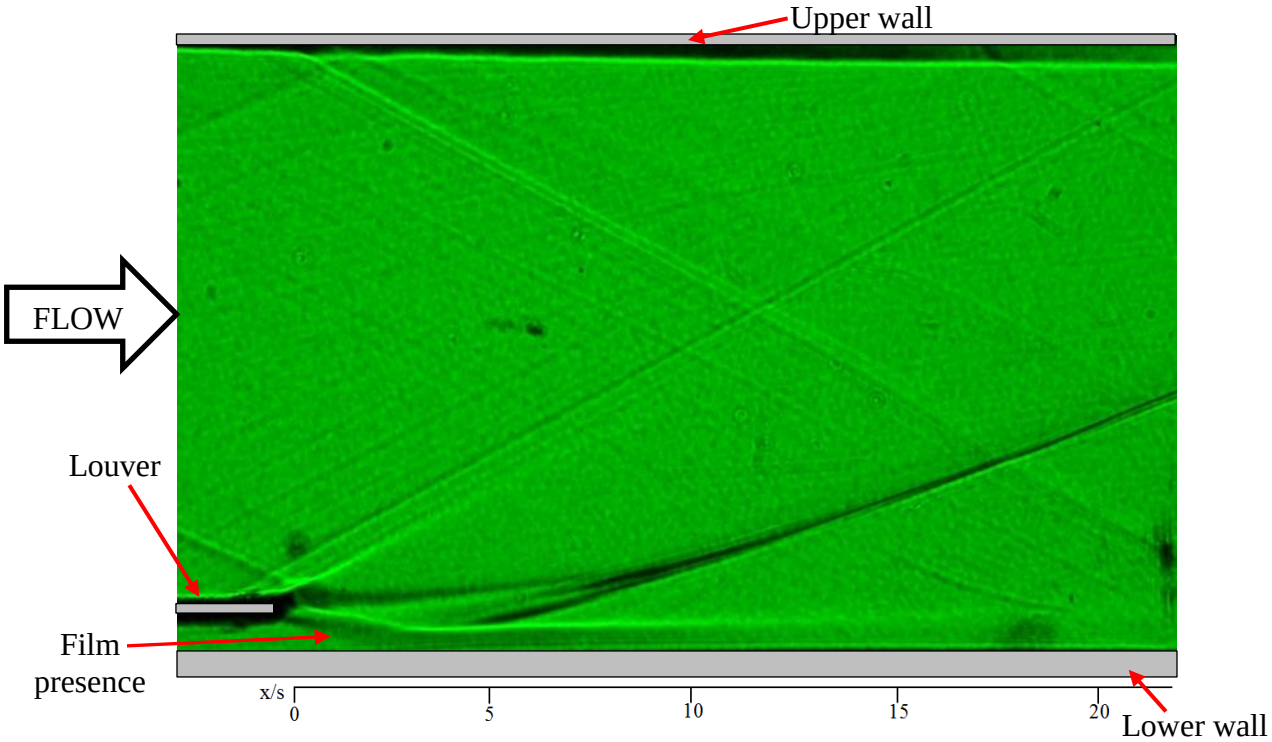

Figure 33: Schlieren image of Case 0 before film block addition

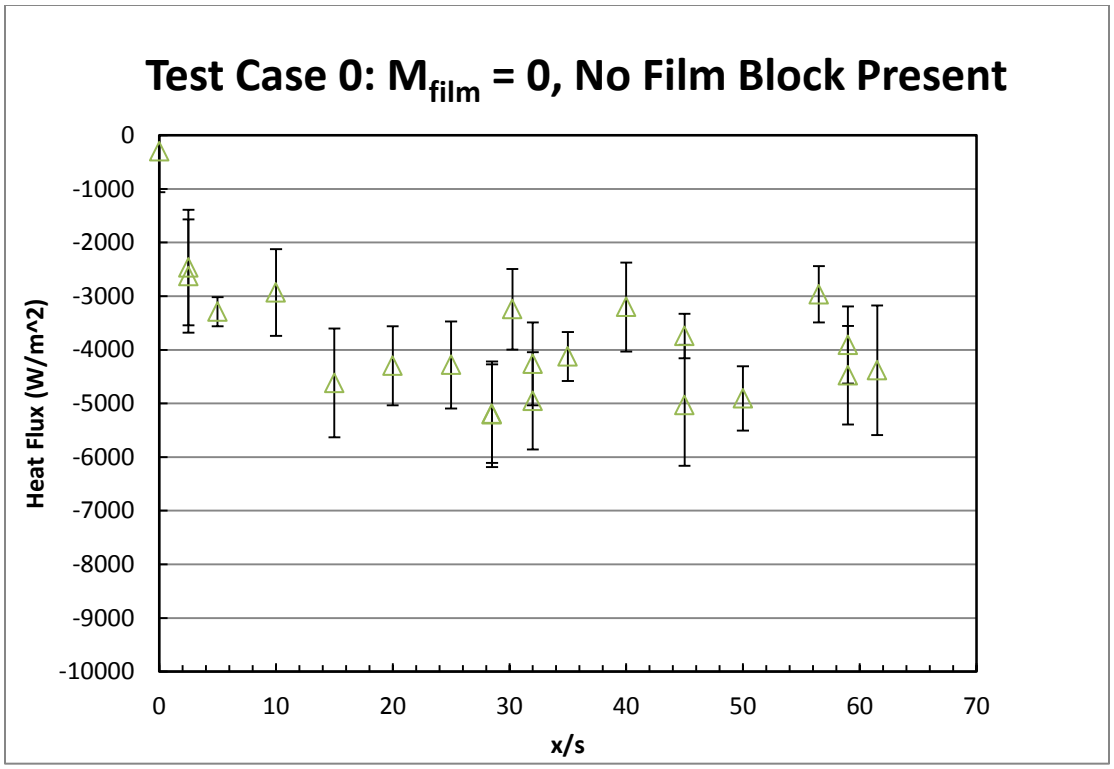

Figure 34: Test Case 0 heat flux with no block present (N = 15)

Figure 34 shows the heat flux without a block present under the louver. There is no heat flux increase when the flow initially turns around the louver, which raised concerns that there was still some film escaping and causing a slight protection region.

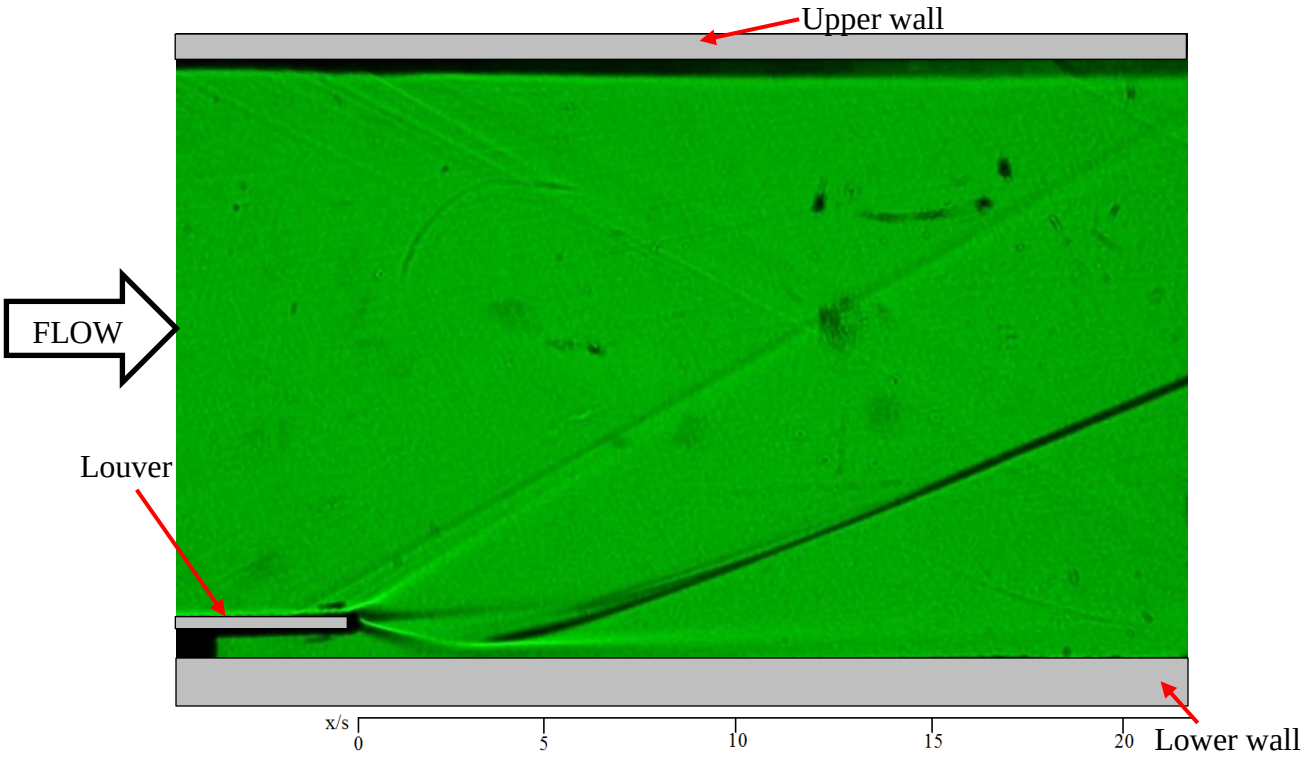

Figure 35: Schlieren image of Case 0 after film block addition

In Figure 35, the film presence downstream of the louver seen in Figure 33 is no longer visible. This can be confirmed by the sharp heat flux increase expected when the flow initially turns around the louver into an unprotected wall, seen in Figure 32.

6.3.6 Improved lower wall heat flux measurements

The large amount of scatter in regions that should be free from any flow structure impingement or other factors that would affect heat transfer was concerning and ultimately led to the construction of a new set of instrumented plates. Great care was taken in there construction to ensure that the wall thermocouples were in the proper positions and that all had been thoroughly potted in thermal grease with no air gaps.

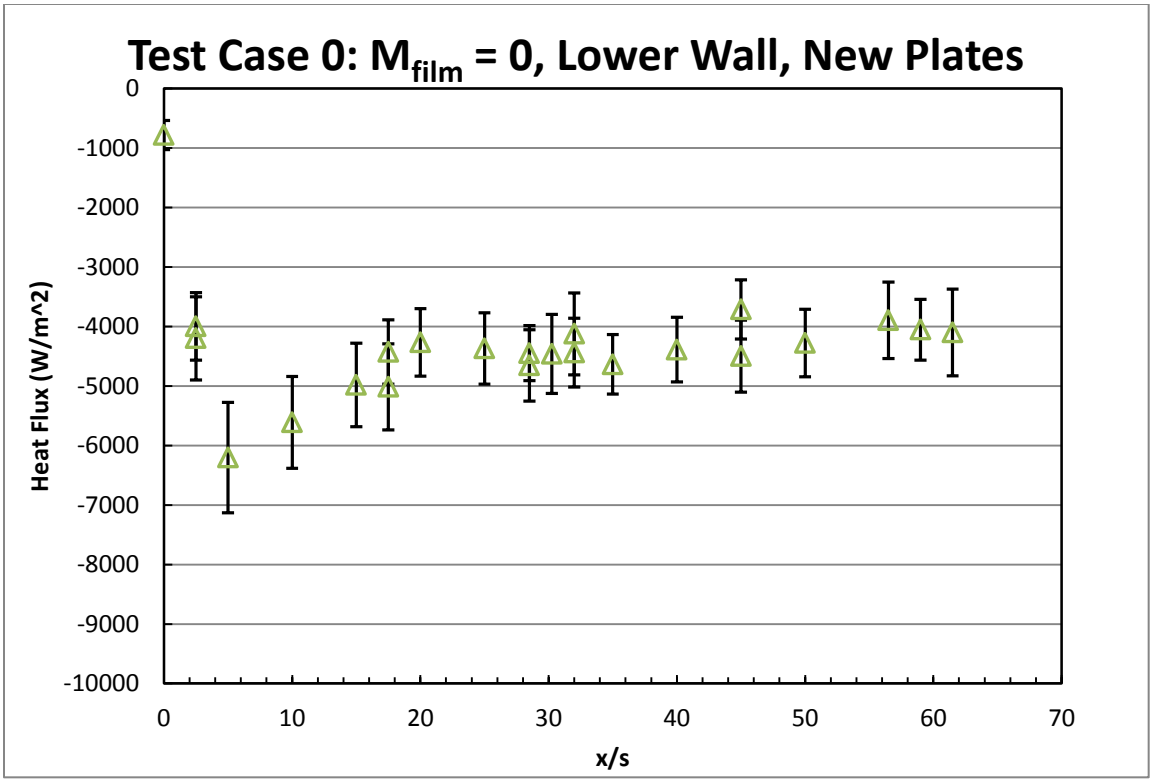

Figure 36: Test Case 0 heat flux with new instrument (N = 14)

The measurements resulting from temperature-time histories recorded using the new plates are plotted in Figure 36. While the trend and overall order of magnitude of the heat fluxes are comparable to those presented in Figure 32, there is much less scatter. Unfortunately, time constraints did not permit re-running all of the experiments in the test matrix and only data for Cases 0 and 3 (with N = 15 experiments for each case) were acquired.

6.4 Test Case 1

6.4.1 Summary of experimental conditions

Table 8: Test Case 1 Summary Table

$\boldsymbol{T_{0,ambient}}$	295 K
$\boldsymbol{P_{0,ambient}}$	1 atm
$\boldsymbol{T_{0,film}}$	318 K
$\boldsymbol{P_{0,film}}$	0.06 atm
$\boldsymbol{M_{film}}$	0.5
$\boldsymbol{u_{film}}$	280.4 m/s
Film throttle valve setting	10% (Mostly closed)
Film heater setting	6 (Medium)
$\boldsymbol{T_{wall}}$	~335 K
$\boldsymbol{M_c = \frac{U_\infty - U_f}{a_\infty - a_f}}$	0.65
$\boldsymbol{\lambda = \frac{\rho_f U_f}{\rho_\infty U_\infty}}$	0.14
$\boldsymbol{s = \frac{\rho_f}{\rho_\infty}}$	0.43
$\boldsymbol{r = \frac{U_f}{U_\infty}}$	3.13

Case 1 corresponds to a subsonic film of M=0.5. Features are similar to Test Case 0 because the injection velocity is relatively low.

6.4.2 Flow structures

Figure 37 is a Schlieren image showing flow structures near the louver exit in Case 1. Clearly visible in the image are a shock originating slightly downstream of the edge of the louver and an interface between the film and core flows.

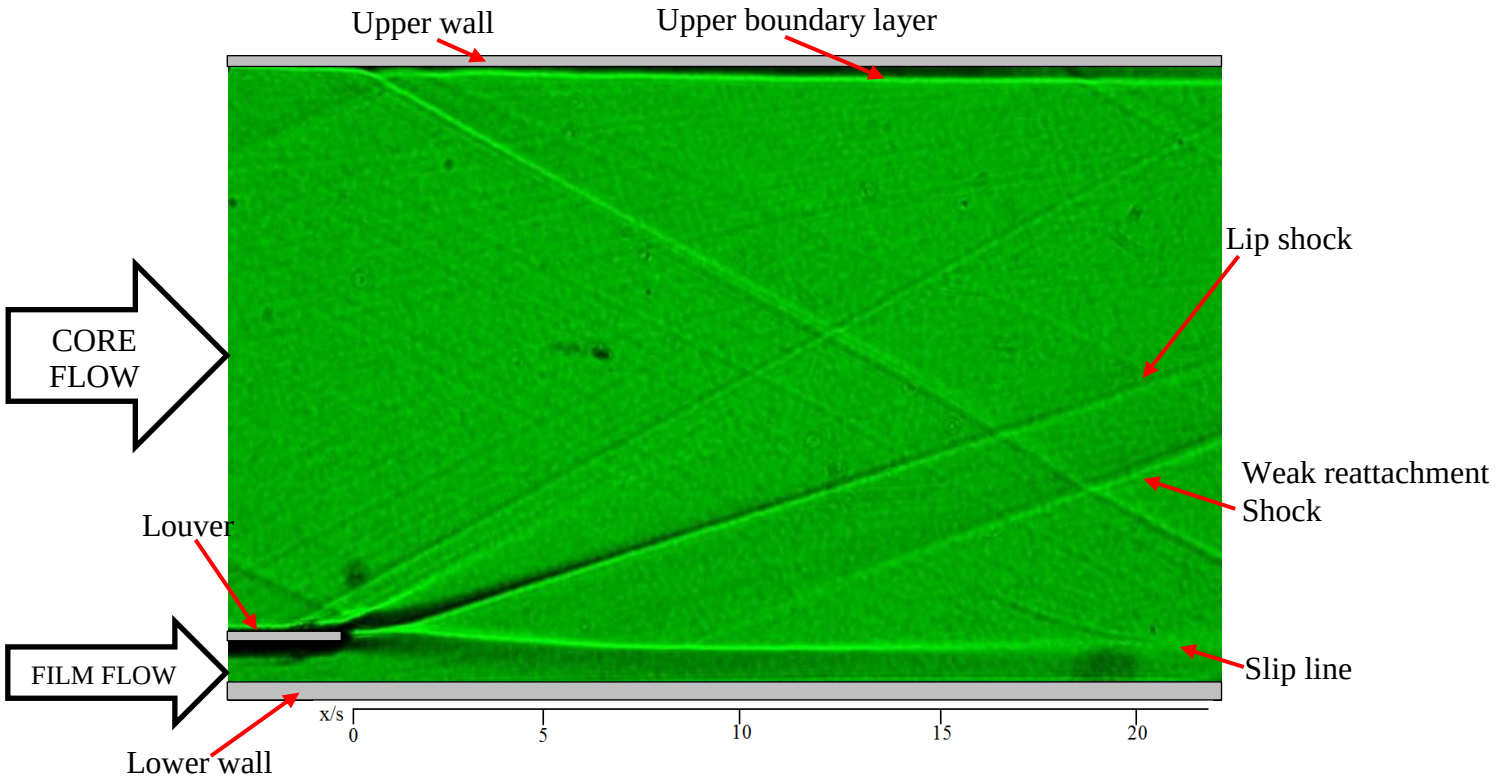

Figure 37: Test Case 1 Schlieren image

As in Case 0, the core flow initially turns downward behind the louver through an expansion fan centered on the upper edge of the louver. However, the film flow emanating from the louver prevents the core flow from contacting the lower wall and the core flow is turned back through a system of converging expansion waves which coalesce into a shock that appears to emanate slightly downstream of the trailing edge of the louver. Momentum transfer across the shear layer accelerates the film and the need to conserve mass causes the interface between the film and core to slope downward after the lip shock. No more decreases in flow area are required once the film has stopped accelerating, so a weak reattachment shock forms to turn the core flow parallel to the wall. This physical reasoning leads to the sketch of basic flow features presented in Figure 38. The interface between the film and core flows becomes less distinct as one moves downstream of the reattachment shock and

disappears entirely by x/s ~20 indicating that the flows have become well mixed. This suggests that the thermal protection offered by the film will be diminished and this is consistent with the heat flux measurements presented in Figure 40.

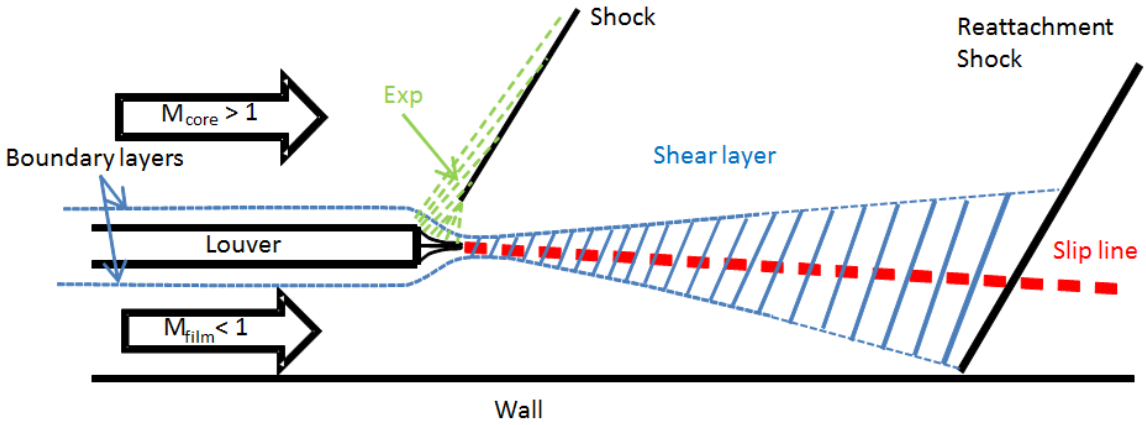

Figure 38: Supersonic flow-subsonic film at M=0.5 interaction

6.4.3 Upper Wall heat flux

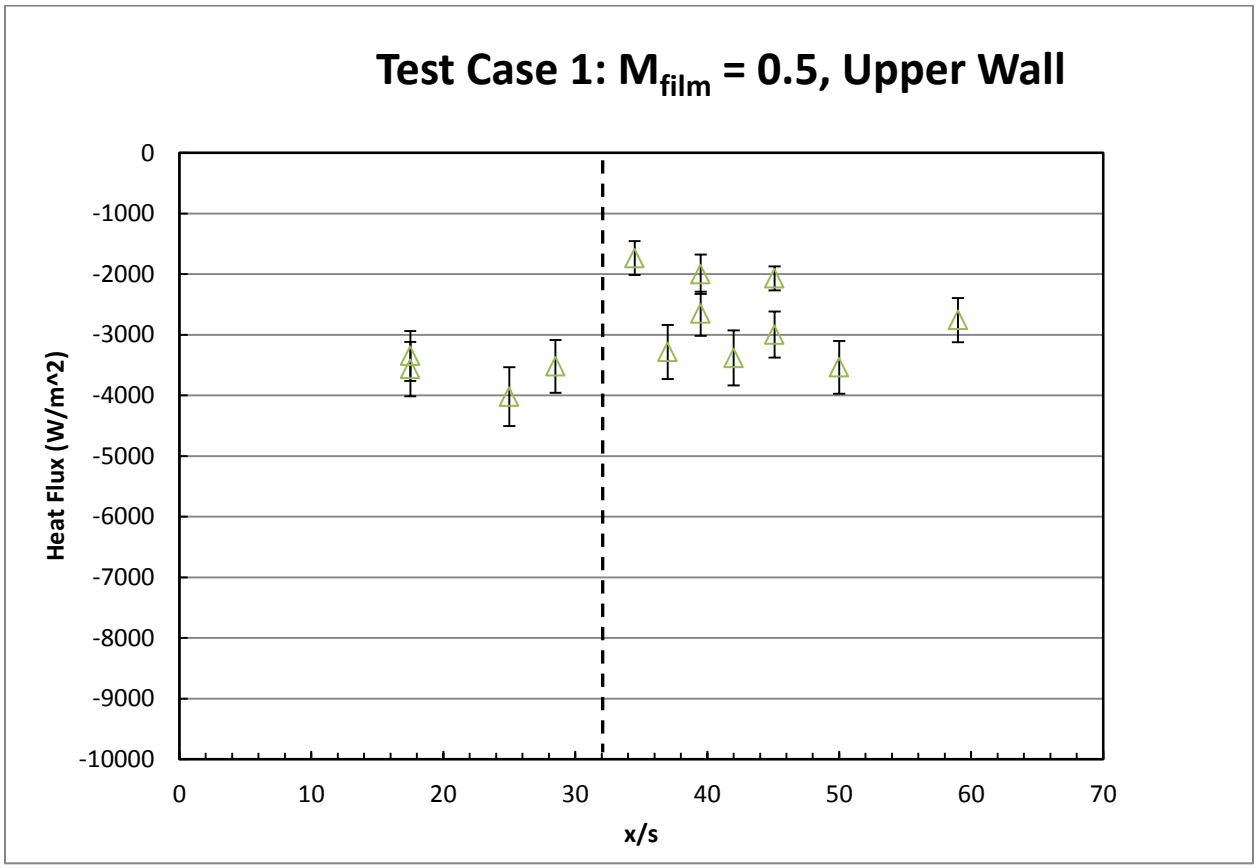

Figure 39: Test Case 1 upper wall heat flux. Dashed lines denote the locations of the lip shock impingement as determined by Schlieren. (N = 16)

Figure 39 shows the heat flux distributions along the upper wall in Case 1. The decrease in heat flux in the ~30 < x/s < 40 range suggests that this is where the expansion fan/shock system originating from the louver edge strikes the upper wall. The change in heat flux is smaller, however, because the core flow undergoes less turning at the louver exit leading to a weaker expansion wave and shock.

6.4.4 Lower Wall heat flux

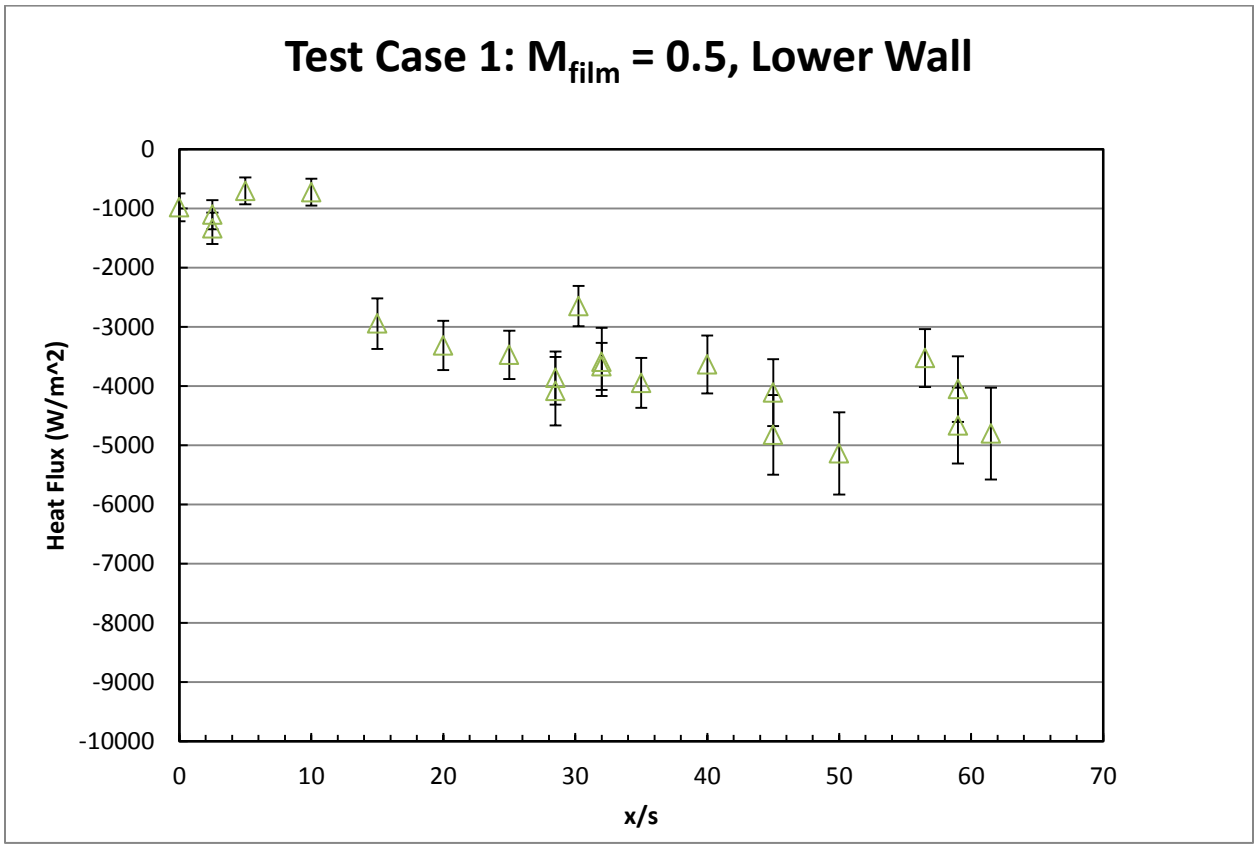

Figure 40: Test Case 1 lower wall heat flux (N = 16)

Figure 40 shows the heat flux distribution along the lower wall in Case 1. The turning of the core flow towards the lower wall is now prevented by the film flow layer, which results in a short region of film protection extending to x/s~10 where the recompression shock originates and the heat flux triples from ~1000 W/m^2 to ~3000 W/m^2. The heat flux continues to increase beyond this point but at a much slower rate indicating that some protection remains after the recompression shock.

6.5 Test Case 2

6.5.1 Summary of experimental conditions

Table 9: Test Case 2 Summary Table

$T_{0,ambient}$	295 K
$P_{0,ambient}$	1 atm
$T_{0,film}$	318 K
$P_{0,film}$	.09 atm
M_{film}	0.5
u_{film}	280.4 m/s
Film throttle valve setting	15% (Partially open)
Film heater setting	7 (Medium-high)
T_{wall}	~335 K
$M_c = \frac{U_\infty - U_f}{a_\infty - a_f}$	0.53
$\lambda = \frac{\rho_f U_f}{\rho_\infty U_\infty}$	0.2
$s = \frac{\rho_f}{\rho_\infty}$	0.45
$r = \frac{U_f}{U_\infty}$	2.22

Test Case 2 corresponds to a subsonic film of M=0.72. The higher injection velocity, which is pressure matched to the core flow, results in a larger film protection length and a more stable boundary layer.

6.5.2 Flow structures

Figure 41 is a Schlieren image showing flow structures near the louver exit in Case 2. As in Case 1, a shock originating downstream of the edge of the louver and

the interface between film and core flows are visible. Unlike in Case 1, a reattachment shock is not visible.

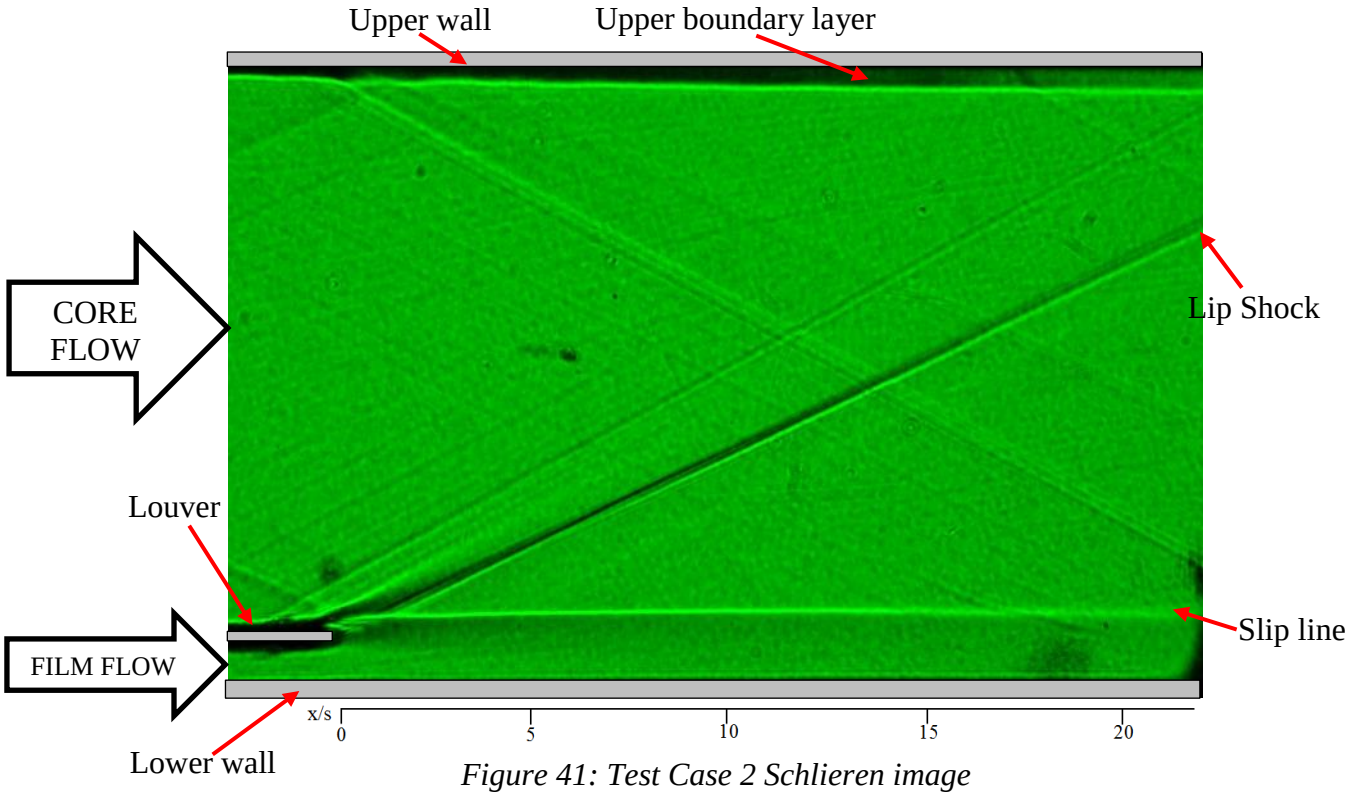

Figure 41: Test Case 2 Schlieren image

As in Case 1, the core is initially turned around the louver, creating a brief expansion on the upper edge of the louver. Now, however, the film flow from under the louver prevents the core flow from expanding into the film flow at all. The two flows continue parallel to each other while momentum transfer from the core flow accelerates the film. The slip line becomes fainter with distance downstream, indicating that the core and film flows are starting to mix. This suggests that the thermal protection offered by the film will decrease too and this will be borne out by the heat flux measurements presented in Figure 44.

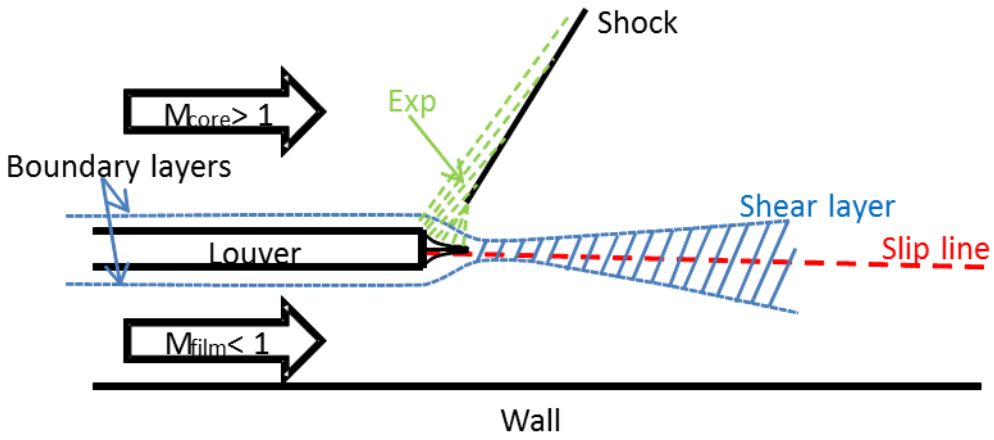

Figure 42: Supersonic flow-subsonic film at M=0.72 interaction

6.5.3 Upper Wall heat flux

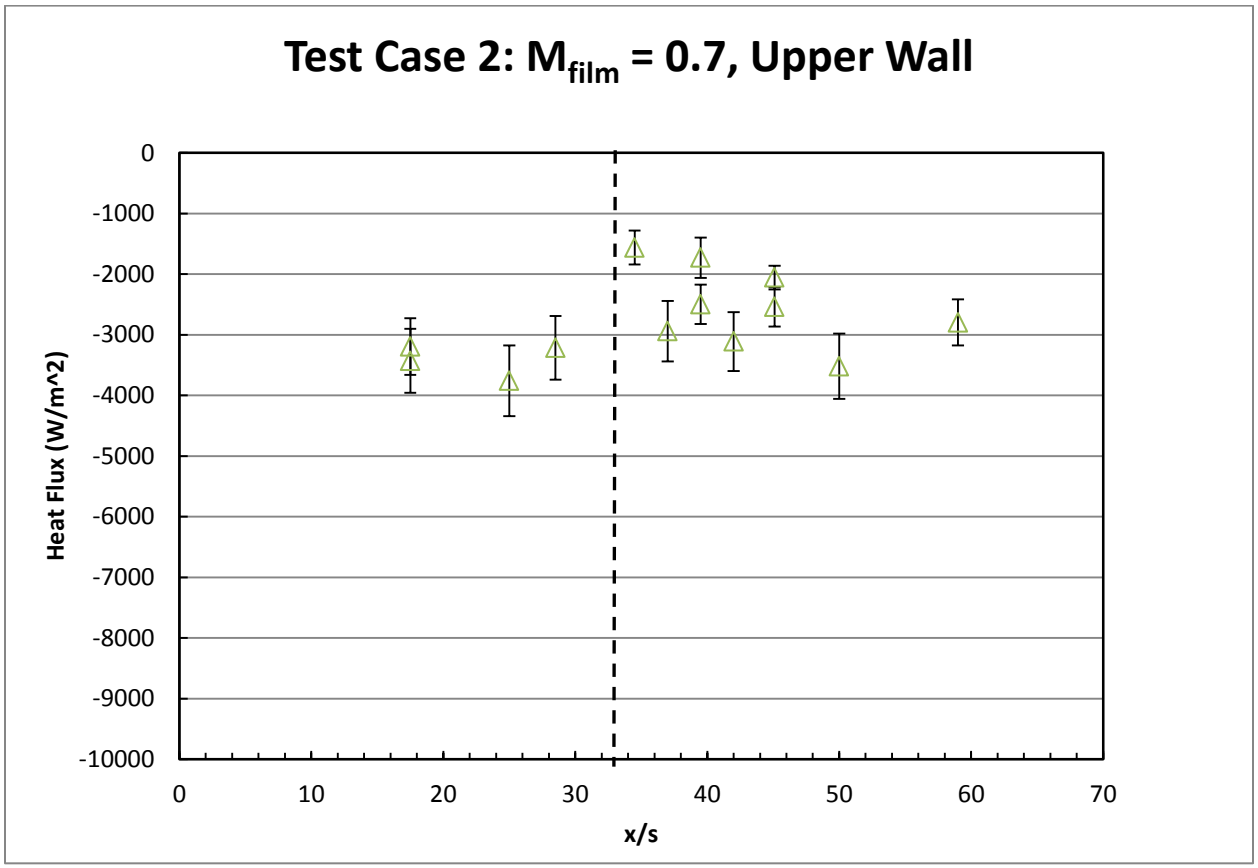

Figure 43: Test Case 2 upper wall heat flux. Dashed lines denote the locations of the lip shock impingement as determined by Schlieren (N = 15)

Figure 43 shows the heat flux distributions along the upper wall in Case 2. The decrease in heat flux in the ~32 < x/s < 45 range suggests this is where the expansion fan/shock system impact the upper wall. The change in heat flux is minimal because the static pressure of the film has been set to match that of the core and thus the fan/shock system is weak.

6.5.4 Lower Wall heat flux

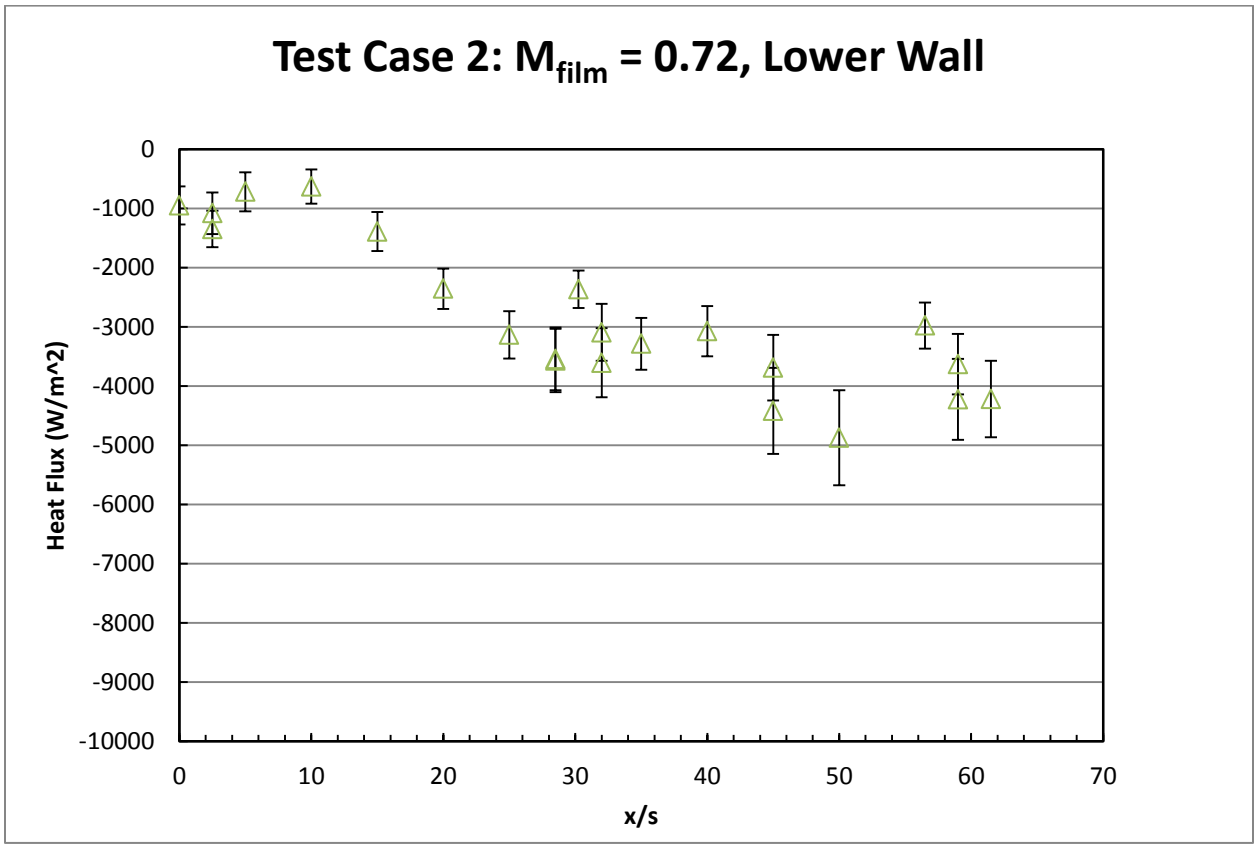

Figure 44: Test Case 2 lower wall heat flux (N = 15)

Figure 44 shows the heat flux distribution along the lower wall in Case 2. The core flow is now entirely prevented from contacting the lower wall, producing a longer region of film protection extending to x/s~15. Beyond this point, the shear layer begins to expand into the film flow, gradually degrading the thermal protection until it is fully mixed out at ~25 x/s. The heat flux increases relatively slowly after x/s ~ 25, indicating some lingering film protection.

6.6 Test Case 3

6.6.1 Summary of experimental conditions

Table 10: Test Case 3 Summary Table

$T_{0,ambient}$	295 K
$P_{0,ambient}$	1 atm
$T_{0,film}$	318 K
$P_{0,film}$	.21 atm
M_{film}	0.5
u_{film}	280.4 m/s
Film throttle valve setting	45% (Partially open)
Film heater setting	2x 10 (Two heaters at full power)
T_{wall}	~335 K
$M_c = \frac{U_\infty - U_f}{a_\infty - a_f}$	0.24
$\lambda = \frac{\rho_f U_f}{\rho_\infty U_\infty}$	0.44
$s = \frac{\rho_f}{\rho_\infty}$	0.57
$r = \frac{U_f}{U_\infty}$	1.30

Case 3 corresponds to a supersonic film of M=1.2. The supersonic injection results in an even larger film protection length and a more stable boundary layer in spite of more complex shock interactions between the film and core streams.

6.6.2 Flow structures

Figure 45 is a Schlieren image showing flow structures near the louver exit in Case 3. The shock from the louver end and interface between the core and film flow

are present as in the previous two cases. However now there is an additional shock propagating from the underside of the louver into the film layer.

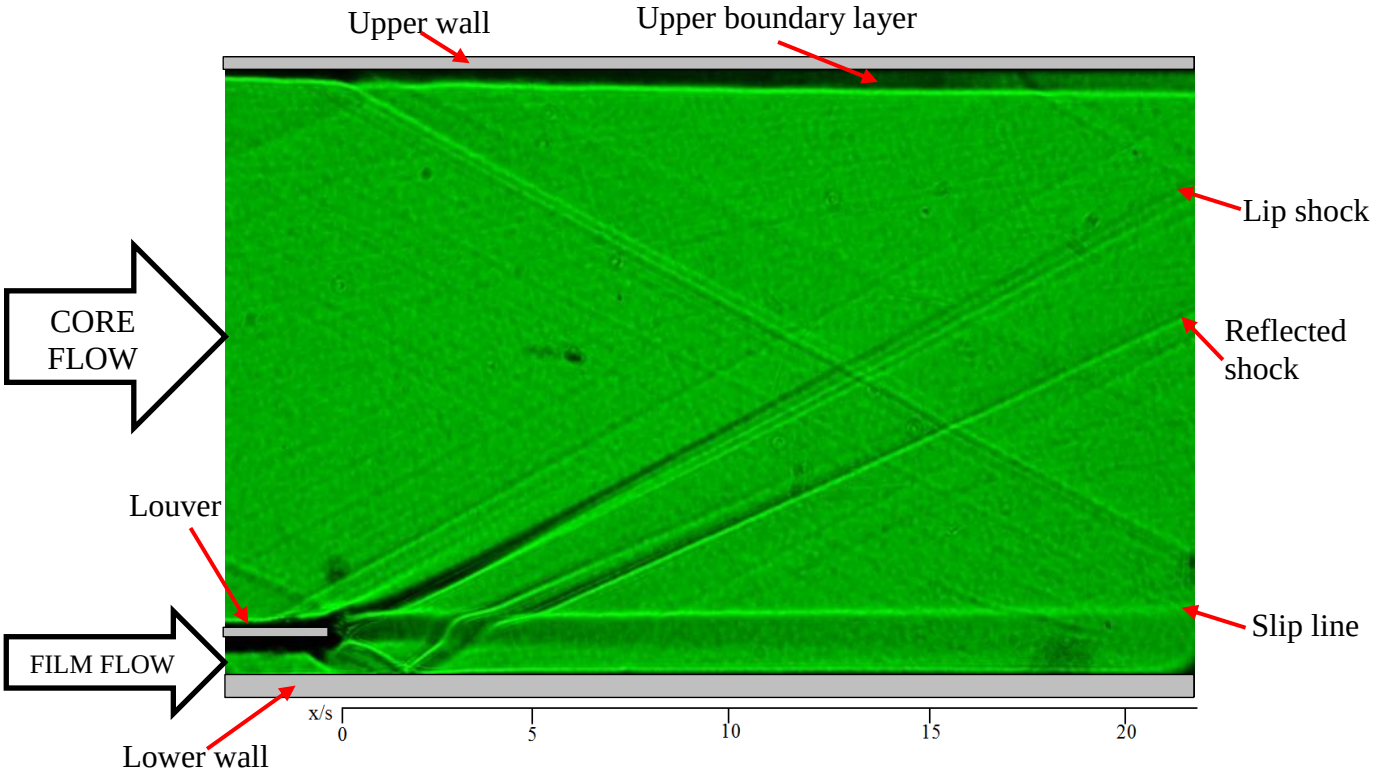

Figure 45: Test Case 3 Schlieren image

This shock reflects off the lower wall, is refracted as it passes through the shear layer (giving some indication of its thickness) and propagates back into the core flow. Meanwhile, the slip line continues parallel to the lower wall and diminishes little in intensity suggesting that mixing between the film and core is weak and thus that the thermal protection is relatively strong. This will be confirmed in Figure 48.

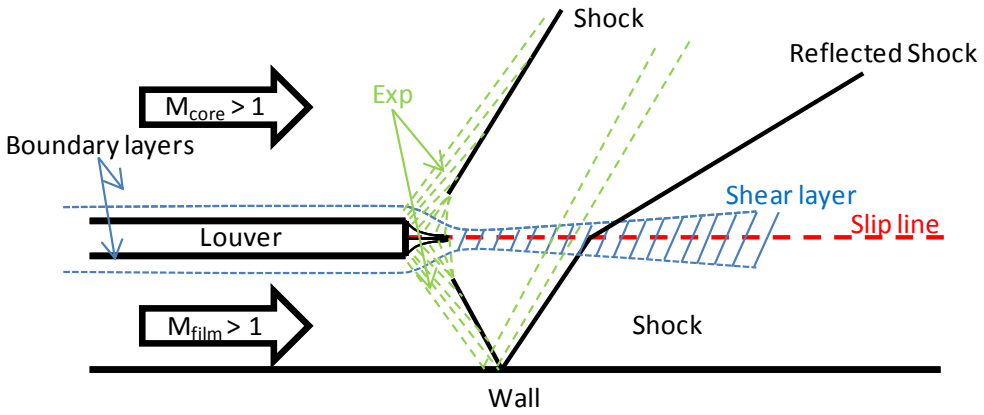

Figure 46: Supersonic flow-supersonic film interaction at film M = 1.2

6.6.3 Upper Wall heat flux

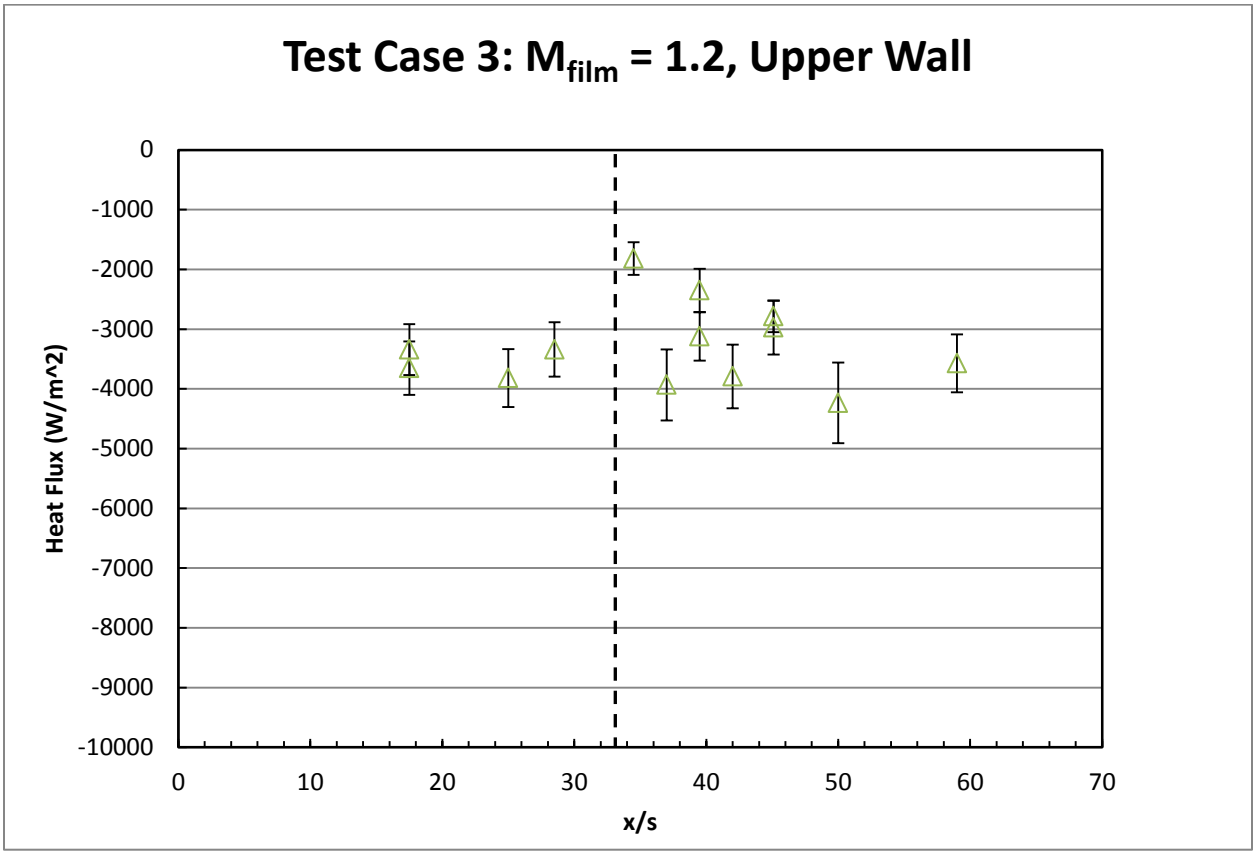

Figure 47: Test Case 3 upper wall heat flux. Dashed lines denote the locations of the lip shock impingement as determined by Schlieren (N = 14)

Figure 47 shows the heat flux distribution along the upper wall in Case 3. The decrease in heat flux in the ~30 < x/s < 37 range suggests that this is where the expansion fan/shock system contacts the upper wall. The change in heat flux is greater than in Case 2 (pressure matched) because the disturbance caused by the supersonic injection is larger.

6.6.4 Lower Wall heat flux

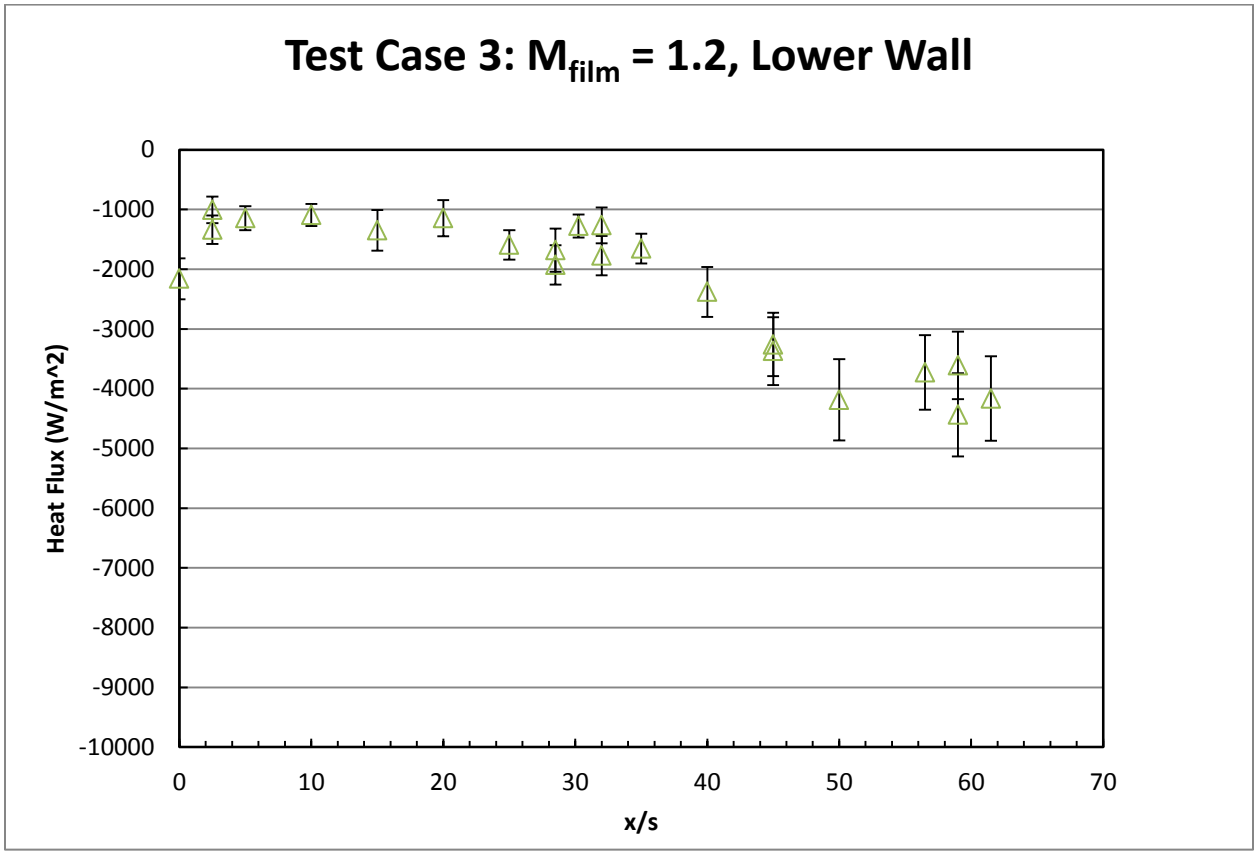

Figure 48: Test Case 3 lower wall heat flux (N =14)

Figure 48 shows the heat flux distribution along the lower wall in Case 3. The large protection region extending to x/s~35 is evident. The data show that the shear

layer starts to degrade beyond this point and film protection slowly erodes until the flow becomes fully mixed out around x/s~48.

6.6.5 Improved lower wall heat flux measurements

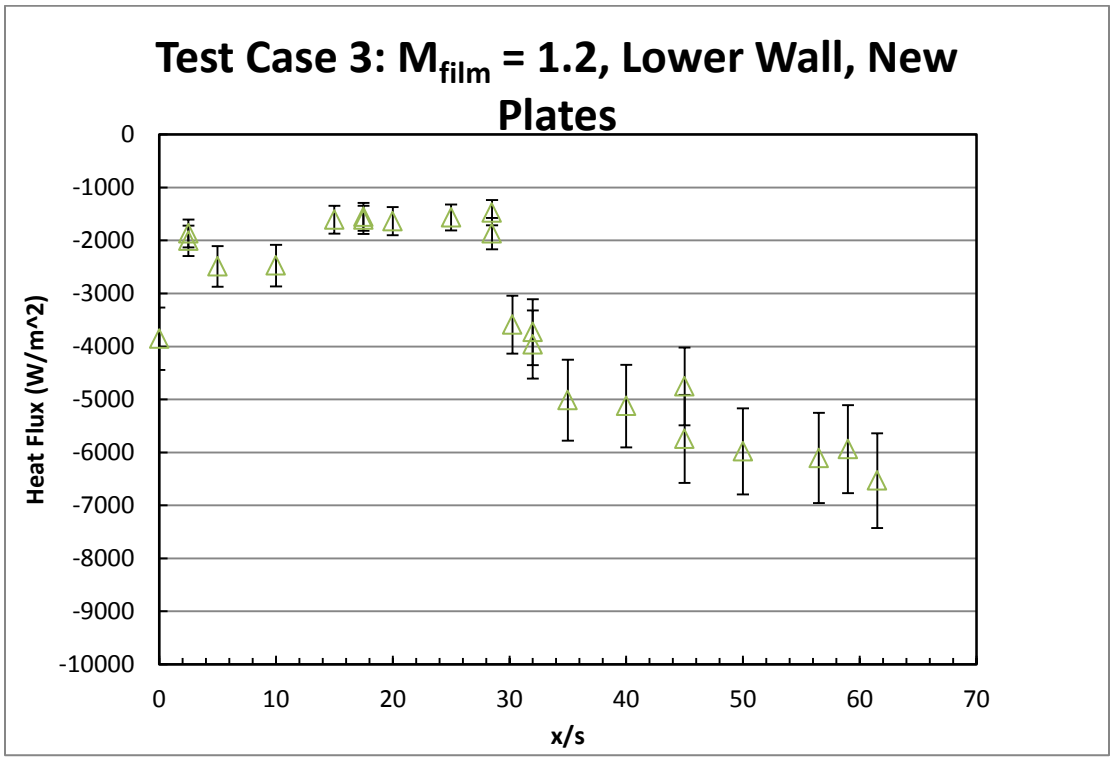

Figure 49: Test Case 3 lower wall heat flux with new instrument (N = 14)

Figure 49 shows a similar trend as Figure 48 but with some notable differences. First, the heat fluxes recorded in the $5 < x/s < 10$ region are higher than previous measurements. Second, the film breaks down sooner (at x/s~30 vs. x/s~ 35 previously) and more sharply than in Figure 48. Third, the heat flux downstream rises to 6000 W/m^2 rather than 4000 W/m^2. The reasons for this difference are unclear but one contributor could be the fact that the core Mach number in the new Case 3 measurements was 2.32 which is somewhat higher than the 2.25 in the previous set of

experiments. This likely led to a greater rate of shear between the two streams thereby causing the film to dissipate faster.

6.7 Comparison between measurements and CFD

6.7.1 Test Case 0

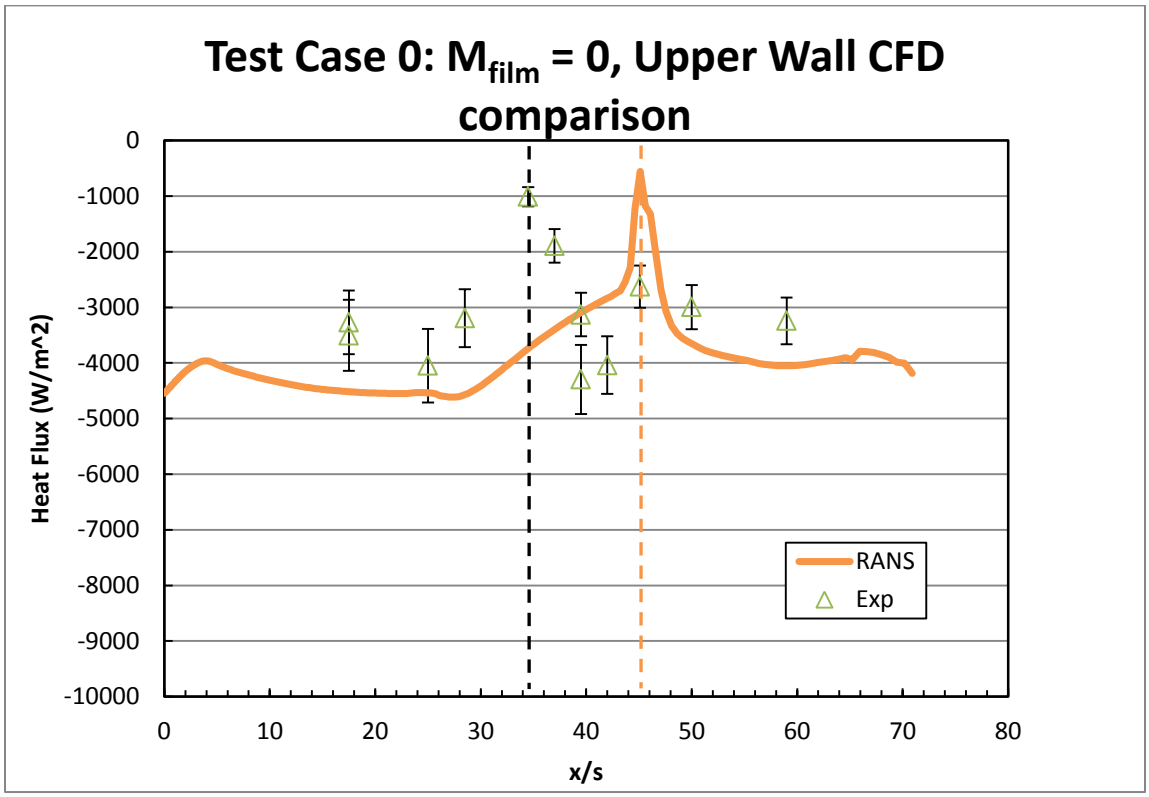

Figure 50: Test Case 0 upper wall heat flux comparison to RANS CFD. Dashed lines denote the locations of the lip shock impingement as determined by experimental (Schlieren, in black) and computational (RANS CFD, in orange) methods.

Figure 50 shows the comparison between Kittur's Loci-CHEM RANS simulation and the upper wall experimental data for Test Case 0. The RANS CFD slightly overpredicts the magnitude of the heat flux, but misses the impingement location of the recompression shock by about 10 x/s. The difference in impingement

point location between the measurements and simulations is caused by the fact that the angle of the recompression shock is smaller in the simulations than in the experiments. Kittur conducted an investigation into this discrepancy, but was not able to provide a resolution. Both the measurements and CFD indicate that the wall heat flux is reduced at the points where shock and expansion waves reflect off of the wall.

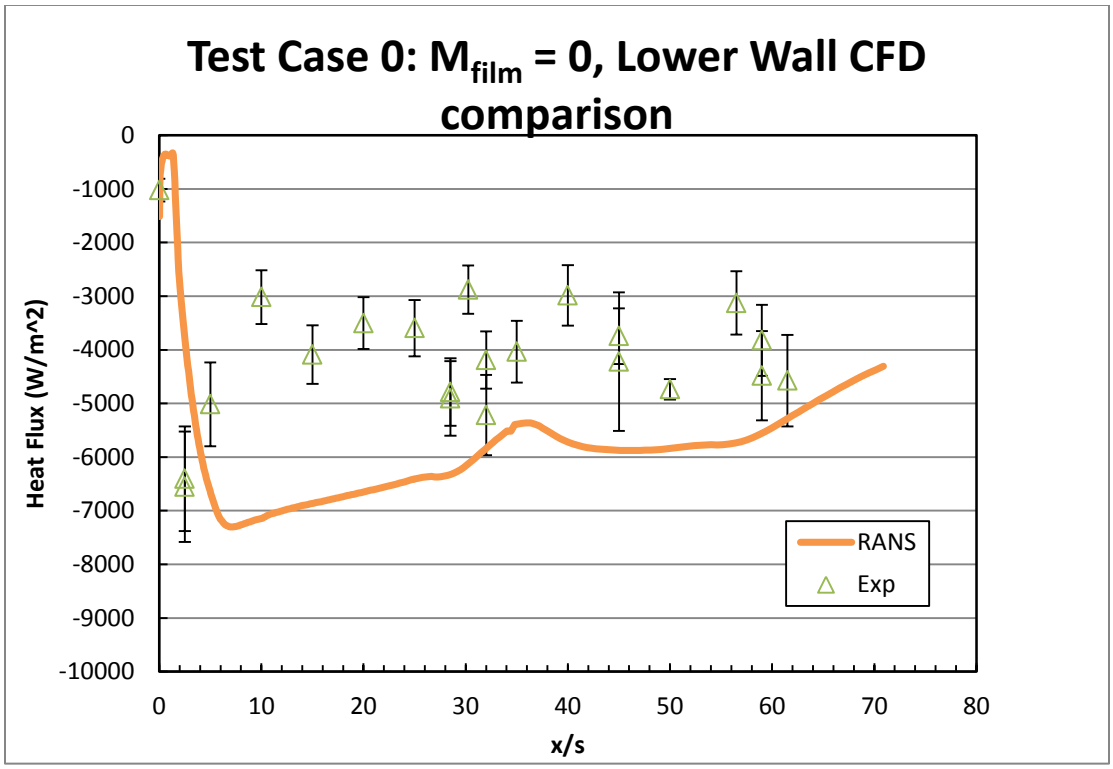

Figure 51: Test Case 0 lower wall heat flux comparison to RANS

Figure 51 shows the Test Case 0 lower wall heat flux compared to RANS CFD. RANS CFD overpredicts the heat flux everywhere except near the louver where it seems to underpredict it. Previous work [16], [23] suggests that this is caused by underpredicting the shear layer growth rate and/or the degree of mixing and momentum transfer between the core and recirculating flows. The 'bump' in the heat flux at x/s ~ 36 corresponds to the point at which the expansion fan from the upper

surface of the nozzle intersects the lower wall. A similar 'bump' is not visible in the measurements because of a high degree of scatter.

6.7.2 Test Case 1

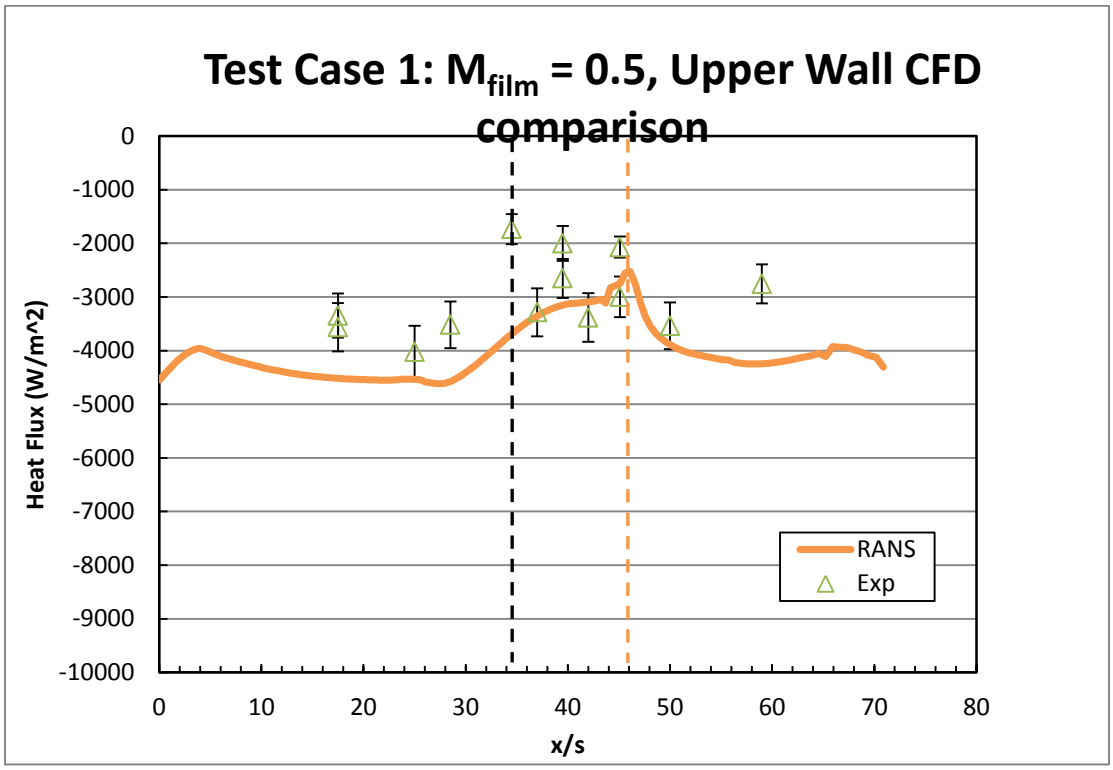

Figure 52: Test Case 1 upper wall heat flux comparison to RANS CFD. Dashed lines denote the locations of the lip shock impingement as determined by experimental (Schlieren, in black) and computational (RANS CFD, in orange) methods.

Figure 52 shows the Test Case 1 upper wall heat flux as compared to RANS CFD. The experimental prediction for the reattachment shock strikes the upper wall in the same general area at x/s~34 while RANS CFD predicts x/s~44. Thus, the discrepancy between the experiment and CFD-predicted shock location prediction remains, but the change in heat flux is much smaller because the reattachment shock is much weaker.

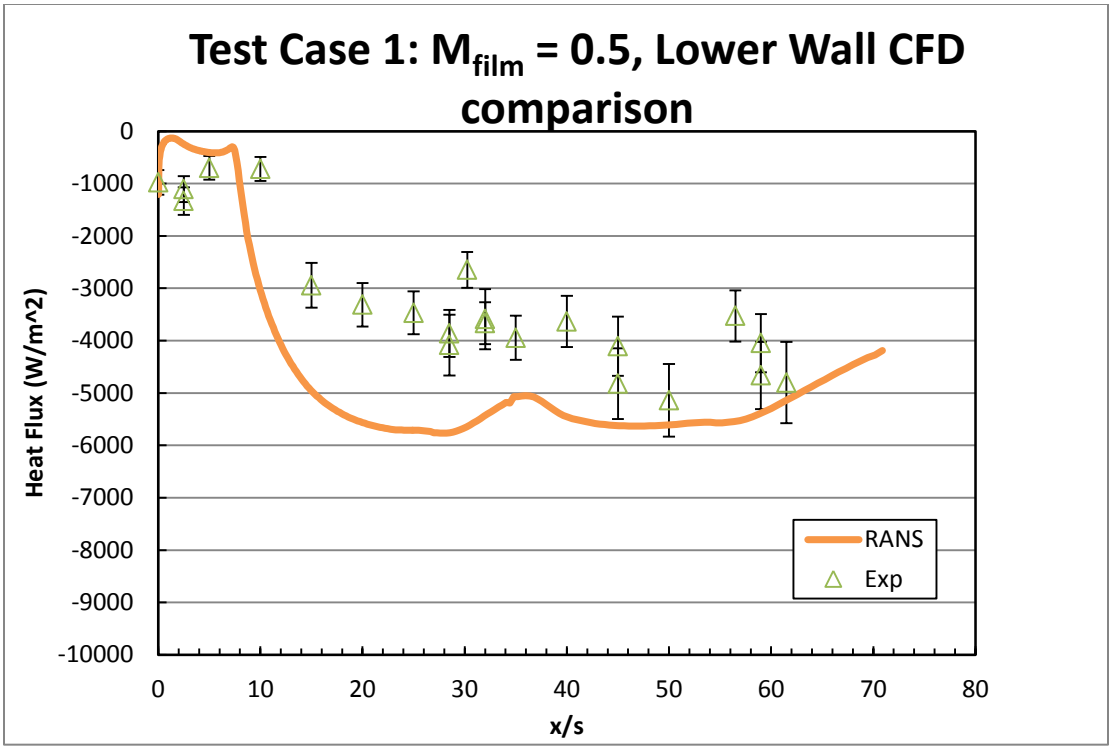

Figure 53: Test Case 1 lower wall heat flux comparison to RANS CFD

Figure 53 shows the heat flux measurements on the lower wall in Test Case 1 compared to RANS CFD. RANS CFD predicts film breakdown at x/s~8 which is somewhat earlier than observed experimentally. The RANS CFD underpredicts heat flux in the protected region but overpredicts almost everywhere else. As in Case 0, a 'bump' in the heat flux at x/s ~ 35 corresponds to the point where the expansion from the upper nozzle contacts the lower wall. It is interesting to note that the CFD seems to overpredict mixing/shear layer growth rate in Case 1 whereas it seems to underpredict it in Case 0.

6.7.3 Test Case 2

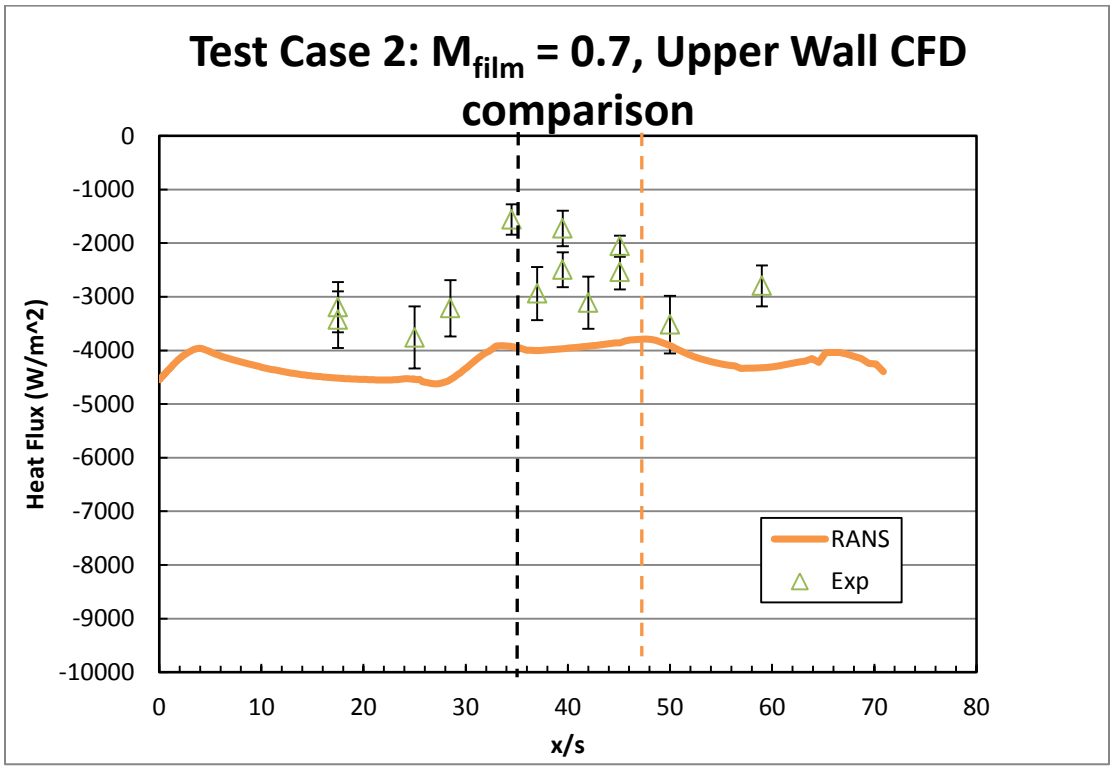

Figure 54: Test Case 2 upper wall heat flux comparison to RANS CFD. Dashed lines denote the locations of the lip shock impingement as determined by experimental (Schlieren, in black) and computational (RANS CFD, in orange) measurements.

Figure 54 shows the experimental comparison to RANS CFD for the upper wall in Test Case 2. The expansion strikes the upper wall at ~35 x/s, whereas RANS CFD seems to predict around 45 x/s.

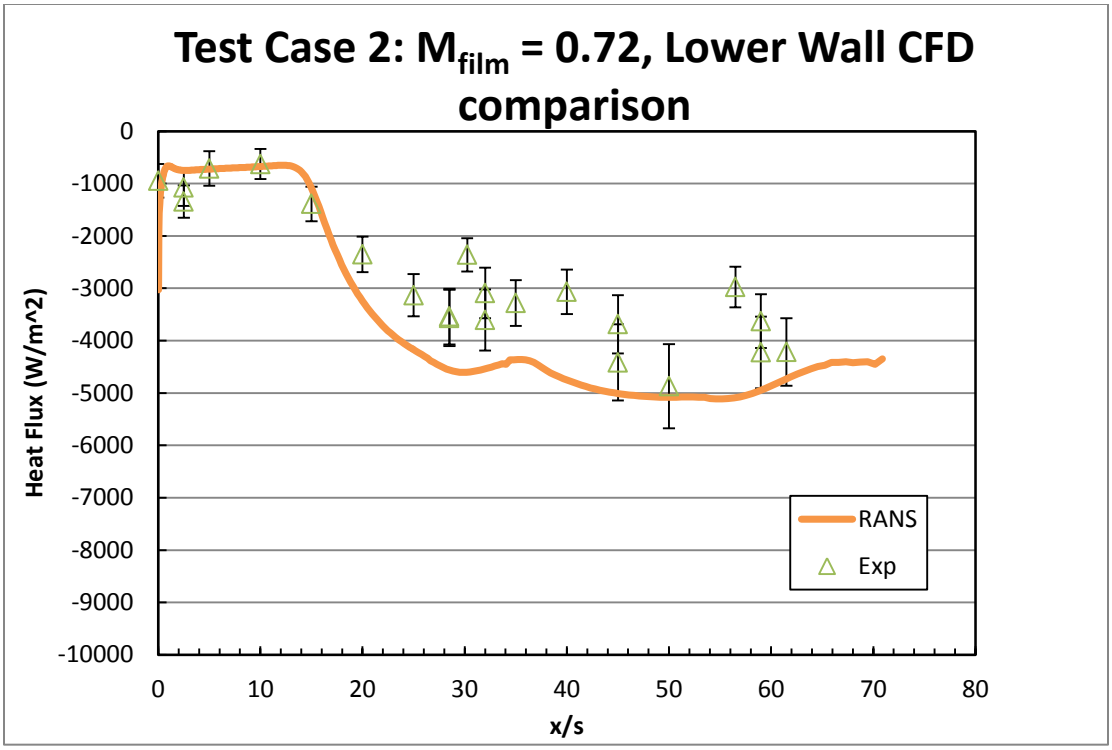

Figure 55: Test Case 2 lower wall heat flux comparison to RANS CFD

Figure 55 shows the comparison between experiments and RANS CFD for the lower wall in Test Case 2. RANS CFD predicts heat flux well in the protected region but overpredicts slightly after the film starts to degrade. The ‘’bump’ in the heat flux can be seen at ~35 x/.s where the expansion from the upper nozzle contacts the lower wall.

6.7.4 Test Case 3

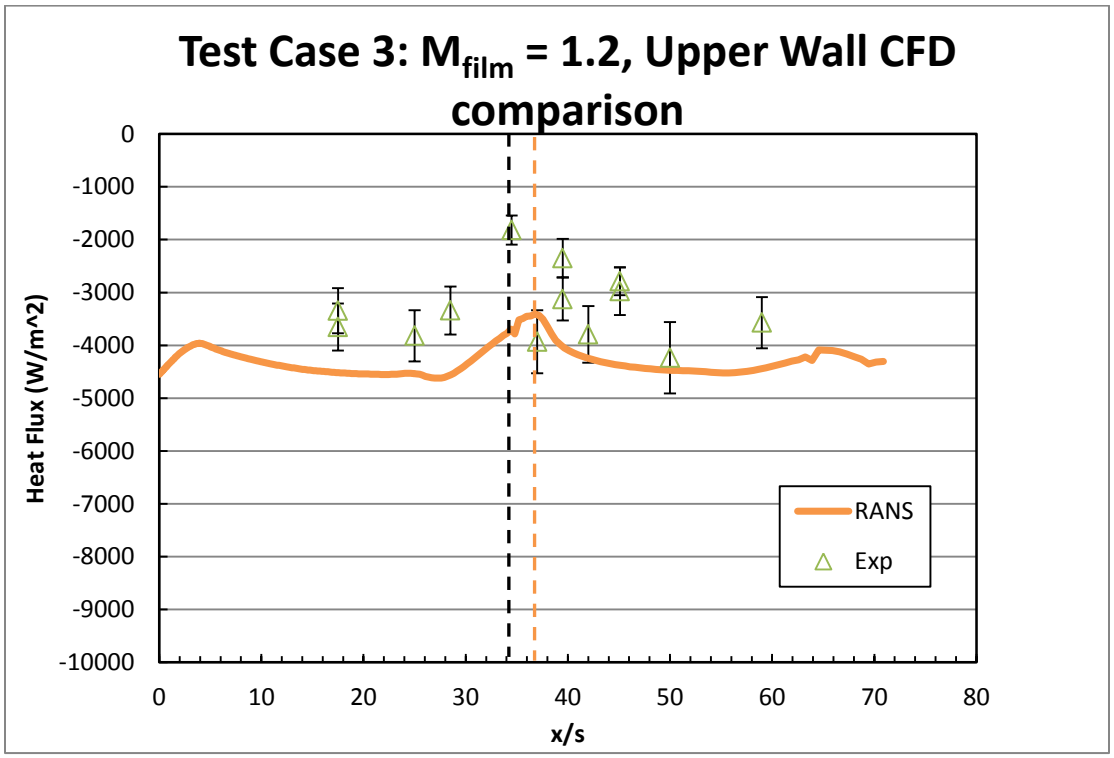

Figure 56: Test Case 3 upper wall heat flux comparison to RANS CFD. Dashed lines denote the locations of the lip shock impingement as determined by experimental (Schlieren, in black) and computational (RANS CFD, in orange) measurements.

Figure 56 shows the comparison between experimental measurements and RANS CFD predictions for the upper wall in Test Case 3. The RANS CFD heat flux magnitude prediction is similar to the previous three cases, but the location of the expansion is much closer in this case. The expansion strikes the wall at ~34 x/s, very close to the RANS CFD prediction of 36 x/s.

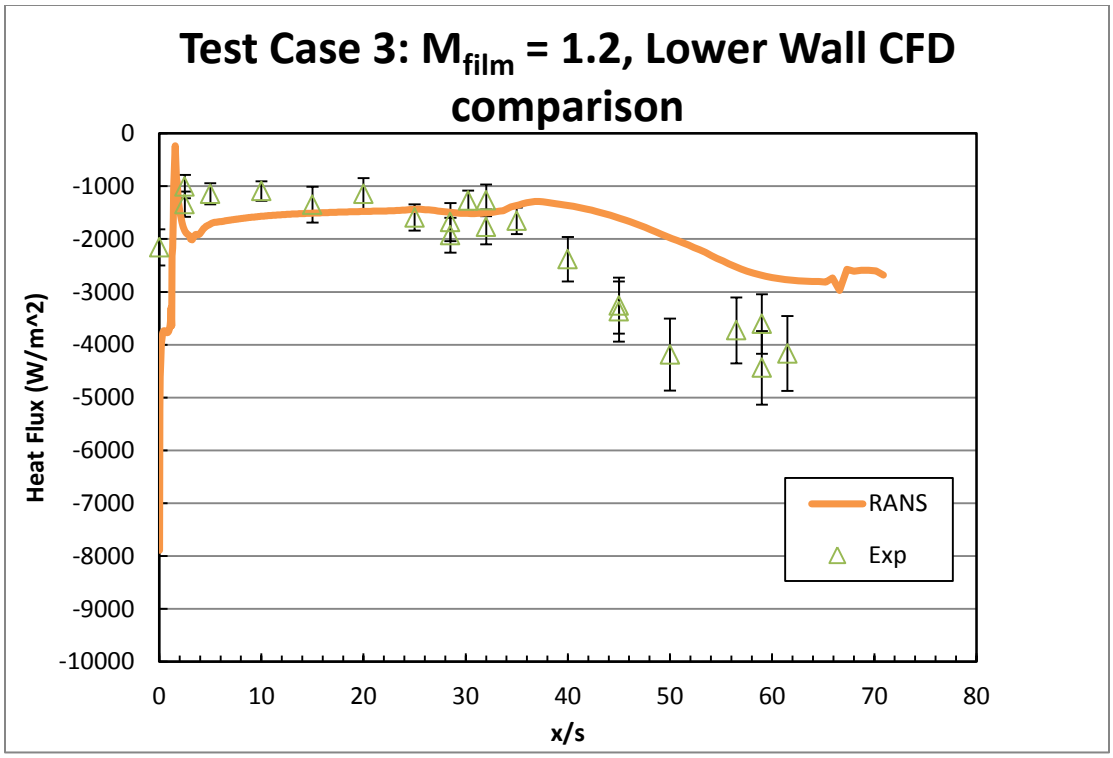

Figure 57: Test Case 3 lower wall heat flux comparison to RANS CFD

Figure 57 shows the comparison between the experimental heat flux and RANS CFD prediction on the lower wall in Test Case 3. RANS CFD underpredicts the heat flux in the protection region, but underestimates the degradation of the film, overpredicting the protection afforded by the film after it starts to break down. The expansion from the upper nozzle contacts the lower wall at the same location that the film breakdown begins, possibly causing difficulties in the simulation.

6.7.5 Experimental, RANS, and LES comparison

Figure 58 shows the comparison between the initial set of experiments and a separate set of RANS and LES simulations generated by Verma. In general, both RANS and LES simulations agree with the film cooling data within the protected region of the film. After the film protection wears off, the RANS simulations predict

a more drastic increase in the heat flux for the subsonic case. The LES simulation for Test Case 0 is still not converged, resulting in some oscillations. However, LES model tends to agree more with the experimental measurements than the RANS model in the x/s > 40 region, after the film has broken down.

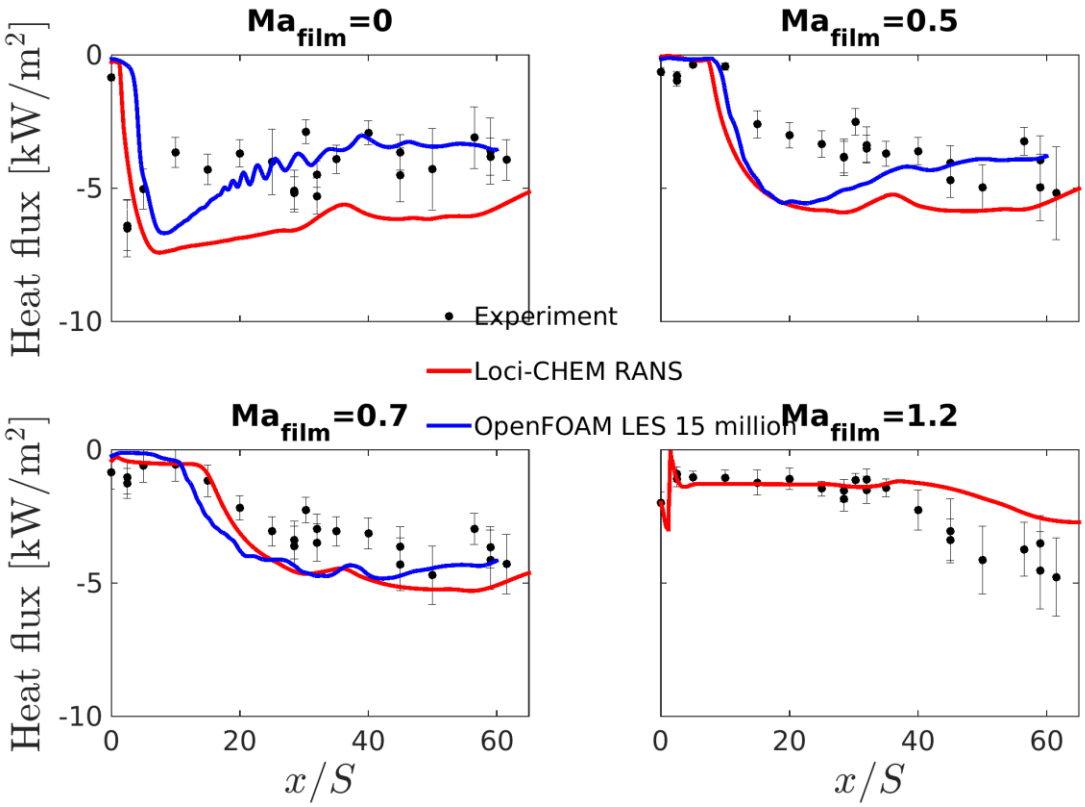

Figure 58: Experimental comparison to RANS and LES

The supersonic case, similar to past experiments, is the only case in which the CFD overpredicts the heat flux after film breakdown. LES simulations were not able to be conducted for the upper wall due to a lack of inflow condition.

Taken together, the RANS and LES simulations seem to predict trends in the experiments but are generally unable to predict the magnitudes of the wall heat flux within the uncertainty limits of the experiments. Thus, more work is required to

understand the factors influencing the differences between measured and predicted wall heat flux distributions.

Chapter 7: Verification of Heat Flux Measurement Technique

7.1 Overview

The relatively large variations in measured wall heat flux combined with persistent differences with CFD-based predictions motivated a parallel campaign to assess the efficacy of the methods used to measure wall heat flux. To this end, separate experiments were conducted with both upper and lower test plates in which both were impulsively exposed to a known thermal boundary condition (an ice bath at 0 C) and the measured subsurface temperature-time histories were used to predict the surface temperature. Experiments with both heated and unheated walls were performed. In the unheated cases, ΔT between wall and ice bath = 20°C and in the heated cases ΔT between wall and ice bath = 40°C.

Table 11: Full plate ice test summary table

$T_{ambient}$	295 K
T_{ice}	0 K
T_{wall}	318 K & 338 K

7.2 Temperature-time histories

Figure 59 shows the temperature time histories of all of the thermocouples in the upper wall instrument over the course of an experiment. The data show that some thermocouples respond in an inconsistent manner. Those are the thermocouples marked “Inactive” in Table 3 and assumed to have been damaged during installation. Data from these thermocouples are not processed or included in the final data sets. There is also a spread of initial thermocouple temperatures due to difficulty in heating the plates to perfect uniformly with several discrete heat sources (cartridge heaters.)

The initial temperature was examined with relation to the final heat flux, and has been determined to have a negligible effect on the final heat flux measurement.

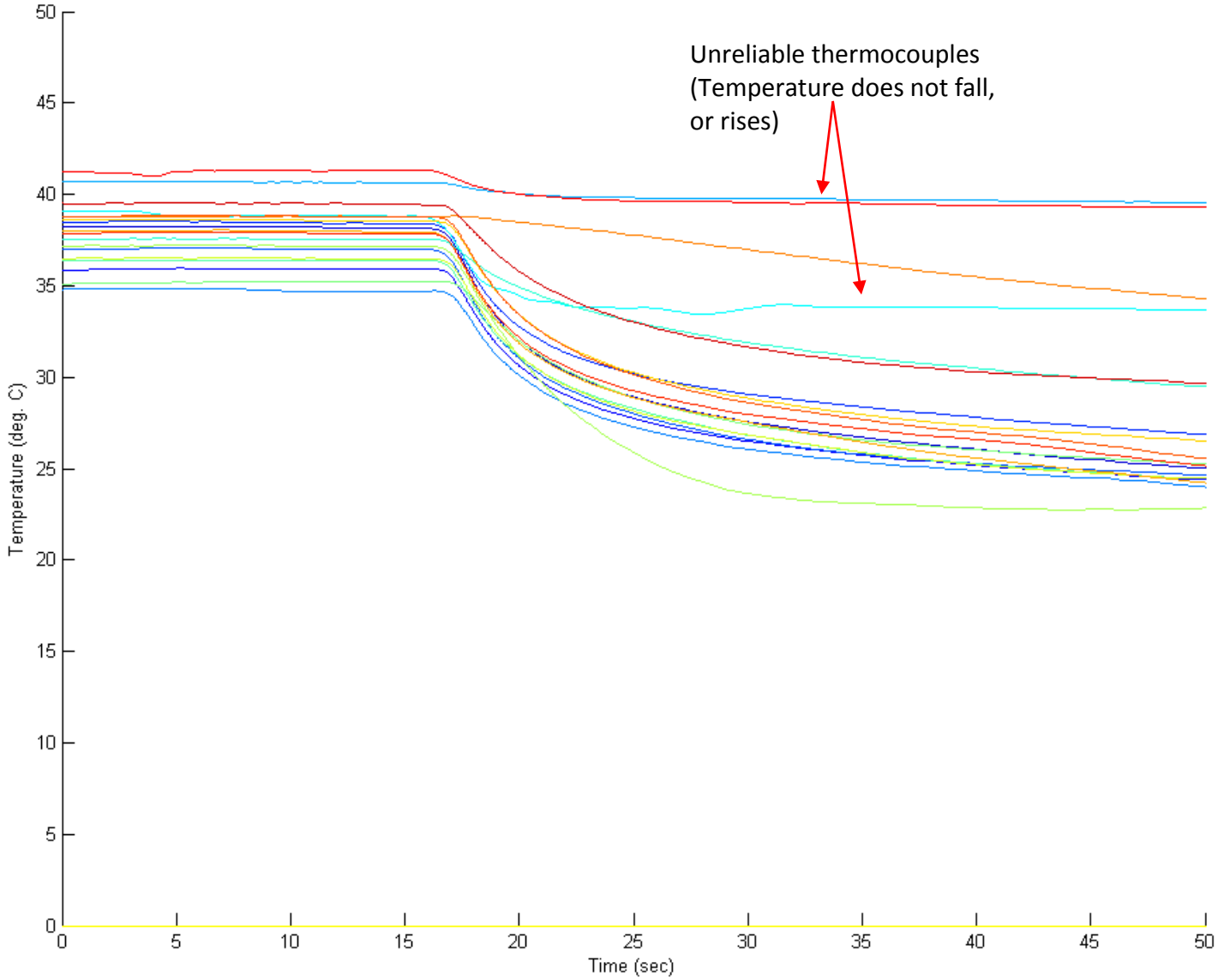

Figure 59: Sample Temperature-time histories for a full plate ice test. Each color shows the temporal response of a different thermocouple

7.3 Heat flux-time histories

The inverse heat flux method was used to process the above temperature time histories from when the plate contacted the water (at t=17 seconds) until the semi-infinite wall assumption was compromised (~10 seconds later when the thermal wave reaches the outer edge of the wall). The outcome is plotted as a function of time in Figure 60.

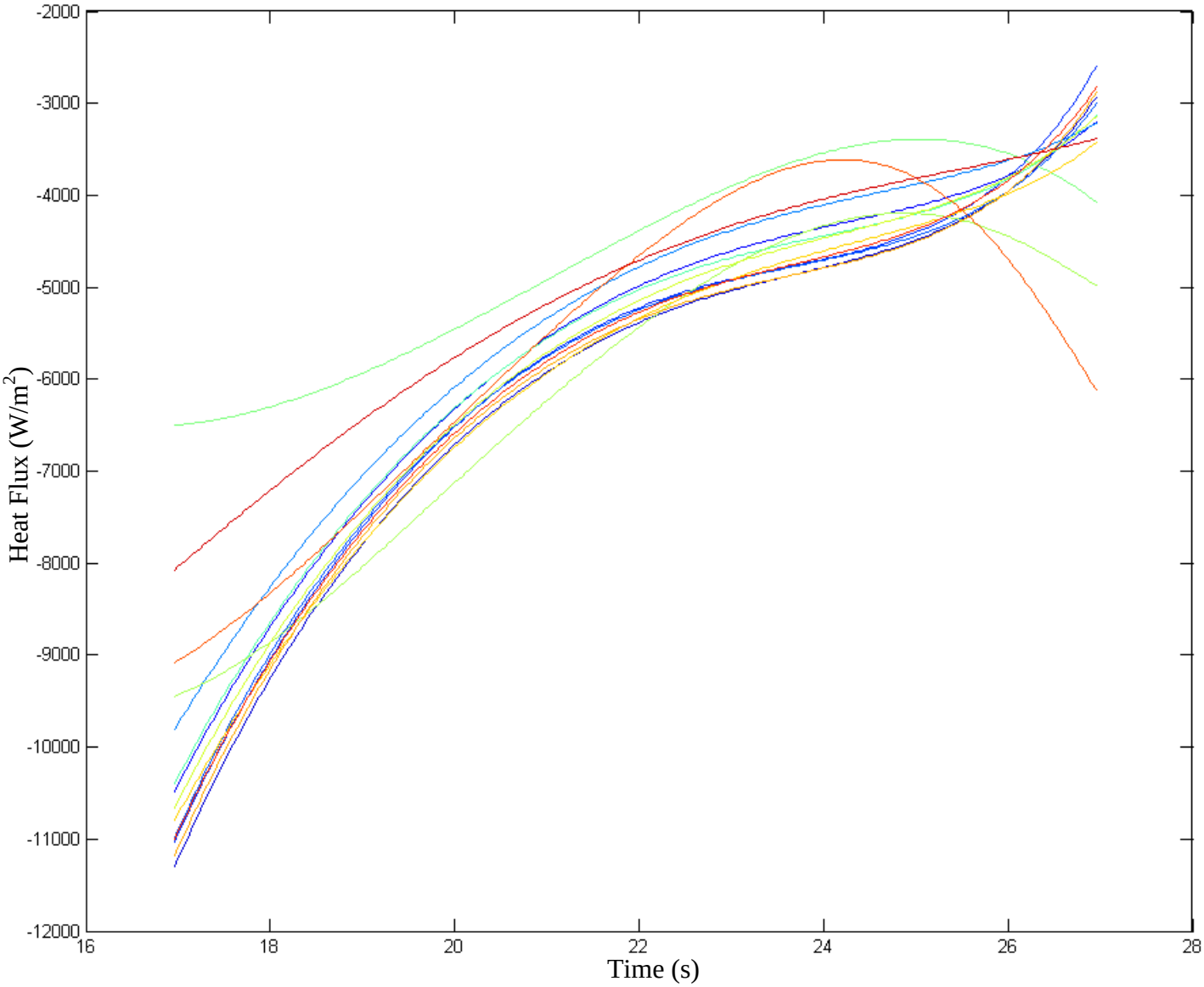

Figure 60: Sample Heat fluxes after curve fitting for full plate ice test. The plates were immersed in the ice bath at t=17 sec.

7.4 Effect of Scheme Used to Infer Heat Flux from Subsurface Temperature-Time Measurements.

As discussed in Section 3.3 Experimental Procedure, temperature-time histories were processed by both Maqbool's inverse curve fitting method and

Verma's simple 1D conduction solver. The results of the comparison are seen in Figure 61.

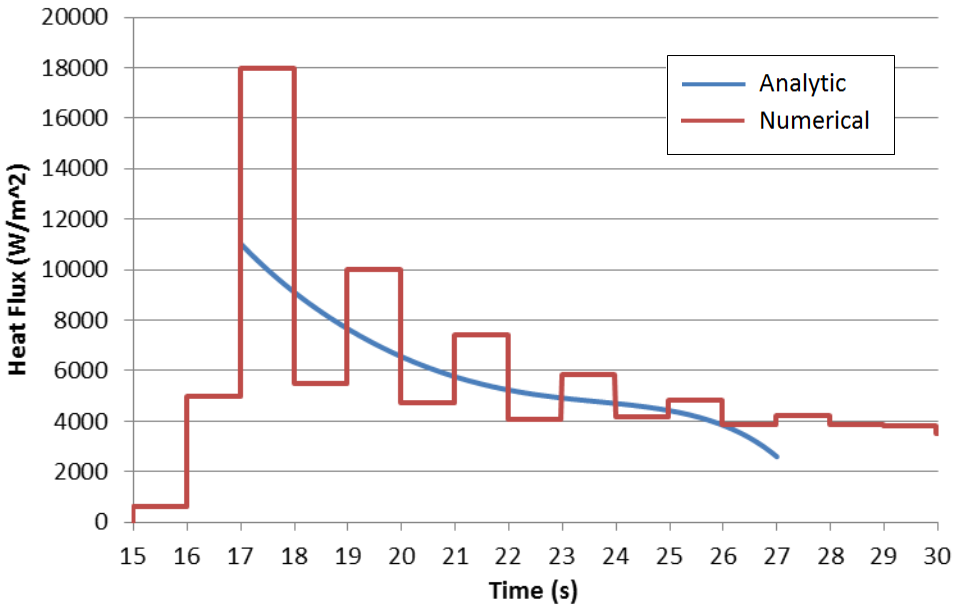

Figure 61: Comparison of the curve fitting and simple 1-D iterative approach to inferring heat flux from a subsurface temperature-time history.

It is clear that both codes follow the transient nature of the heat flux solution, though the 1-D conduction equation solution oscillates around the actual value. This is because the 1-D conduction solution works by predicting a heat flux, then attempting to construct the temperature time history at some depth below the surface. The temperature-time signal inherently contains some variation due to noise, even after smoothing, which is reflected in the oscillation of the heat flux solution.

As discussed in Section 3.3 Experimental Procedure, the test data presented in Chapter 6: Experimental Results: Film cooling were processed by both Maqbool's inverse curve fitting solution and Verma's simple 1-D unsteady convection solver to provide verification. The results are presented in Figure 62 - Figure 65. Finally, it

should be pointed out that Verma's method does not take into account the initial temperature gradient in the plate. Therefore, the main point is that both methods predict the same trends and the heat fluxes are generally of the same order of magnitude.

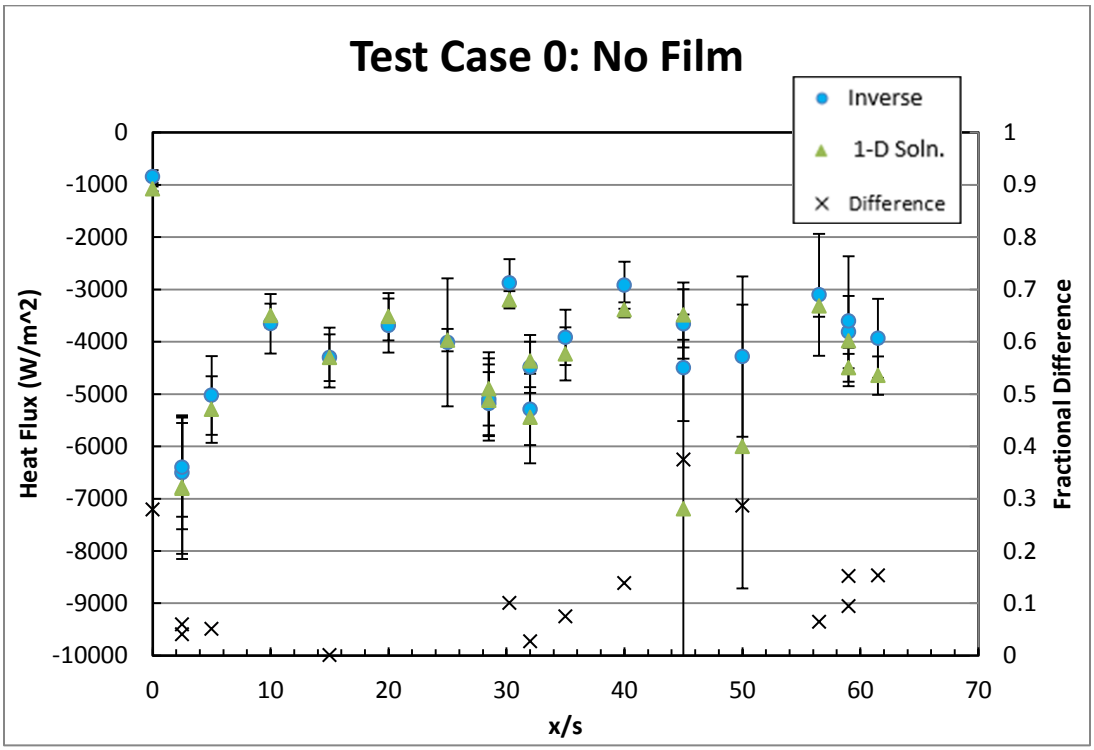

Figure 62: Curve fitting and simple 1-D iterative solution comparison – Test Case 0

For Test Case 0, the agreement between the two solutions is well within their respective margins of error. Both solutions capture the initial heat flux spike present due to the core flow turning around the louver, then settle to around 4000 W/m² with some scatter for the remainder of the test section. Verma's conduction solver has some difficulty with the heat flux gauges at 45 and 50 x/s as seen by the large variance and skewed average, so those values can be considered outliers. In general, the heat fluxes predicted using each technique are within 15% of each other and, more importantly, indistinguishable within their respective limits of uncertainty.

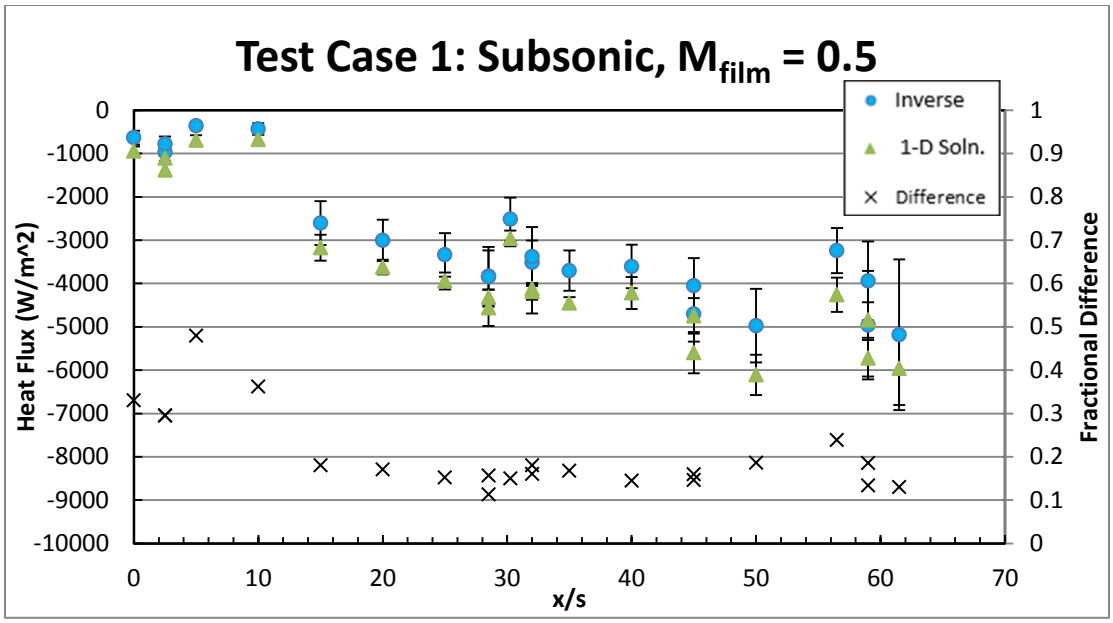

Figure 63: Curve fitting and simple 1-D iterative solution comparison – Test Case 1

For Test Case 1, the agreement between the two solutions is again generally within their respective margins of error. Both solutions show the initial film protection present in the first 10 x/s and capture the abrupt rise in heat flux at x/s = 15. While the agreement is not quite as good as Test Case 0, the values agree within 20% of each other over most of the domain. The percent disagreement between the methods is much higher in the film protected region immediately downstream of the louver. This is due to the fact that the wall heat flux in the protected area is very low and is an important factor to consider when designing practical systems.

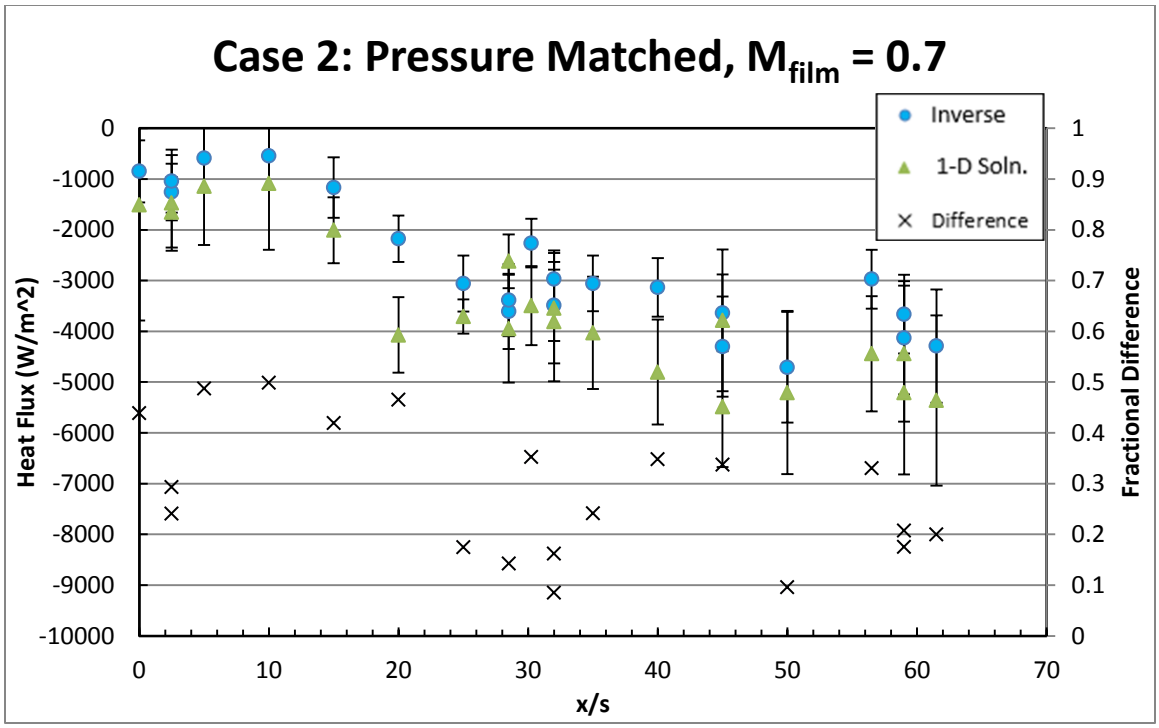

Figure 64: Curve fitting and simple 1-D iterative solution comparison – Test Case 2

Test Case 2 shows the poorest agreement between the two methods of data interpretation, and the reasons for the disagreement are unclear. Both solutions show the initial film protection present up to about 20 x/s, then the slow rise for the rest of the test section. However, Verma's conduction solution produces values ~30-40% higher than the curve fitting code. While the overall difference exceeds 30% in many areas, the predictions of both methods remain indistinguishable within their respective uncertainties. Therefore, the main source of the discrepancy between the two methods may be the relatively large uncertainties in Case 2.

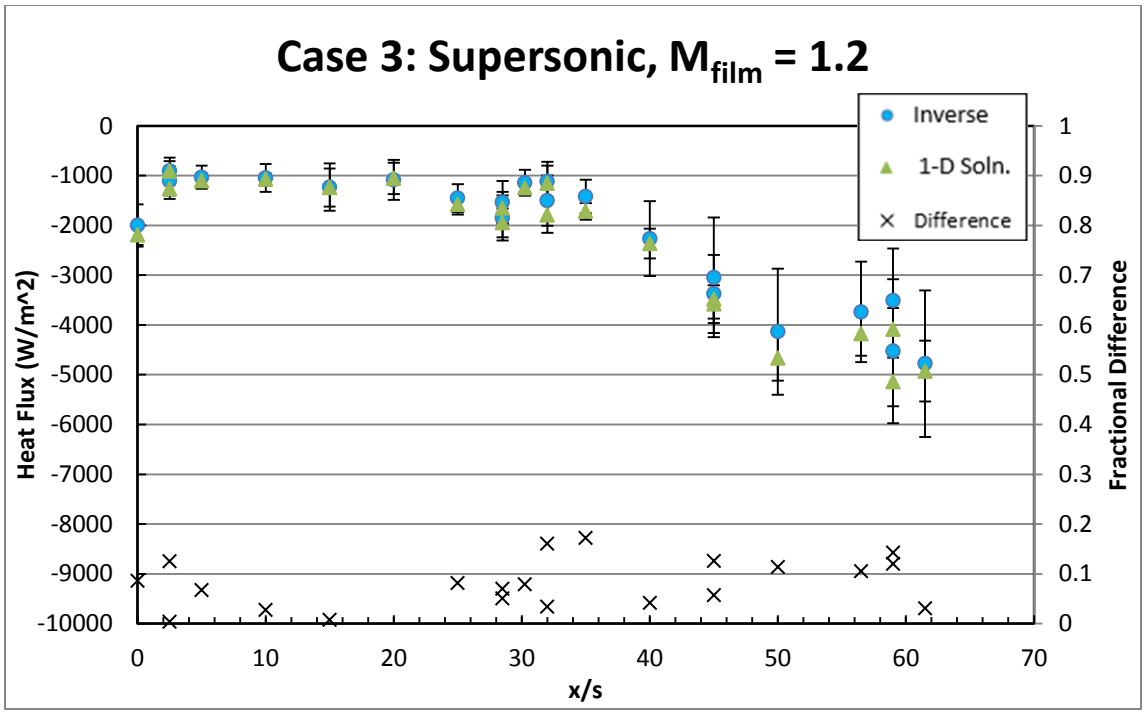

Figure 65: Curve fitting and simple 1-D iterative solution comparison – Test Case 3

The data interpretation methods are most consistent in Test Case 3. Both solutions show the enhanced supersonic film protection out to ~35 x/s, and capture the subsequent rise as the film layer breaks down. Again, low heat flux makes the difference slightly larger, but the two solutions generally agree to within 10-15%. As suggested in the discussion of the Case 2 results, this may be due to the fact that the overall measurement uncertainties are lowest in Case 3

7.5 Summary

Overall, the full wall instrument tests allowed the inverse measurement technique to be more closely examined for a known boundary condition. The comparison to Verma's data interpretation technique inspires confidence in the trends observed in the measured wall heat flux distributions. While differences in the

magnitudes of the heat flux predicted using the two methods can be significant (>20%), the differences usually don't exceed the level of uncertainty in the measurements themselves (i.e. are indistinguishable within their respective uncertainty limits) and seem to scale with the level of uncertainty. Thus, while more work is required to understand these differences, the heat flux measurement technique appears to be sound.

Chapter 8: Design of Favorable Pressure Gradient test section

8.1 Favorable Pressure Gradient background

A favorable pressure gradient refers to a situation where a flow's pressure decreases as it moves downstream:

$$\frac{dP}{dx} < 0 \tag{18}$$

Favorable pressure gradients are found in multiple physical situations, including the backsides of airfoils and in the expansion section of rocket nozzles. As discussed in Section 1.4 Previous work at UMD, work by Dellimore assimilated findings from over 40 investigations in the literature to show that favorable pressure gradients improve film cooling performance when the velocity of the film is greater than that of the core and degrade film cooling performance when the velocity of the film is smaller than that of the core. However, there are very few heat flux data acquired in situations where favorable pressure gradients are present let alone in conditions analogous to those present in the J-2X nozzle extension. Therefore, the objective of this section is to design a wind tunnel test section that can be sued to investigate the effect of pressure gradients in J-2X like conditions.

8.2 Design parameter selection

In order to begin the development of the favorable pressure gradient, it was necessary to select a targeted design parameter. One common parameter used by most studies [40][41][42] to quantify a pressure gradient is the acceleration parameter, or K [43]. Acceleration parameter can be defined as:

$$K = -\frac{\mu}{\rho^2 u_\infty^2}\frac{\partial p}{\partial x} \tag{20}$$

The parameter selected by Dellimore was Kay's acceleration parameter, or K_p [44]. Kay's acceleration parameter can be written as follows:

$$K_p = \frac{\nu}{U_\infty^2}\frac{dU_\infty}{dx} \tag{21}$$

Based on an analysis of the actual J-2X nozzle, Joseph Ruf of NASA Marshall Spaceflight Center provided some sample values for the kinematic viscosity, core velocity, and velocity change rate in the free stream. These values assume U_∞ and $\frac{dU_\infty}{dx}$ are selected outside of the boundary layer present along the wall of the nozzle, and produce a Kay's acceleration parameter of $K_p = 1.8 * 10^{-8}$. This corresponds to an acceleration parameter of approximately $K = 1 * 10^{-6}$, so the acceleration parameter produced would be in line with experiments from the literature. The current test section, with modification of a half angle nozzle and adjusted upper wall, is able to match this parameter by introducing an upper wall expansion angle of approximately 11.75°.

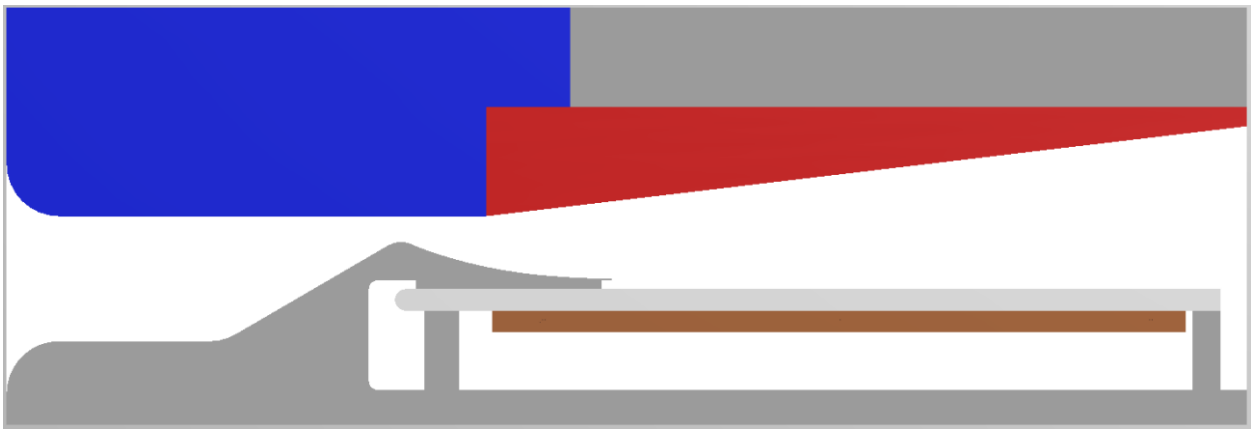

Figure 66: Favorable Pressure Gradient test section

It should be pointed out that making these modifications will make it difficult to impossible to measure heat flux on the upper wall, as the expansion removes the space needed to house the thermocouple modules and heating apparatus. However, this modification is acceptable, since the upper wall can no longer be considered an unprotected analogue of the lower wall.

Preliminary Favorable Pressure Gradient analysis

Some preliminary analyses of the performance of the favorable pressure gradient test section were conducted. The first was to determine the length of the expansion fan along the wall. Because the pressure gradient is generated by a single corner, the calculation of the Prandtl-Meyer expansion fan is fairly simple. The dimensions of the expansion fan can be seen below in Figure 67.

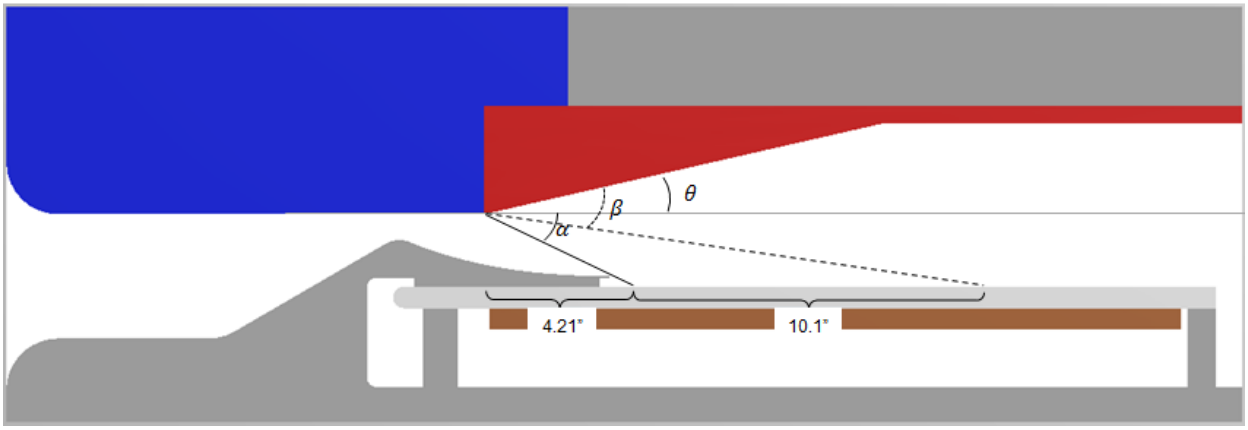

Figure 67: Favorable Pressure Gradient expansion length

In Figure 67, the expansion angle is denoted by θ measured from where the zero pressure gradient wall used to be. For $K_p = 1.8 * 10^{-8}$, this corresponds to θ = 11.75°. The first Mach wave of the expansion is shown as a solid black line and denoted by α, where $\alpha = 24.6°$. The final Mach wave of the expansion is shown as a

dashed black line and denoted by β, where $\beta = 19.9°$. This corresponds to a favorable pressure gradient length of 10.1", or 40.4 x/s, along the lower wall. In Test Cases 1 and 2 this extends past the film breakdown, but it roughly coincides with the Test Case 3 film breakdown. Therefore, some simulations were conducted in order to determine the predicted effects of the favorable pressure gradient on the heat flux. Figure 68 shows RANS simulations of Test Cases 0-3 for ZPG compared to FPG with an 11.75 degree expansion.

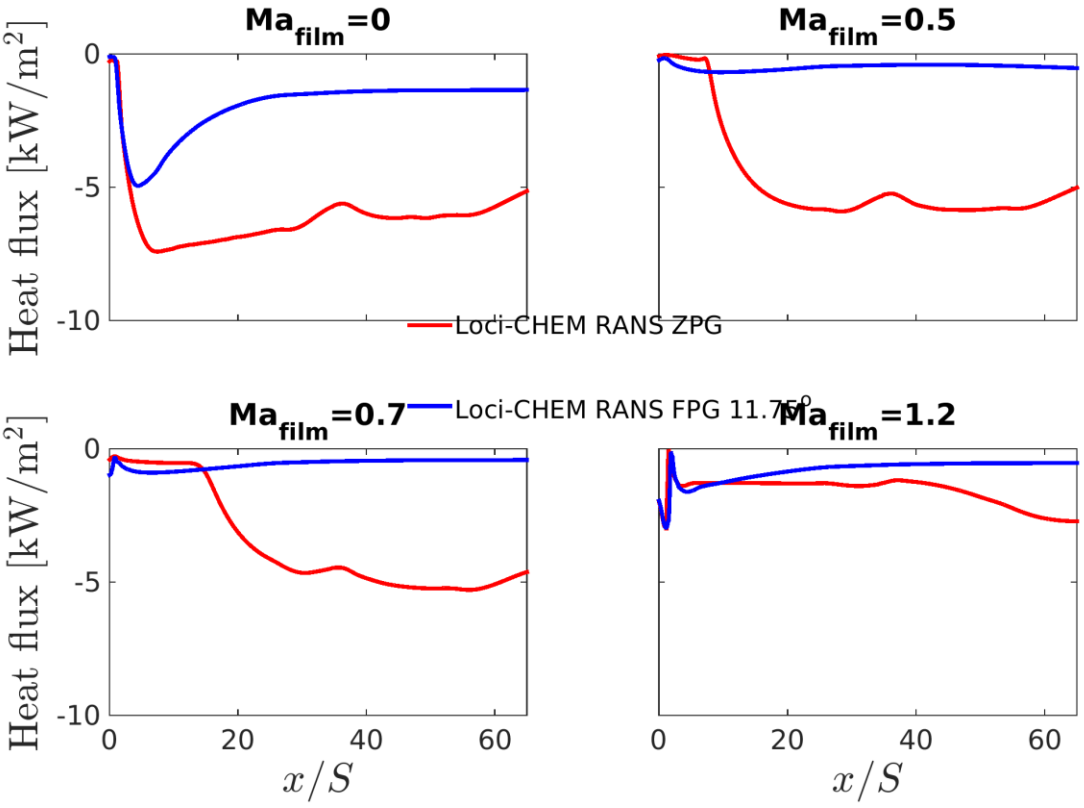

Figure 68: RANS heat flux simulations for Favorable Pressure Gradient (Verma).

Though there is some minor heat flux present in Test Case 3 and Test Case 0, the favorable pressure gradient generally has the effect of reducing the heat flux to the lower wall by such an amount that reliable measurements would be very difficult.

Therefore, in order to make quality measurements with the current apparatus, it might be necessary to further heat the lower wall and film. This would increase the magnitude of the heat flux occurring on the lower wall. Currently, the limitation on lower wall temperature is the operating temperature of the NI 9213 thermocouple modules. Once temperatures in the film plenum rise above 70°C, the modules start to return erroneous values, and must be restarted to resume testing. If a pass-through was constructed for the thermocouple wires, it would allow the thermocouple module to be mounted outside of the wall. With the sensitive electronics removed, the limiting temperature of the lower plates and film plenum would be the melting point of the plastic tubing, ~100°C.

Chapter 9: Conclusion

9.1 Summary of Findings

The main goal of this thesis is to provide a set of heat transfer measurements and Schlieren images for several film conditions in a supersonic flow that can be used to validate numerical solvers. The test matrix set out by Dellimore was populated with at least 15 experiments for each condition using the film cooling apparatus constructed by Maqbool. Additionally, the code developed by Maqbool for heat flux determination from subsurface temperature time histories was extended and verified with physical measurements.

The heat flux measurements on the lower wall are consistently lower than the RANS predictions in the subsonic cases, especially in the region around film breakdown. The RANS solver predicts the duration of the complete film protection very well, but predicts a much higher rise in the heat flux after film breakdown. In the supersonic case, the RANS under predicts the heat flux measurements, forecasting a longer film protection region than was measured. These results are similar to the data taken by Collett in 2014.

In order to take these heat flux measurements, several improvements were made to the film cooling assembly. The film heater from previous experiments was replaced with a superior version, resulting in more consistent and less transient film heating in all cases. Additionally, the test plates were reinforced to prevent failure in high stress regions. The Schlieren assembly was likewise improved by implementation of superior optics and more meticulous alignment procedures.

9.2 Main Contributions

1. Produced, installed, and collected data with a new set of nozzle blocks and test surfaces in the University of Maryland wind tunnel
2. Verified the inverse heat flux measurement technique developed by Maqbool with known boundary conditions and comparison to Verma's 1-D conduction solver
3. Collected at least 15 sets of heat transfer measurements, Schlieren images and pressure data for each test case suitable for comparison to RANS and LES

9.2 Future Work

While this work was sufficient to populate the test matrix for the zero pressure gradient case, the eventual goal of this project was to extend the research to a favorable pressure gradient. With that in mind, the following improvements can be made to collect data best suited to the development of film cooled rocket engines:

1. Implement a high speed focusing Schlieren imaging system in order to capture and quantify turbulence in the boundary and film layers.
2. Implement the favorable pressure gradient upper wall designed in Section 5.2 Favorable Pressure Gradient Design and record heat flux and pressure measurements. The upper wall has been designed to adjust the height discrepancy resulting from inaccurate CAD, producing a smooth expansion through the nozzle.
3. In the course of this work, several RANS and LES models were compared to the experimental data. Determining which model is most accurate for comparison

would provide a better understanding of where the models deviate from the measurements.

Appendices

A. *MATLAB Code – Adapted from Maqbool and modified*

For further explanation of this code or subroutines, please see reference [20].

```
clear
tic

% --------------------
% control panel starts

alpha = (7.3e-7);
%x = 0.001651;
x = 0.001397;
k = 1.46;

x1 =[ 0 0.625 0.625 1.25 2.5 3.75 4.375 4.375 5 6.25 7.125 7.125 7.5625 8 8 8.75 10
11.25 11.25 12.5 14.125 14.75 14.75 15.375];
x1 =x1'.*4;
x2 = [10 17.5 17.5 25 28.5 28.5 31.5 34.5 34.5 37 39.5 39.5 42 45.1 45.1 50 56 59 59
62 67.5]';

jmin=5;
jmax=18;
for ThermocoupleNumber = 0:45
   heat_flux_resultsSum(ThermocoupleNumber+2-1)= 0;
   surface_temp_resultsSum(ThermocoupleNumber+2-1)=0;
end
for j = jmin:jmax
   load(['temp_' num2str(j) '.lvm'])
   tempn = eval(['temp_' num2str(j)]);
%    load(['tempSmooth_' num2str(j) '.txt'])
%    tempn = eval(['tempSmooth_' num2str(j)]);

load(['pressureMod_' num2str(j) '.txt'])
pressn = eval(['pressureMod_' num2str(j)]);
pressn = pressn';
indexes = [];
t= pressn(:,1);
dt = pressn(2,1)-pressn(1,1);
for i = 1:length(t)
   if (pressn(i,4)<0.59)&&(pressn(i,4)>0.3)
     indexes = [indexes i];
   end
```

```
end
tstartold = min(indexes-1)*dt;
tendold = max(indexes-1)*dt;

runtime = tendold - tstartold;
tunnel_start_time = ceil(tstartold + runtime/8);
tunnel_end_time = ceil(tstartold + 7*runtime/8);

sample_rate_Hz = 1/(tempn(2,1)-tempn(1,1));

temp_gradient = 0.00;

   % control panel ends
   % ------------------

   for i =1:1:46
      ThermocoupleNumber = i-1;

         data_start_index = (tunnel_start_time)*sample_rate_Hz;
         data_end_index = (tunnel_end_time)*sample_rate_Hz;

         times = tempn((data_start_index:data_end_index),1);
         times2 = tempn((data_start_index:data_end_index),1);
         temps = tempn((data_start_index:data_end_index), ThermocoupleNumber+2);

         temps_for_T_init = tempn(((tunnel_start_time-
.5)*sample_rate_Hz:(tunnel_start_time)*sample_rate_Hz),
ThermocoupleNumber+2);

         T_init = mean(temps_for_T_init);


         tgc = 0;
         for tgc = 1:length(temps)
            temps(tgc) = temps(tgc) + (times(tgc)-tunnel_start_time)*temp_gradient;
         end

         %plot(times, temps)

         % Non-dimensionalize time, temperature, and distance
         nd_times = alpha.*times./(x^2);
         nd_temps = (temps - T_init)/T_init;

         % set number of terms

         n = 5;
```

```
        % precalculate coefficients of b

        for t_counter = 1:1:length(nd_times)
           for n_counter = 1:1:n
              inerf_terms(t_counter, n_counter) = inerf(2*n_counter,
0.5/sqrt(nd_times(t_counter)));
              pre_coeffs(t_counter, n_counter) =
((4*nd_times(t_counter))^n_counter)*gamma(n_counter+1)*inerf_terms(t_counter,
n_counter);
           end
        end

        toc

        options = optimset('fminsearch');
        options = optimset(options,'Display','iter');
        options = optimset(options,'MaxFunEvals',500000);
        options = optimset(options,'MaxIter',500000);
        options = optimset(options,'TolFun',1e-18);
        options = optimset(options,'TolX',1e-18);
        bs = fminsearch(@(bs) temperature_fmin_function(bs, pre_coeffs, nd_times,
nd_temps), -0.02.*zeros(1,n), options)

        % curve fit

        for cc = 1:length(nd_times)
           fit_temp = 0;
           for bb = 1:length(bs)
              fit_temp = fit_temp +
bs(bb)*(4*nd_times(cc))^bb*gamma(bb+1)*inerf_terms(cc, bb);
           end

           fit_temps(cc) = fit_temp;
        end

        toc

        for cc = 1:length(nd_times)
           fit_surface_temp = 0;
           for bb = 1:length(bs)
              fit_surface_temp = fit_surface_temp + bs(bb)*(nd_times(cc))^(bb);
           end

           fit_surface_temps(cc) = fit_surface_temp*T_init + T_init;
        end
```

```
        for cc = 1:length(nd_times)
            fit_q = 0;
            for bb = 1:length(bs)
                fit_q = fit_q + bs(bb)*(nd_times(cc))^(bb-
0.5)*gamma(bb+1)/gamma(bb+0.5);
            end

            %fit_qs(cc) = fit_q*k*T_init/(x);
            %fit_qs(cc) = fit_q*k*60/(x);
            fit_qs(cc) = fit_q*k*fit_surface_temps(cc)/(x);
        end

        heat_fluxes = (-fit_qs);
        surface_temps = fit_surface_temps;
        times = nd_times.*(x^2)./alpha;


        for w = 1:(length(heat_fluxes)-1)
            residual(w) = abs(heat_fluxes(w+1)-heat_fluxes(w));
            wstart = 1;
            wend = ceil(7*length(heat_fluxes)/8);
            wlen = wstart-wend;
        end
        heat_fluxes_plot = heat_fluxes;
        heat_flux_results(ThermocoupleNumber+2-1,j+1)=
sum(heat_fluxes(wstart:wend))/wlen;
        surface_temp_results(ThermocoupleNumber+2-1,j+1) =
sum(surface_temps(wstart:wend))/wlen;
        clearvars residual
        clearvars heat_fluxes
        clearvars times
        clearvars surface_temps
      end
   end
toc

for j=jmin:1:jmax
   heat_flux_resultsSum = heat_flux_results(:,j+1)+heat_flux_resultsSum;
   surface_temp_resultsSum =surface_temp_results(:,j+1)+surface_temp_resultsSum;
   Nruns = Nruns+1;
End

heatflux = nanmean(heat_flux_results');
surfacetemp = nanmean(surface_temp_results');
```

```
a = heat_flux_results';
e = nanstd(a);

figure()
errorbar(x1,heatflux([1:24]),e([1:24]),'bo')
ylabel('Surface Heat Flux (W/m^2)')
xlabel('x/s')
title('bottom')
axis([-2 70,-8000 0])

figure()
errorbar(x2([1:19]),heatflux([25:43]),e([25:43]),'bo')
ylabel('Surface Heat Flux (W/m^2)')
xlabel('x/s')
title('top')
axis([-2 70,-8000 0])
```

B. CFD boundary conditions

	C. Kittur (RANS)	**S. Verma (RANS)**	**S. Verma (LES)**
Core Inlet	isentropicInflow(p_0 = 101325 Pa, T_0 = 300 K)	isentropicInflow(p_0 = 101325 Pa, T_0 = 295 K)	Generated with RANS
Film Temperature	323 K	323 K	323 K
Wall Temperature	333 K	333 K	333 K
Outflow	Zero gradient for all variables	Zero gradient for all variables	Zero gradient for all variables
Case 0 BC	Wall	Wall	Wall
Case 1 BC	isentropicInflow(p_0 = 6500 Pa, T_0 = 323 K)	isentropicInflow(p_0 = 6500 Pa, T_0 = 323 K)	Generated with RANS
Case 2 BC	isentropicInflow(p_0 = 9100 Pa, T_0 = 323 K)	isentropicInflow(p_0 = 9100 Pa, T_0 = 323 K)	Generated with RANS
Case 3 BC	isentropicInflow(p_0 = 22000 Pa, T_0 = 323 K)	isentropicInflow(p_0 = 22000 Pa, T_0 = 323 K)	Generated with RANS
Upper wall y+	~0.3	~0.1	Upper wall not resolved in LES
Lower wall y+	~0.1	~0.1	2
Total Cells	200,000	100,000	15,000,000

C. *Infrared Heating Assurance*

Since the copper plates are heated with cartridge heaters, there are initially large thermal gradients in both the copper heating plates and MACOR test plates. While Maqbool's interrogation method accounts for a small initial thermal gradient present depthwise in the MACOR plate, it is necessary to have the plates be roughly isothermal in the spanwise and streamwise directions at the start of data collection. In order to ensure that the MACOR plates were uniformly heated, a FLIR Thermacam SC3000 thermal camera was used to record a video of the plates during a typical heating cycle. The copper and MACOR were painted black to ensure uniform emissivity between the two materials.

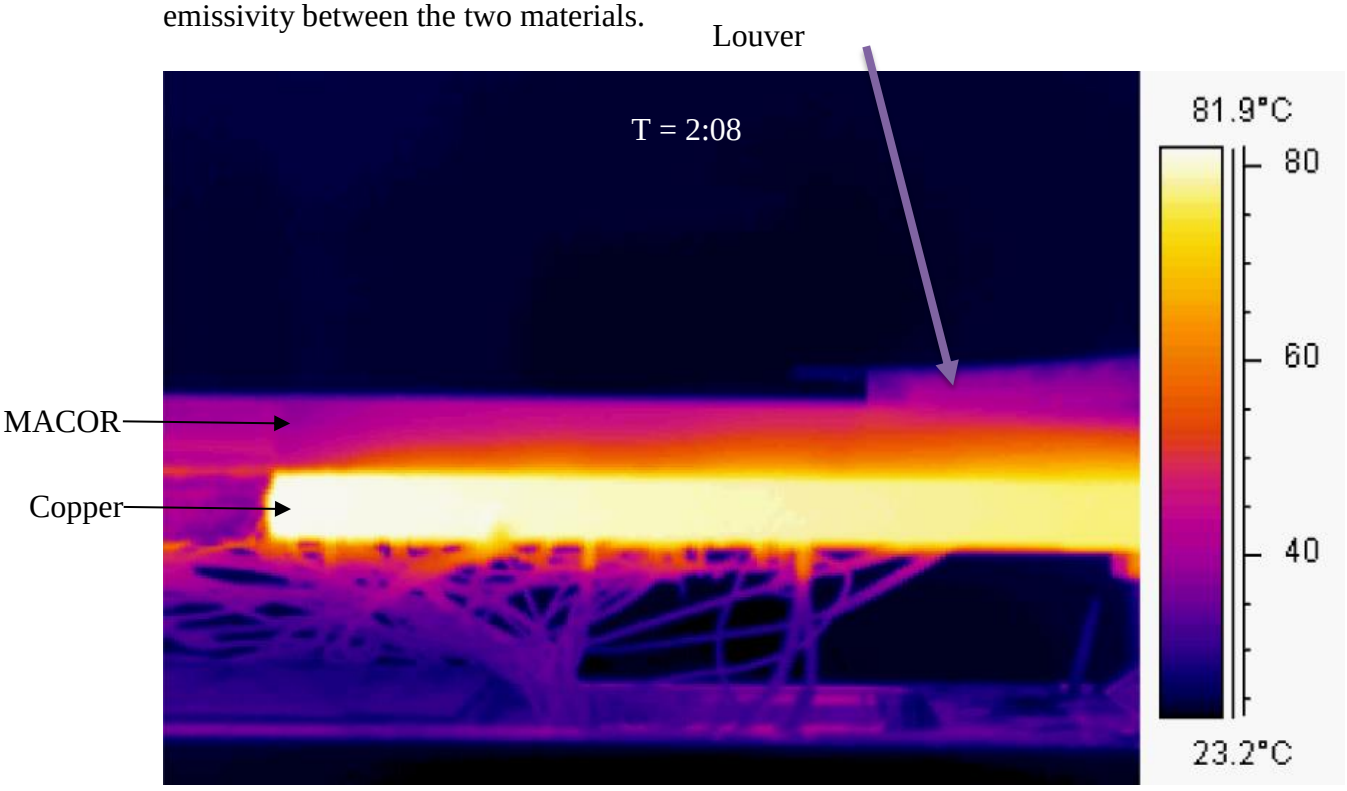

Figure 69: Thermal image of the MACOR and copper plates during heating

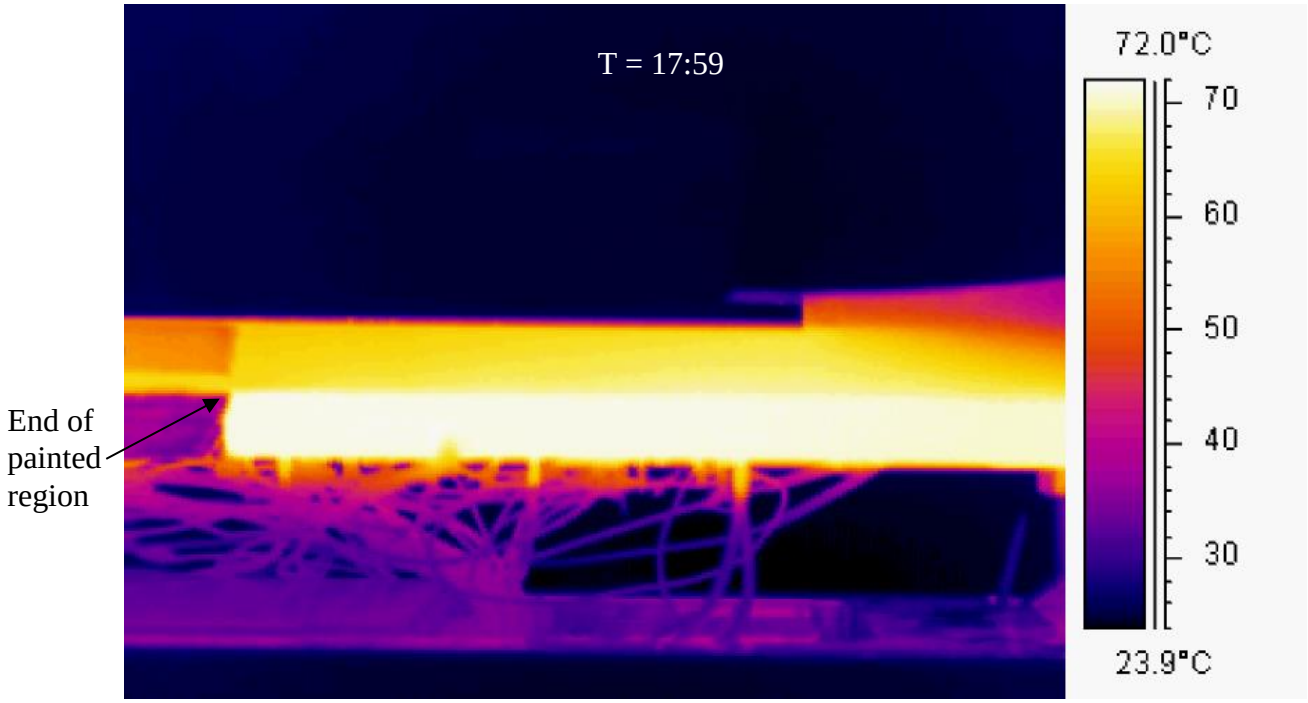

Figure 70: Thermal image of MACOR and copper plates after smoothing

The image in Figure 69 was taken at 2:08 in the video, and the image in Figure 70 was from 17:59. This shows that the plates typically take about 15 minutes to reach 70°C, and a further 10 minutes to fall to 60°C and achieve a uniform temperature profile. However, between tests the plates only cooled to ~55°C, so there was minimal reheating needed between runs – typically less than 5 minutes. Therefore, tests were typically conducted 15-20 minutes apart to allow time for plates to reheat and develop a uniform temperature distribution. There is a small amount of heat present in the louver structure, but the film flow has such a low residence time in the film injection region that the warm louver would not further heat the flow to any measurable degree.

Bibliography

[1] D. Bogard and K. Thole, “Gas Turbine Film Cooling,” *J. Propuls. Power*, vol. 22, no. 2, pp. 249–270, 2006.

[2] W. M. Grisson, “Liquid Film Cooling in Rocket Engines,” 1991.

[3] D. Maqbool, K. Dellimore, and C. Cadou, “Development of a Supersonic Film Cooling Test Facility,” no. July, pp. 1–14, 2010.

[4] T. Hansmann, “An experimental investigation of the film-cooling process at high temperatures and velocities,” *Arch. Set 521*, no. December, 1963.

[5] J. Goldstein, R. B. Rask, and E. R. G. Eckert, “Film Cooling with Helium Injection Air Flow,” *Int. J. Heat Mass Transf.*, vol. 9, pp. 1341–1350, 1966.

[6] E. ECKERT and R. GOLDSTEIN, “Film cooling with air and helium injection through a rearward-facingslot into a supersonic air flow.,” *AIAA J.*, vol. 4, no. 6, pp. 981–985, 1966.

[7] R. J. Goldstein and M. Y. Jabbarlf, “Film Cooling Effectiveness with Helium and Refrigerant 12 Injection into a Supersonic Flow,” *AIAA J. Compos. Mater.*, vol. 8, no. 4, pp. 246–251, 1970.

[8] M. Hunt, K. Juhany, and J. Sivo, “Supersonic film cooling effectiveness using air and helium for a range of injectant temperatures and Mach numbers,” *26th Thermophys. Conf.*, 1991.

[9] B. Aupoix, A. Mignosi, S. Viala, F. Bouvier, and R. Gaillard, “Experimental and numerical study of supersonic film cooling,” *AIAA J.*, vol. 36, no. 6, pp. 915–923, 1998.

[10] M. Konopka, M. Meinke, and W. Schröder, “Large-Eddy Simulation of

Supersonic Film Cooling at Incident Shock-Wave Interaction," in *High Performance Computing in Science and Engineering '12*, 2012.

[11] J. D. Anderson, *Modern Compressible Flow: With Historical Perspective*, 3rd Editio. McGraw –Hill Science/Engineering/Math, 2002.

[12] T. Badinand and T. H. Fransson, "Radiative Heat Transfer in Film-Cooled Introduction," vol. 17, no. 1, pp. 1–6, 2003.

[13] G. P. Sutton and O. Biblarz, *Rocket Propulsion Elements*, 8th Editio. Wiley, 2010.

[14] C. I. Morris and J. H. Ruf, "Validation of Supersonic Film Cooling Modeling for," no. July, 2010.

[15] N. FS–2008–11–158–MSFC, "George C. Marshall Space Flight Center, Huntsville, AL 35812," 2008.

[16] C. A. Cruz, "Experimental and Numerical Characterization of Turbulent Slot Film Cooling," University of Maryland, 2008.

[17] C. A. Cruz, "Large-Eddy Simulation of Film Cooling Through a 2D Slot," no. July, pp. 1–11, 2006.

[18] F. Raffan, "Experimental Characterization of Slot Film Cooling Flows with Minimally Intrusive Diagnostics," 2008.

[19] K. Dellimore, "Modeling and Simulation of Mixing Layer Flows For Rocket Engine Film Cooling," University of Maryland, 2010.

[20] D. Maqbool, "Development of an experiment for Measuring Film Cooling Performance in Supersonic Flows," University of Maryland, 2011.

[21] J. V. Beck, "Surface heat flux determination using an integral method," *Nucl.*

Eng. Des., vol. 7, pp. 170–178, 1968.

[22] C. J. Chen and J. S. Chiou, "Prediction of Surface Temperature and Heat Flux from an Interior Temperature Response," *Lett. Heat Mass Transf.*, vol. 3, pp. 539–548, 1976.

[23] A. P. Voegele, "Experimental and Numerical Investigation of Tangentially-Injected Slot Film Cooling," 2013.

[24] H. Jasak, A. Jemcov, and Z. Tukovic, "OpenFOAM : A C ++ Library for Complex Physics Simulations," *Int. Work. Coupled Methods Numer. Dyn.*, vol. m, pp. 1–20, 2007.

[25] X. T. Yan, "On the Penetration Depth in Fourier Heat Conduction," in *8th AIAA/ASME Joint Thermophysics and Heat Transfer Conference*, 2002, no. June.

[26] R. S. Figliola and D. E. Beasley, *Theory and Design for Mechanical Measurements*, 3rd ed. Wiley, 2005.

[27] G. C. Fralick, J. D. Wrbanek, and C. Blaha, "Thin Film Heat Flux Sensor of Improved Design." 2002.

[28] A. Esposito, F. De Rosa, V. Caso, and F. Parente, "Design of slug calorimeters for re-entry tests," *NASA Tech. Pap*, 2010.

[29] M. Imber and J. Khan, "Prediction of transient temperature distributions with embedded thermocouples," *Aiaa J.*, vol. 10, no. 6, pp. 784–789, 1972.

[30] C. J. Marek and R. R. Tacina, "Effect of Free-Stream Turbulence on Film Cooling." National Aeronautics and Space Administration, Washington, D.C., 1975.

[31] G. S. Settles, *Schlieren and Shadowgraph Techniques*. 2001.

[32] M. J. Colaço, H. R. B. Orlande, and G. S. Dulikravich, "Inverse and optimization problems in heat transfer," *J. Brazilian Soc. Mech. Sci. Eng.*, vol. 28, no. 1, pp. 1–24, 2006.

[33] J. V Beck and B. Blackwell, "Comparison of some inverse heat conduction methods using experimental data," *Int. J. Heat Mass Transf.*, vol. 39, no. 17, pp. 3649–3657, 1996.

[34] M. N. Ozisik and H. R. B. Orlande, *Inverse heat transfer*. 2000.

[35] C. J. Chen and D. M. Thomsen, ""On Determination of Transient Surface Temperature and Heat Flux by Imbedded Thermocouple in a Hollow Cylinder," *AIAA J.*, vol. 13, no. 5, pp. 697–699, 1975.

[36] I. Celik and O. Karatekin, "Numerical Experiments on Application of Richardson Extrapolation With Nonuniform Grids," *J. Fluids Eng.*, vol. 119, no. 3, p. 584, 1997.

[37] B. Larson, "Study of the Factors Affecting the Sensitivity of Liquid Penetrant Inspections : Review of Literature Published from 1970 to 1998," no. January, p. 22161, 2002.

[38] M. Collett, "Experimental Investigation of Film Cooling in a Supersonic Environment," University of Maryland, 2015.

[39] H. E. Smith, "THE FLOW FIELD AND HEAT TRANSFER DOWNSTREAM OF A REARWARD FACING STEP IN SUPERSONIC FLOW," no. March, 1967.

[40] J. Dittmar, A. Schulz, and S. Wittig, "Assessment of various film-cooling

configurations including shaped and compound angle holes based on large-scale experiments," *J. Turbomach.*, vol. 125, no. 1, pp. 57–64, 2003.

[41] A. J. H. Teekaram, C. J. P. Forth, and T. V. Jones, "Film Cooling in the Presence of Mainstream Pressure Gradients," *J. Turbomach.*, vol. 113, no. 3, p. 484, 1991.

[42] Y. W. Kim, C. Coon, and H.-K. Moon, "Film-Cooling Characteristics of Pressure-Side Discharge Slots in an Accelerating Mainstream Flow," *ASME Conf. Proc.*, vol. 2005, no. 47268, pp. 889–897, 2005.

[43] J. Stoll, "Film Cooling and Heat Transfer in Nozzles," *J. Turbomach.*, vol. 110, no. 1, pp. 57–65, 1988.

[44] D. W. Kearney, R. J. Moffat, and W. M. Kays, "The Turbulent Boundary Layer : Experimental Heat Transfer With Strong Favorable Pressure Gradients and Blowing," Stanford, California, 1970.